

T.C.

UNIVERSITY OF TURKISH AERONAUTICAL ASSOCIATION

SCIENCE AND TECHNOLOGY INSTITUTE

**WIND ASSESSMNT FOR DEFFERNTS SITES IN LIBYA AND
PROPER WIND TURBINE BLADE DESIGN USING CFD**

Ph.D. THESIS

SALEM RAMADAN SILINI

1303947011

Thesis Supervisor: Asst. Prof. Dr. Munir Ali Elfarra

DEPARTMENT OF MECHANICAL AND AERONAUTICAL

ENGINEERING

December 2018



Thesis Defense Date: 28 Dec. 2018

**OF UNIVERSITY OF TURKISH AERONAUTICAL ASSOCIATION
INSTITUTE OF SCIENCE AND TECHNOLOGY
STATEMENT NON-PLAGIARISM**

I hereby declare that all information in this study I present as my Ph.D. thesis, entitled “*Wind Assessment for Different Sites in Libya And Proper Wind Turbine Blade Design Using CFD*”, has been presented in accordance with the academic rules and ethical conduct. I also declare and certify with my honor that I have fully cited and referenced all sources utilized in this study.

28 Dec. 2018.

Salem Ramadan Omer Silini

WIND ASSESSMENT FOR DEFERRED SITES IN LIBYA AND PROPER WIND TURBINE BLADE DESIGN USING CFD

SILINI, Salem

Ph.D., Department of Mechanical and Aeronautical Engineering

Thesis Supervisor: Asst. Prof. Dr. Munir Ali Elfarrar

Decembere-2018, 116 pages

ABSTRACT

The current study is a multidisciplinary research which incorporates analyses based on computational fluid dynamics (CFD) of a wind turbine blade and wind energy assessment of real wind data. The technical and economical assessment was performed for four sites close to the Libyan; Tarhuna, Alazeziya, Tolmeita and Almqrn. The assessment was carried out using the Weibull distribution function and the Weibull parameters were calculated using three different methods; graphical method (GM), empirical method (EM) and maximum likelihood method (MLM). Error analyses using various techniques were conducted to check for the validity of the different Weibull methods used. The technical assessment includes the calculations of the annual energy production (AEP), capacity factor (C_f) and greenhouse gas emission (GHG) reduction. The estimated annual energy production was used in the calculation of the present value of cost which estimates the cost of each kWh of electricity produced by a certain wind turbine.

The effect of the annual greenhouse gas emission reduction on the cost analysis was also considered. The results have shown the electricity cost of all the sites is below the world average electricity price. Using different Weibull parameters have noticeable effects on the technical and economical estimations of wind power production. The MLM method yields higher AEP estimation compared to the other methods for all the sites. On the other hand, GM method gives less estimation for the AEP compared to the other methods for all the sites. Adding the GHG reduction income into the electricity cost calculations decreases it by an average of 18%. The CFD work was carried out to find the best blade tip pitch angle distribution and proper blade of a wind turbine rotor size to increase its power output and hence increase the AEP of the analyzed sites. The baseline case is the NREL VI experimental wind

turbine which is a stall regulated turbine. Using the CFD method, the optimum blade tip pitch angle to maximize the power output (provided that the rated power is not exceeded) was obtained for each wind speed in the range between 5-20 m/s and the new optimum pitch power curve was computed. Doing so, the stall regulated turbine was converted into a pitch regulated one. The blade with the optimum pitch was enlarged by three different scale factors, 1.05, 1.1 and 1.15, and the power curve corresponding to each scale factor was calculated by solving the Reynolds Average Navier Stokes equations. Wind assessment was conducted to estimate the annual energy production and to calculate the generated electricity cost using the real wind data of the sites and the computed power curves of the new designed blades. The wind assessment was performed using the maximum likelihood method which is a two-parameter Weibull distribution method. The results have shown a significant increase in annual energy production and pronounced decreases in generated electricity cost after using the new pitch distribution with different blade size scales.

Keywords: CFD, blade tip pitch angle, wind energy, blade sizing, Weibull distribution, wind assessment, annual energy production, present value of cost.

LIBYA'DA FARKLI SİTELER İÇİN RÜZGAR DEĞERLENDİRMESİ VE CFD KULLANARAK PROPER RÜZGAR TÜRBİNİ BLADE TASARIMI

SILINI, Salem

Doktora, Makine ve Havacılık Mühendisliği Bölümü

Tez Danışmanı: yrd. Prof. Dr. Munir Ali Elfarra

Aralık-2018, 116 sayfa

ÖZET

Bu çalışma multidisipliner bir araştırmadır. bir rüzgar türbini kanadının hesaplamalı akışkan dinamiğine (CFD) ve gerçek rüzgar verilerinin rüzgar enerjisi değerlendirmesine dayanan analizleri içerir. Teknik ve ekonomik değerlendirme, Libya'ya yakın dört bölge için yapıldı; Tarhuna, Alazeeziya, Tolmeita ve Almqun. Değerlendirme Weibull dağılım fonksiyonu kullanılarak yapıldı ve Weibull parametreleri üç farklı yöntem kullanılarak hesaplandı; grafiksel yöntem (GM), ampirik yöntem (EM) ve maksimum olasılık yöntemi (MLM). Kullanılan farklı Weibull yöntemlerinin geçerliliğini kontrol etmek için çeşitli teknikler kullanılarak hata analizleri yapılmıştır. Teknik değerlendirme, yıllık enerji üretimi (AEP), kapasite faktörü (Cf) ve sera gazı emisyonu (GHG) azaltma hesaplarını içermektedir. Tahmini yıllık enerji üretimi, belirli bir rüzgar türbini tarafından üretilen her bir kWh elektriğin maliyetini tahmin eden mevcut maliyet değerinin hesaplanmasında kullanılmıştır.

Yıllık sera gazı emisyonu azaltımının maliyet analizine etkisi de dikkate alınmıştır. Sonuçlar tüm sahaların elektrik maliyetinin dünya elektrik fiyatının altında olduğunu göstermiştir. Farklı Weibull parametrelerinin kullanılması, rüzgar enerjisi üretiminin teknik ve ekonomik tahminlerini belirgin şekilde etkiler. MLM yöntemi, tüm siteler için diğer yöntemlere kıyasla daha yüksek AEP tahmini sağlar. Öte yandan, GM metodu AEP için tüm sahalar için diğer metotlara göre daha az tahmin vermektedir. Sera gazı azaltma gelirini elektrik maliyet hesaplamalarına eklemek ortalama% 18 oranında azalmaktadır. CFD çalışması, en iyi bıçak ucu adım açısı dağılımını ve güç çıkışını arttırmak ve böylece analiz edilen alanların AEP'sini arttırmak için bir rüzgar türbini rotor boyutunun uygun bıçağını bulmak için gerçekleştirildi. Temel durum, durak ayarlı bir türbin olan NREL VI deneysel rüzgar türbinidir. CFD yöntemini kullanarak, güç çıkışını maksimize etmek için (nominal gücün aşılması şartıyla) optimum bıçak ucu adım açısı, 5-20 m / s aralığında her rüzgar hızı için elde edildi ve yeni optimum adım gücü eğrisi, bilgisayarlı. Bunu yaparak, durak ayarlı türbin, ayarlanmış bir aralığa dönüştürüldü. Optimum eğime sahip bıçak, üç farklı ölçek faktörü, 1.05, 1.1 ve 1.15 ile büyütüldü ve her bir ölçek faktörüne karşılık gelen güç eğrisi, Reynolds Ortalama Navier Stokes denklemleri çözülerek hesaplandı. Yıllık enerji üretimini tahmin etmek ve sahaların gerçek rüzgar verilerini ve yeni tasarlanmış bıçakların hesaplanan güç eğrilerini kullanarak üretilen elektrik maliyetini hesaplamak için rüzgar değerlendirmesi yapıldı. Rüzgar değerlendirmesi, iki parametrelili bir Weibull dağılım yöntemi olan maksimum olasılık yöntemi kullanılarak yapıldı. Sonuçlar, yeni ptich dağılımını farklı bıçak ebatı ölçeklerle

kullandıktan sonra, yıllık enerji üretiminde önemli bir artış ve üretilen elektrik maliyetinde belirgin bir düşüş olduğunu göstermiştir.

Anahtar Kelimeler: CFD, bıçak uç açısı açısı, rüzgar enerjisi, bıçak boyutlandırma, Weibull dağılımı, rüzgar değerlendirme, yıllık



ACKNOWLEDGMENTS

First of all, I would like to thank Allah Almighty for his divine help. I sincerely thank my supervisor Mr. Munir Elfarrar for his support, guidance and keenness to overcome the difficulties, which helped me accomplish this thesis.

Also, I extend sincere thanks to the honorable committee members for their time and valuable feedback. I dedicate this work to my father (may Allah have mercy on him), to my mother (may Allah prolong her life), my wife (Asma), who has been patient during the accomplishment of PhD, and to my sons Ahmed, Jini, Jinan and Rafaa.

I also thank the rest of my family members including my brothers and sisters and uncle Abdullah Al-Sghayer and aunt Ambaraka. I feel so thankful to all the friends and especially my dear friends Nagi Nusir, Ali Belhag, Abdulbaset Mohammed and Faraj Altheep and my dear Turkish family (Mr. Sihhat Karabıyık, Ms.Emine Gülay Karabıyık and their daughters).

I am thankful to the Turkish government, cooperative, Turkish people, the university staff, and everyone else, who helped me when I needed it.

CONTENTS

ABSTRACT	IV
ÖZET	VI
ACKNOWLEDGMENT	VIII
TABLE OF CONTENTS	IX
LIST OF TABLES	XII
LIST OF FIGURES	XIII
LIST OF NOMENECLATURE	XV
GREEK LETTERS	XVII
ABBREVIATIONS	XVIII
CHAPTER 1	1
INTRODUCTION	1
1.1. Wind	2
1.2. Wind Energy	2
1.3. The first attempts to produce electricity power from the wind	3
1.3.1. Wind Turbine Pioneers in Denmark.....	3
1.3.2. Ambitious wind power plant installation in Germany	5
1.3.3 1250 kw Power Generation through wind-The First Huge American wind ..	5
1.4. Modern wind turbines.....	7
1.4.1. Horizontal Axis Wind Turbines	7
1.4.2 Vertical Axis Wind Turbines.....	8
1.5. Principles generation of energy wind turbine.....	9
1.6. Methods to control and regulate power in wind turbines (Aerodynamic Torque Control).....	12
1.6.1. Stall-regulated rotor designs.....	12
1.6.2. Pitch regulated rotor designs	12
1.7. A brief review of the aerodynamic models	13

1.7.1 Blade Element Momentum Method	13
1.7.2 Navier-Stokes Solvers.	14
1.8. Energy Situation of Libya	15
1.9. Wind in Libya	17
1.10. Literature Review	18
CHAPTER 2	21
TECHNICAL AND ECONOMICAL EVALUATION ANALYSIS OF WIND POWER GENERATION IN FOUR SITES USING DIFFERENT WEIBULL ...	21
2.1. Wind Data.....	21
2.2. Analysis Method	26
2.2.1. Graphical Method (GM)	27
2.2.2. Empirical Method (EM)	28
2.2.3. Maximum Likelihood Method (MLM)	28
2.3. Error Analysis	28
2.4. Weibull Parameters	9
2.5. Probability Density and Cumulative Distribution Functions	3
2.6. Annual Energy Production and Capacity Factor	40
2.7. Present value Cost and Electricity Price	43
2.8. Greenhouse Gases Emission Reduction	45
CHAPTER 3	47
COMPUTATIONAL FLUID DYNAMIC AND NUMERICAL SOLUTION	7
3.1. Navier-Stokes Equations	48
3.2 Turbulence Models	52
3.2.1. Closure Problem and the Statistical Turbulence Models	52
3.3. Reynolds Averaged Navier-Stokes (RANS) Equations Spalart-Allmaras Model ...	53
3.4. Spalart-Allmaras Model	57
3.5. Shear Stress Transport/ $k - \omega$ (SST)	58
3.6. Pre-conditioning for Low Mach Number Flows	60

3.6.1. Hakimi Preconditioning.....	60
3.7. Boundary Conditions.....	61
3.7.1. Solid Wall Boundary Conditions.....	61
3.7.2. External Boundary Conditions	62
CHAPTER 4.....	64
CFD Simulations for Test Cases: NREL Phase VI (HAWT Rotors)	64
4.1. Experimental Data and Basline Blade Description of the Test Case	64
4.2. Geometric Blade	66
4.2.1. Airfoil Features.....	66
4.2.2 S809 Wind Turbine Airfoil	67
4.3. Mesh Generation	70
4.4. CFD Simulation and Results	73
4.4.1. Flow Simulation	74
CHAPTER 5.....	82
RESULTS AND DISCUSSIONS	82
5.1. Annual energy and power curve of the baseline turbine	82
5.2. Optimum Blade Tip Pitch Angles	83
5.3. Wind Turbine Blade Sizing	89
5.4. Electricity and Present Value Cost, PVC	92
CHAPTER 6.....	97
CONCLUSION	97
6.1. Conclusion and Recommendations	97
6.2. Future Work.....	98
REFERENCES	99

LIST OF TABLES

Table 1.1	Total Energy Production and Consumption (2010 - 2012)	16
Table 2.1	Physical features of the meteorological stations.....	21
Table 2.2	Average wind speeds at 20 m height	22
Table 2.3	Average wind speeds at 40 m height	22
Table 2.4	Average wind speeds at 60 m height	23
Table 2.5	Weibull Parameters estimated by three methods at 20m height.....	31
Table 2.6	Weibull Parameters estimated by three methods at 40m height.....	32
Table 2.7	Weibull Parameters estimated by three methods at 60m height.....	32
Table 2.8	Error analysis results.....	33
Table 2.9	Technical specifications of the model wind turbine	41
Table 2.10	Annual energy production and capacity factor for all sites at 60m	42
Table 2.11	The values of the terms in the present value cost equation	43
Table 2.12	Electricity Cost of each kWh for each site	44
Table 2.13	Annual GHG reduction for each site	46
Table 2.14	Cost of kWh for each site considering the GHG reduction effect.....	46
Table 3.1	Sutherland's law Coefficient	63
Table 4.1	NREL Phase VI blade description.....	66
Table 4.2	Twist and chord variations (NREL-VI rotor blade)	68
Table 4.3	Different grid system for <i>NREL-VI</i> at 5m/s	71
Table 4.4	Different Turbulence Models and their Power Generation (NREL-VI).....	75
Table 5.1	The results for AEP and C_f (NREL VI)	83
Table 5.2	Baseline Power Optimum Power at different wind speeds	87
Table 5.3	Optimum pitch angles at different wind speeds	88
Table 5.4	RPM versus scale factor	90
Table 5.5	Comparison of power output percentage increase for the different scale.....	91
Table 5.6	Mean wind speeds at 20 m height.....	92
Table 5.7	Comparison of the Annual energy production.....	93
Table 5.8	The values of the terms in the PVC equation and the calculated PVC.....	94
Table 5.9	Electricity cost of each kWh for each site at different blade configur ...	94
Table 5.10	Electricity cost of each kWh for each site at different blade with reduction....	95
Table 5.11	Percentage of reduction in electricity cost.....	95

LIST OF FIGURES

Fig. 1.1 Global Wind Power Capacity and Yearly Increase - 2006-2016	1
Fig. 1.2 Diurnal valley and mountain wind (Rohatgi and Nelson, 1994) [3].....	1
Fig. 1.3 Paul La Cours built the first experimental wind turbines in 1891	3
Fig. 1.4 Turbine of La-Cour-Lykkegard (18m, 30kW and rated speed 12m/s)	4
Fig. 1.5 Smidth Turbine. (Three blades - diameter 24m - rated capacity 70Kw)	4
Fig. 1.6 Project Kleinhenz Whit (130m rotor diameter and 10,000kW rated power) ..	5
Fig. 1.7 Jacob's "wind charger" (4m rotor diameter, rated power 1.8 3kW).....	6
Fig. 1.8 Smith Wind turbine, US: 53.2m rotor diameter 1251kW rated power[9]	7
Fig. 1.9 Horizontal wind turbine components [10]	8
Fig. 1.10 Vertical wind turbine components [12]	9
Fig. 1.11 Actuator disk model of a wind turbine [15].....	10
Fig.1.12 Axial thrust and power curve comparison between pitch and stall regulat	13
Fig. 1.13 The energy consumption over the last 10 years [27]	16
Fig. 1.14 The wind speed in coastal cities in Libya, [28]	17
Fig. 1.14 The Libyan renewable energy plan (<i>Source: REAOL</i>)	17
Fig. 2.1 The location of the sites in Libya.....	21
Fig. 2.2 Monthly variation of wind speeds for the selected sites at 20m height.....	23
Fig. 2.3 Monthly variation of wind speeds for the selected sites at 40m height.....	23
Fig. 2.4 Monthly variation of wind speeds for the selected sites at 60m height.....	24
Fig. 2.5 Annual mean wind speeds for the selected sites at 20m height.....	24
Fig. 2.6 Annual mean wind speeds for the selected sites at 40m height.....	25
Fig. 2.7 Annual mean wind speeds for the selected sites at 60m height.....	25
Fig. 2.8 Measured annual frequency distribution at height 20m.....	25
Fig. 2.9 Measured annual frequency distribution at height 40 m.....	26
Fig. 2.10 Measured annual frequency distribution at height 60 m.....	26
Fig. 2.11 Graphical method to estimate the Weibull parameters at 20m	30
Fig. 2.12 Graphical method to estimate the Weibull parameters at 40m	30
Fig. 2.13 Graphical method to estimate the Weibull parameters at 60m.....	31
Fig. 2.14 Probability density function for the sites at 20m height	34
Fig. 2.15 Probability density function for the sites at 40m height	35
Fig. 2.16 Probability density function for the sites at 60m height	36

Fig. 2.17 Cumulative distribution function for the sites at 20m height	37
Fig. 2.18 Cumulative distribution function for the sites at 40m height	38
Fig. 2.19 Cumulative distribution function for the sites at 60m height	39
Fig. 2.20 Power curve of the model wind turbine	41
Fig. 2.21 Comparison of <i>AEP</i> among the sites using different Weibull methods for 60m .43	
Fig. 3.1 Process of Computational Fluid Dynamics.....	47
Fig. 4.1 NREL-VI Wind Turbine Inside the NASA Ames Wind Tunnel. [77]	64
Fig. 4.2 Baseline Plan Form View	65
Fig. 4.3 Baseline twist distribution along the blade	65
Fig. 4.4 Geometric Blade	66
Fig. 4.5 S809 Airfoil	67
Fig. 4.6 Angle and twist at different blade sections (NREL-VI)	69
Fig. 4.7 3D <i>NREL-VI</i> blade geometry (created using AutoBlade software).....	69
Fig. 4.8 3D blade	70
Fig. 4.9 Y+ contours for 5 m/s and 9 m/s	72
Fig. 4.10 3-D mesh strcutue of the basline blade	73
Fig. 4.11 Power Generation Comparison: Experimental vs. Computed Generation 74	
Fig. 4.12 Pressure contours	75
Fig. 4.13 Experimental vs. Calculated Pressure Coefficients at 5m/s.....	77
Fig. 4.14 Experimental vs. Calculated Pressure Coefficients at 10m/s	78
Fig. 4.15 Experimental vs. Calculated Pressure Coefficients at 13m/s.....	80
Fig. 5.1 Power curve of baseline turbine and annual energy of sites.....	83
Fig. 5.2 Optimum pitch angle at different wind speeds	84
Fig. 5.3 Optimum pitch angle at different wind speeds	85
Fig. 5.4 Optimum pitch angle at different wind speeds	86
Fig. 5.5 Comparison between the optimum power and the baseline power.....	88
Fig. 5.6 Blade geometries with different scale factors	89
Fig. 5.7 Comparison of power curves for different scales	90

LIST OF NOMENECLATURE

T	Thrust
\dot{m}	Mass flow rate
U_1	Free stream velocity
U_4	Velocity for wake region
A	cross sectional area
p_1, p_2	Pressure before and behind rotor
a	Induction factor
P	Power from wind
V_m	Mean wind speed
$PF(v)$	Weibull distribution function
$F(v)$	Cumulative Distribution Function
k	Shape factor
c	Scale factor
R^2	coefficient of determination
C_f	Capacity factor
t	turbine life time
i	Inflation rate
ri	Interest rate
c	Chord length
C_D	Drag coefficient
C_L	Lift coefficient
C_N	Normal force
C_P	Pressure coefficient
C_T	Tangential force coefficient
e	Internal energy
e_0	Total energy
F	Inviscid flux
f_{ei}	External force component
F_v	Viscous flux

h	Enthalpy
h_0	Total enthalpy
K	Coefficient of thermal conduction, Kinetic turbulent energy
Q	Vector of conservation Variables
q_j	Heat flux
R	Radius of wind turbine rotor
r	Local blade radius
Re	Reynolds number
S_T	Source temp.
S_{ij}	Strain rate tensor
u_i	Cartesian velocity component
V	Space volume
V_z	Axial Velocity
V_r	Relative velocity component

GREEK LETTERS

σ	standard deviation
α	Angle of attack
β	Twist angle
δ_{ij}	Kronecker delta
θ	Local pitch angle
ε	Turbulent dissipation
θ_T	Blade twist angle
θ_p	Pitch angle
λ	Second coefficient of viscosity, Tip speed ration
μ	Dynamic viscosity
ν	Kinematic viscosity
ν_T	Turbulent viscosity
ρ	Density
τ_{ij}	Viscous stress tensor
ϕ	Flow angle
ω	Specific turbulent dissipation rate
Ω	Angular speed
C_p	Pressure coefficient

ABBREVIATIONS

GM	Graphical Method
EM	Empirical method
MLM	Maximum likelihood method
RMSE	Root Mean Square Error
MBE	Mean Bias Error
MAE	Mean Bias Absolute Error
AEP	Annual energy production
PVC	Present value of costs
GHG	Greenhouse Gases Emission Reduction
PDEs	Partial differential equations
BEM	Blade Element Momentum
CFD	Computational Fluid Dynamics
GECOL	General Electricity Company of Libya
HAWT	Axis Wind Turbines
VAWT	Perpendicular Axis Wind Turbines
LE	Leading Edge
NREL	National Renewable Energy Laboratory
RANS	Reynolds Average Navier Stokes
REAOL	Renewable Energy Authority of Libya
RPM	Revelation per Minute
SST	Shear Stress Transport
AS	Spalart – Allmaras
TE	Trailing Edge

Chapter 1

Introduction

The global energy requirements have exponentially increased because of excessive human population and rapid industrialization. The energy requirements were met using fossil fuels and their derivatives but now they are depleting at a great speed. Rising demands will ultimately lead to unmet energy requirements; thus, the existing energy supply is unsustainable. It requires paradigm shift from fossil fuel dependence to finding new ways to meet the energy challenges. Now the focus is towards renewable energy sources, which might be way more sustainable as compared to fossil fuels. They are needed in large quantities. Traditional and nuclear power generation will be used only until sufficiently developing sustainable renewable energy.

Moreover, awareness of this issue has caused development of sustainable and renewable energy technologies. The clean power generation sources are sought for limiting adverse power generation effects on the atmosphere. Experts have identified some renewable energy forms such as hydro, solar, current, and wind, which are significantly affected by weather. For example, the wind power generation results in heating the earth's surface. This happens because the wind generates waves in the atmosphere. Moreover, the solar energy isn't the ultimate renewable form of energy because the techniques used for harnessing it still require further development. Currently, the overall power generation using wind energy is increasing at a higher rate, which is likely to increase further, as Figure 1 shows.

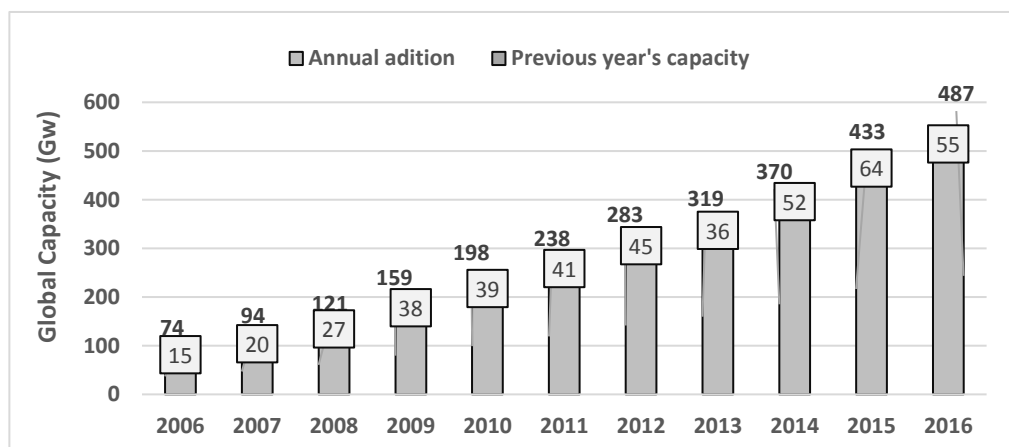


Figure 1.1. Global Wind Power Capacity and Yearly Increase - 2006-2016
(RENEWABLES 2017)

1.1. Wind

Wind is a result of what is happening to the atmospheric pressure due to the effect of solar radiation. When hot air layers rise, and replace cold air layers, the currents of air turn into wind. Wind is the main factor in the atmospheric circulation of the layers. There are many types and patterns due to differences in temperature between the land, seas, oceans, and mountains as Figure 1.2 shows.

The earth's surface roughness affects the wind speed and objects such as mountains, trees and buildings. Winds are classified according to their speed, source and geographical location. [1, 2]

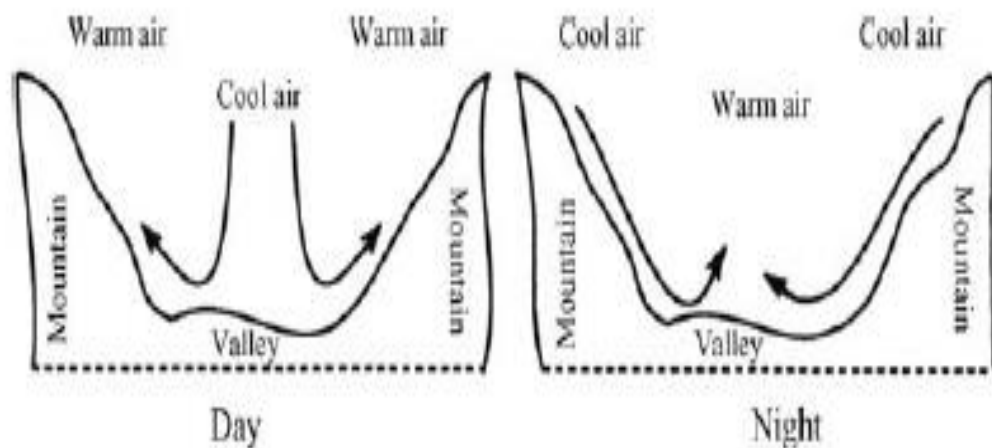


Figure 1.2. Diurnal valley and mountain wind (Rohatgi and Nelson, 1994) [3]

1.1. Wind Energy

Wind power is used to pass air through wind turbines to produce electrical energy through generators. This type of energy is widely available, and it causes no greenhouse gas emissions during operation. In addition, it has limited impact on the environment as compared to non-renewable energy sources.

1.3. The first Attempts to Produce Electricity Power from the Wind

The first wind power plants were established with a capacity of about 500 kilowatts in New York in 1882 and in Berlin [4]. In 1891, three-phase current was adopted for this purpose.

The technology of power plants has rapidly developed since the 19th Century, especially in the industrialized countries. The first attempts to produce energy from wind were done in that period despite the presence of electricity in cities; however, the first technical development of the use of wind occurred in Denmark.

1.3.1. Wind Turbine Pioneers in Denmark

Paul La Cours built the first experimental wind turbines to operate like a "dynamo" in 1891 (Fig.1. 2). The obvious result is that he was able to deal with the problem of storage of excess energy produced from the turbine and storage of emitted hydrogen gas between 1885 and 1902.

La Cour Lykkegard was created having different turbine sizes from 10 to 35Kw. The rotor consists of four sails, which make it probable to stay below a certain rotational speed limit to supply a small network in the form of an isolated battery (Fig. 1.3).



Figure.1.3. Paul La Cours Built the first Experimental Wind Turbines in 1891 in Askov, Denmark [4]



Figure.1.4. Turbine of La-Cour-Lykkegard (18m, 30kW and rated speed 12m/s) in Denmark [5]

Due to some of the problems related to the dynamic properties of rotor blades, the companies turned to producing three rotor blades of diameter 24m with almost 70kW capacity at 10m/s wind speed (Fig 1.5)



Figure.1.5. Smidth Turbine. (Three blades -Diameter 24m -Rated Capacity 70 kW), 1942 [6]

1.3.2. Ambitious Wind Power Plant Installation in Germany

In Germany, when the scientific research was conducted, a physicist Albert Betz scientifically approached wind physics.

An article was published in 1920 in German Journal of Turbine Science (*Zeitschrift für das gesamte Turbinenwesen*), which clearly indicated that the maximum energy obtained through wind power could not exceed 53% of the energy obtainable from the atmosphere [7].

From 1930 to 1940, Germany focused on many researches and designs of wind energy technology. In 1937, Franz designed a large wind turbine project [8]. Even today, MAN- Kleinhenz technical project provides a good impression of advanced technology (Fig.1.6).



Figure.1.6. Project Kleinhenz Whit (130m Rotor Diameter and 10,000kW Rated Power), 1942

1.3.3. 1250 kW Power Generation Through Wind - the First Huge American Wind Turbine

In 1922, Marcellus and Joseph Jacobs developed a small turbine with two to three blades of 4m diameter each to generate DC power at low speed (Figure.1.7).

From 1920 to 1960, many wind turbines were manufactured with different capacities (1.8-3kW).



Figure 1.7. Jacob's "Wind Charger" (4m rotor Diameter, Rated Power 1.8 3kW), 1932

In 1941, a large turbine was installed and operated in the state of Vermont as shown in Figure.1.8. At that time, it was considered as world's first and the largest wind turbine that had 53.5m rotor diameter, 1250W rated power, and 35.6m tower height.

In 1947, Putnam compiled his research and investigations in the book "Wind Power," in which, he suggested methods to economically handle the optimal wind turbine size [9].

These turbines had rotor diameters 53.3-68.5m, height 45.7-53.3m and power generation capacity 1500-2500kW.



Fig. 1.8. Smith Wind Turbine, US: 53.2m Rotor Diameter 1251kW
Rated Power (1941) [9]

Wind turbines were then developed, and their dynamic properties and productivity were improved.

1.4. Modern Wind Turbines

Turbines were developed during the recent times, and they were very rapidly improved with respect to their many properties. Wind turbines are classified according to their aerodynamic performance or in terms of their structure designs, which are used even nowadays.

Using the effect of aerodynamics forces on a movable body, power is generated from the wind as it passes through the rotor. As a result of the dynamic lift from the movement of the air, the blades move and move the rotor as well. One of the factors required to increase the efficiency of the turbines is thrust reduction and the torque increase.

The modern air turbine has been classified on the basis of the turbine's axis of rotation, which has two types including the horizontal axis wind turbines (HAWT) and the vertical axis turbines (VAWT).

1.4.1. Horizontal Axis Wind Turbines

They are also called as the upwind horizontal axis wind turbines because initially the wind reaches their rotor rather than the tower, so their efficiency is higher as compared to the other types because they do not face any aerodynamic interference because of the tower; however, their problem is their inability to self-align in the direction of the wind; therefore, they require either a yaw system or a tail vane. These turbines are highly affected when the tower interacts with the strong wind; however, using self-aligning systems or flexible rotors help them bear the negative effects of strong winds. Their important components include a gearbox, rotor, generator, anemometer, yaw motor, foundation and the control system (Figure. 1.9)

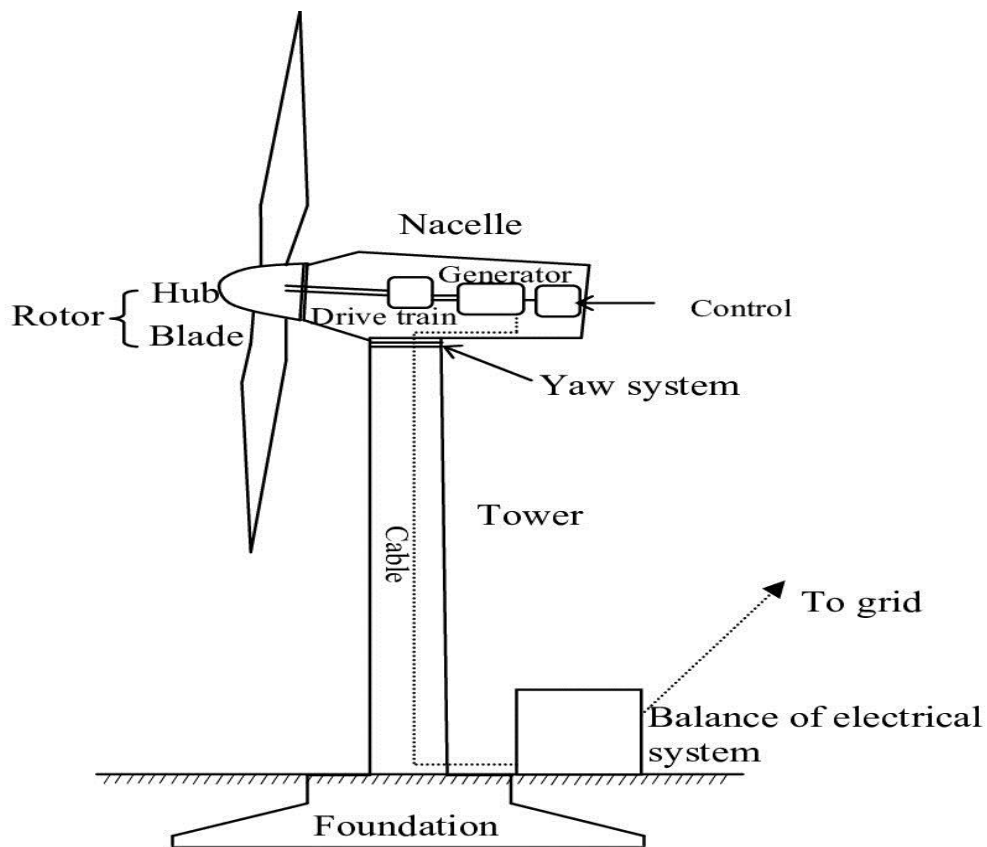


Figure 1.9. Horizontal Wind Turbine Components [10]

1.4.2. Vertical Axis Wind Turbines.

VAWTs are different because their main rotor shaft is vertically arranged. Their main advantage is that the turbine does not necessarily point in the direction of wind.

They are suitable in locations where the direction of wind keeps on changing. They have the capability to utilize wind currents coming from different directions [11].

They have a vertical axis, a gearbox and a generator, which are positioned closer to the ground, so they don't need the tower as a support; therefore, they are easier to maintain. Some designs have a drawback that they generate pulsating torque. They may also create drag when their blades rotate in the wind. They are shown in Figure 1.10.

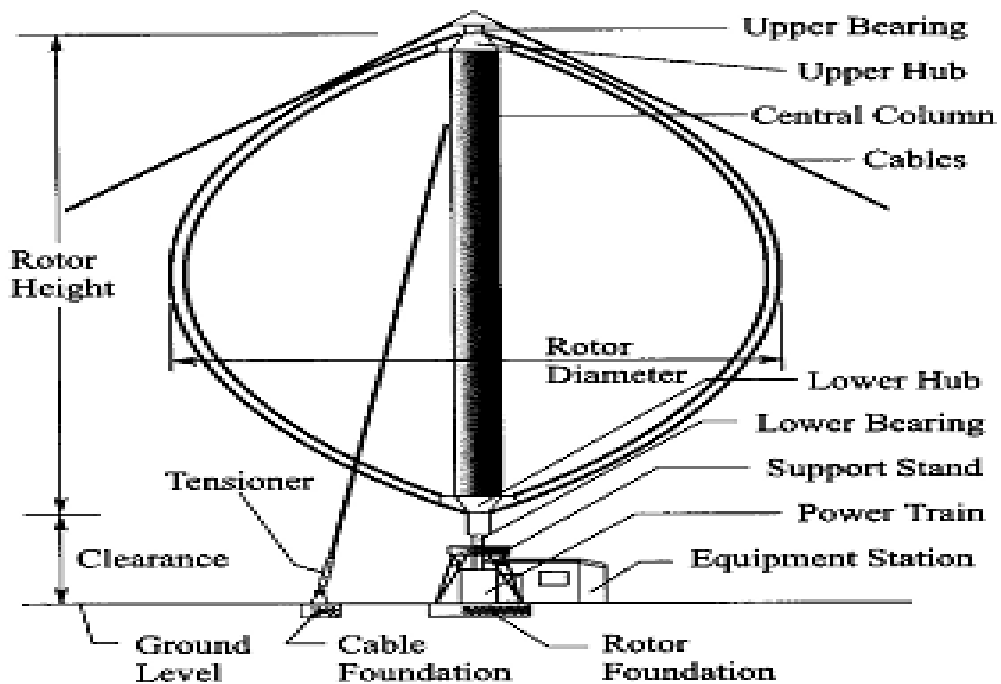


Figure 1.10. Vertical Wind Turbine Components [12]

1.5. Principles of Power Generation through Wind Turbines

The basic single-dimensional wind turbine model is also called as the actuator disc model, in which, a circular disc replaces the turbine, through which, the streamline flow passes at the U_{∞} velocity.

The following equations presented in this section are based on "Utilized Aerodynamics of Wind Power Machines," Oregon State University [13.14]. The analysis presumes a control volume and needs to consider some assumptions: Wind is steady, homogeneous and has a fixed direction; air is incompressible; so, an unlimited figure of blades needs to be considered in addition to non-rotating wake;

uniform thrust needs to be supposed considering the far up/downstream static pressure of the rotor. A simple schematic of this control volume is illustrated in Figure 1.11.

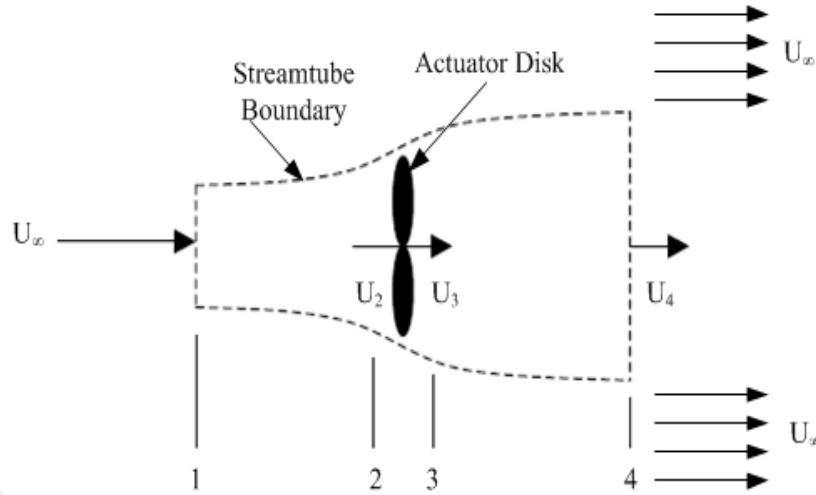


Figure 1.11. Actuator Disk Model of a Wind Turbine [15].

For studying this control volume, 4 regions (Figure 1.11) are required to be considered: 1: free-stream; 2: before-rotor; 3: after-rotor; and 4: far-wake region. For free-stream region, $\mathbf{U}_1 = \mathbf{U}_2$ is assumed.

Applying linear momentum conservation to the control volume considering a steady-state flow; the thrust will be:

$$T = \dot{m}(U_1 - U_4) \quad (1.1)$$

Here, " \dot{m} " represents mass flow rate, so, $\dot{m} = (\rho A U)_1 = (\rho A U)_4$ representing A as the cross-sectional area, ρ the air density while U is velocity of the air.

Here, positive thrust exists; so, behind-the-rotor speed U_4 will be less as compared to U_1 . Because of the frictionless inflow, no work/energy transfer takes place. Bernoulli's principle can be used on the rotor's both sides.

$$p_{1+} + \frac{1}{2}\rho U_1^2 = p_{2+} + \frac{1}{2}\rho U_2^2 \quad (1.2)$$

$$p_{3+} + \frac{1}{2}\rho U_3^2 = p_{4+} + \frac{1}{2}\rho U_4^2 \quad (1.3)$$

Here it's assumed that $p_1 = p_4$ and the velocity across the rotor stays equal $U_2 = U_3$.

The thrust on the rotor disk T is also the differential pressure between stations 2 and 3. The far upstream and far downstream static pressures are equal

$$T = A_2(p_2 - p_3) \quad (1.4)$$

Using Equations 1.2 and 1.3 and substituting them into Equation 1.4:

$$T = \frac{1}{2} \rho A_2 (U_1^2 - U_4^2) \quad (1.5)$$

Recognizing that $\dot{m} = A_2 U_2$, and equating the thrust equations 2.1 and 2.5, we obtained:

$$U_2 = \frac{U_1 + U_4}{2} \quad (1.6)$$

Thus, the wind speed on the rotor plane is obtained by taking the average of the downstream and upstream wind velocities.

An axial induction (or interference) factor "a" measures the influence of the wind when it is slowed down as a result of power extraction by the rotor. It's called as the fractional reduction of the wind speed between the rotor plane and the free stream:

$$a = \frac{U_1 - U_2}{U_1} \quad (1.7)$$

$$U_2 = U_1(1 - a) \quad (1.8)$$

$$U_4 = U_1(1 - 2a) \quad (1.9)$$

The power produced by the rotor " P " happens because of the thrust " T " and the speed of wind speed at U_2 rotor plane.

$$P = T U_2 \quad (1.10)$$

$$P = \frac{1}{2} \rho A_2 (U_1^2 - U_4^2) U_2 \frac{1}{2} \rho A_2 U_2 (U_1^2 - U_4^2) (U_2^2 + U_4^2) \quad (1.11)$$

Substituting for U_2 and U_4 in Equations 1.8 and 1.9 gives:

$$P = \frac{1}{2} \rho A U^3 4a(1 - a)^2 \quad (1.12)$$

Here A replaces the control volume A_2 while U replaced the free stream velocity U_1 [13, 14, 15].

1.6. Methods to Control and Regulate Power in Wind Turbines (Aerodynamic Torque Control)

An approach to control λ is possible by controlling the rotor's aerodynamic torque that ultimately takes place when the rotor L/D is controlled, for which, two further approaches are used:

1.6.1. Stall Regulated Rotor Designs

The stall-regulated rotors have sectional shapes and mean attack angles, which help the rotor to stall on high wind speeds. The stall regulation depends on the rotors' aerodynamic design. The blade design includes a twist to make the blade stall at a certain wind speed to limit the power input.

1.6.2. Pitch Regulated Rotor Designs

Pitch-regulated rotors decrease the aerodynamic torque when it reduces the pitch, and the local angle of attack. The lower attack angles decrease the coefficients of the section lift and the aerodynamic torque.

The pitch control starts with sufficient wind velocity for generating the power level. It continuously reduces the pitch for maintaining optimum λ , and also getting stable power for a certain wind speed. A highly recommended method of affecting the aerodynamic attack angle is controlling the blade pitch angle that reduces the angle of attack, which creates minimal wind energy. Changing the blade's pitch angle is also possible in case of larger attack angle that limits further extracted power increase.

A power curve and axial thrust between pitch regulated and stall regulated blades have been compared and illustrated in Figure 1.12.

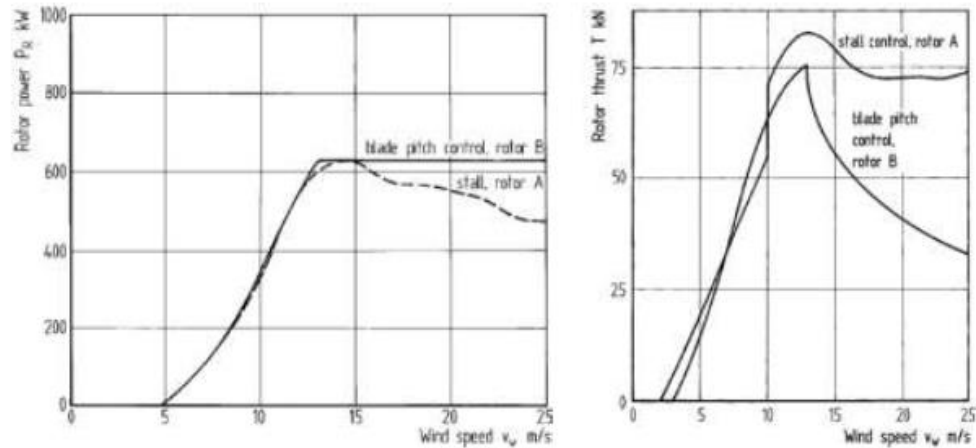


Figure 1.12. Axial Thrust and Power Curve Comparison Between Pitch and Stall Regulated rotors [16,17]

Figure 1.12. clarified that the pitch-regulated blades generate stable power despite lower axial thrust at a high wind speed.

1.7. A brief Review of the Aerodynamic Models

The commercial wind turbine sizes have dramatically increased over the last two and a half decades from almost 50kW with rotor diameter 10-15m. Commercial (5-6 MW) turbines have more than 120m rotor diameter, which facilitates the design tools to consider the highly unsteady aerodynamic loads and their aero-elastic responses such as drive train, tower, control system and rotor [18]. Thus, experts have tried several aerodynamic analytical methods applicable to the wind turbines They include actuator disc method, panel and vortex methods, and line lifting methods:

1.7.1. Blade Element Momentum Method

The calculations of turbine load and performance are performed regularly using the Blade-Element Momentum method [19], which is computationally cheap, reliable and speedy.

The **BEM** process starts with dividing the flow in annular control volumes before applying energy conservation and momentum balance in each control volume. These annuli are stream surface-bound that enclose the rotor extending from far above to down below. The key assumption of the method is that the induced velocity of the rotor should be equal to half induced velocity, which is essential to make the flow analyzable when the blade is divided in many independent elements. In addition, the blade loads are uniform and arranged azimuth-wise that means that the rotor can have infinite number of blades. For every blade element, obtaining the aerodynamic forces is possible through the tabulated airfoil data that starts from measuring wind tunnel, and it is corrected for **3D** effects. The mentioned **BEM** is both a design and a verification process.

1.7.2. Navier-Stokes Solvers

In case of **CFD**, the solution of the governing equations is found using the Navier-Stokes solver. In other words, it can predict the flow fields without entering the values of the airfoil load characteristics. This process is robust, which is its main advantage. It is suitable for all wind speeds, and it can accurately predict **3D** flow characteristics; however, the **CFD** has higher computational time cost. In comparison with other **BEM** methods, **CFD** needs higher computational power, which makes it less suitable for the designs, in which, large number of design variables have to be parametrically changed. Because of the high computational power progress of most of the computing devices, using **CFD** is possible while conducting parallel computations in large clusters [20, 21].

RANS solver is utilizable for expected aerodynamic loads on **NREL Phase VI** [22]. When the steady state flow simulation for **NREL Phase VI** rotor blade were accomplished, the **CFD** results showed agreement with the empirical results [23]. Computational researches were conducted on **HAWT** applying RANS choosing different turbulence models. They are mentioned in the references section [24, 25]. Consequently, the **RANS** approach is more effective and useful as compared to simpler processes, for instance, **BEM**.

1.8. Energy Situation of Libya

Power outage is a major issue in today's Libya, and it has emerged as a serious issue. Since the power generation has been constant for decades while the demand for electricity has increased, the power crisis has aggravated. Libyan power generation institutions, power plant owners, and concerned government organizations expect that the need for electricity will increase by two and half times by the end of 2020. The power production levels [26] and survey statistics indicate that despite the fact that Libya is a small country, and its population is only 6.5 million, its power consumption is the highest in Africa.

In Libya, the per capita power requirement was 4.60 Kwh in 2009 [27], which significantly rose and eventually exceeded the power production. The last survey was conducted in Libya in 2012 when the total power generation was 33.980 Gwh, which shows 4.37% increase as compared to 2010, also shown in Table 1.1. In Libya, the overall power production in 2012 was 6,798MW. Studies and estimates show that the power production did not exceed 48.497 Gwh in 2017 while the energy requirement was as high as 87.935 Gwh [26]. The annual *GECOL* report shows that the Libyan energy consumption has significantly increased, as Figure 1.10 indicates. The regression equation is derived expecting that the load will grow at approximately 6.7% per annum as Figure 1.10 shows.

It must be realized that Libya needs to accomplish a lot in terms of overcoming its energy crisis, which requires good strategic planning, new projects and all possible measures to improve the power generation capacity of the country. Experts suggested mixed power production sources, but Libya has no prior history of initiating such projects such as renewable energy-based and nuclear power plants. Libya is rich in terms of renewable energy resources specifically wind and solar energy. This is obvious from the global renewable energy distribution maps as well as some studies [26, 27]. This opportunity is magnanimous for two reasons: first, its large areas are empty, and that empty part has rich exposure to sunlight and the second is wind energy because in some areas, the velocity of wind is 5 to 10m/s. The vast coastal areas of the country have a 1900 km feasible area with power generation possibilities using the tidal and wave energy [26, 27].

Until now, the renewable power generation technology is not so developed, so it is not enough to single-handedly deal with the Libyan energy crisis; however, it can meet a significant part of the total demands and minimize issues such as pollution and global warming. Focusing on renewable energy sources should be a focus for all governmental energy policies, plans, and initiatives.

Table.1.1: Total Energy Production and Consumption (2010 - 2012) [26]

Item	2010	2012	Change (%)
Max.Load (Mw)	5,759	5,981	3.85
Min.Load (Mw)	2,103	2,080	-0.1
Total Energy Production (Gwh)	32,558	33,980	4.37
Energy Imported (Gwh)	70.331	61.020	-13.24
Energy Exported (Gwh)	152.152	14.419	-90.52
Customers	1,198,176	1,223,727	2.13
Energy Sold Mwh	20,602,217	12,993,675	-36.93
Number of Employee	37,586	40,000	6.0
Consumption Per Capita (Kwh)	4,651	4,850	4.37

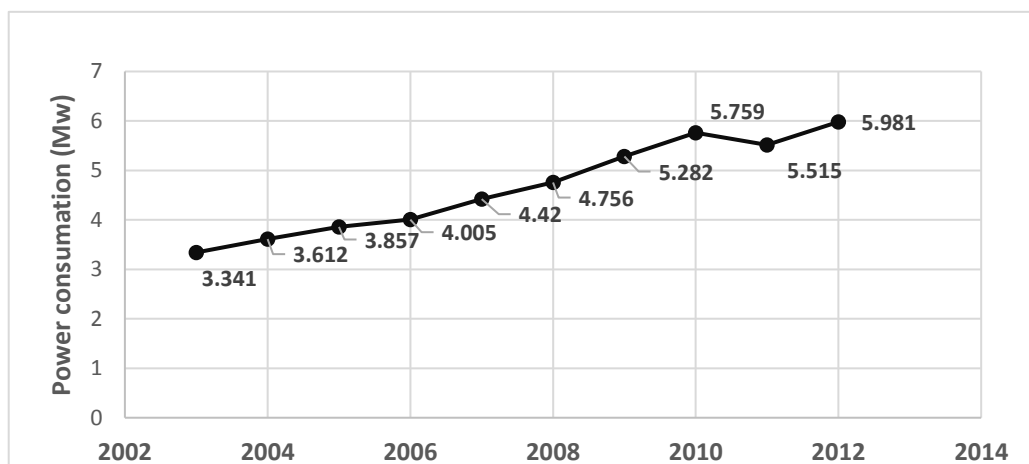


Figure 1.13: The Energy Consumption over the last 10 years [27]

1.9. Wind in Libya

Wind energy is the second best alternative renewable energy source. The wind speed in some coastal districts is illustrated in Figure 1.14.



Figure 1.14: The wind speed in coastal cities in Libya, [28]

The Libyan renewable power generation plan is shown in Figure. 1.15. [29]. The scheme is divided into four basic stages. Due to the instability in Libya, this project has been suspended. At present, the 6% target has not been completely achieved because of the instability. Additionally, there is no political will to launch these projects. As an example of the inappropriate planning, the first stage of the plan was to construct a 60MW wind farm in the city of Dernah, and the project continued from 2008 to 2012. It had 37 wind turbines with capacity to generate 1.65MW each. Then a dispute started over the possession of the land, after which, this project was delayed.

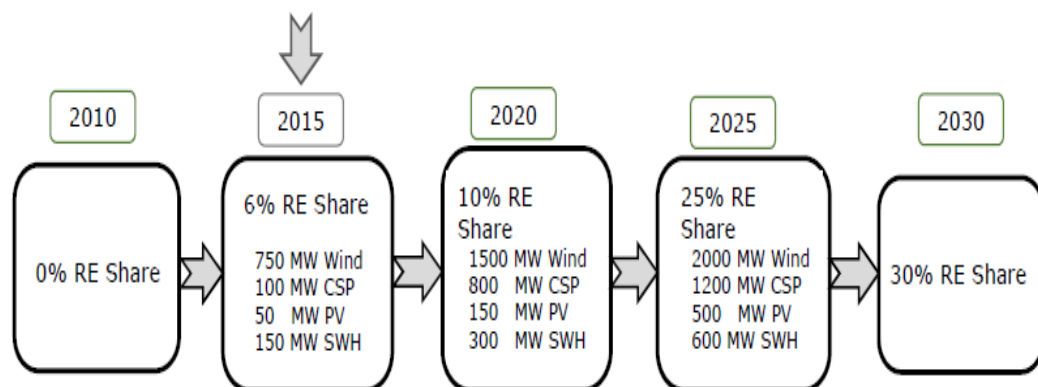


Figure 1.15: The Libyan Renewable Energy Plan (Source: Planning and Studies Department, REAOL)

1.10. Literature Review

Both population and the manufacturing industry are growing all over the world, which means that the demand for energy is increasing. Fossil fuel-based energy sources have negative effects on the environment, and they are running out. Alternative renewable sources must be developed. Wind energy is a renewable energy source that has been widely developed and used in the recent years. Libya is a rapidly growing consumer of energy and the demand for electricity increases by 10-15% every year [30]. Libya has the highest electricity generation and consumption per capita in Africa. The average consumption has increased from 2.60 kWh in 2000 to 4.60kWh in 2009, and since then, it is slowly increasing [31].

Libya is considered as an oil-rich country; however, maintaining the standard of living for the coming generations by decreasing the greenhouse gases is mandatory for this country. In addition to that, power outage has recently become a crisis in Libya. The demand for energy is always more than the energy production.

The data obtained from the wind map and the satellite show that Libya has great potential in terms of wind-based power generation. In many areas, the wind speed remains between 6-7.5m/s at a height of 40m, which is suitable for power generation [32].

There are few studies about wind energy in Libya; El-Osta et al. [33] selected a small wind farm of 1.5MW to make it a pilot wind project. They investigated different sites in Tripoli and Zwara and selected a site for their project. The analysis was conducted using WAsP software. The average wind speed was 6.9m/s at 10m height with available power 399W/m². Their results were promising for the wind farm project.

El-Osta and Khalifa [34] conducted a pre-feasibility study for a 6MW wind farm in Zwara site. They used the RETScreen software for the economic evaluation of the project. Their results show that the project was feasible.

El-Osta et al. [35] evaluated the potential of the wind energy in the central part of the Libyan coast and predicted the wind power generation capacity at different heights. The outcomes of their efforts clearly indicate that less than 1% of the total area was adequate to supply the total needed electric energy. They termed the wind power generation potential in Libya as "high and promising."

Mohammed et al. [31] investigated the utilization of renewable energy in Libya. They concluded that Libya has large renewable energy including wind energy resources but needs more comprehensive energy strategies and more financial as well as educational investments.

M. S. Elmnefi and A. M. Bofares [30] have taken wind speed measurements for 12 months period at Benina site in Libya. The results showed an average 11m/s wind speed at 10m height, which indicates the high wind power generation potential in the Benina site.

Dimitrios Mentis et al. [36] evaluated the African wind energy potential using a GIS system. Their report shows that the Libyan coast is appropriate for installing wind power projects.

Y. Song and J. B. Perot [37] conducted simulations of both turbulent as well as potentially separating flows around a twisted, rotating, and tapered airfoil, which is challenging for CFD simulations. The simulation outcomes showed good agreement with the NREL experimental results for wind speed less than 10m/s when the blades were not fully stalled. The inlet wind speed was more than 10m/s, and at that speed, the researchers observed significantly large differences between the results of simulations and experiments.

N.N. Sorensen and J.A. Michelsen [38] conducted a series of computations during the NREL Phase-VI rotor's upwind operations for zero, yaw, and zero-degree tip-pitch. The current paper shows both computations, which are performed after and before the release of the results from the wind tunnel measurements.

1.11. Scope of the Study

The main purpose of this study is to analyze the wind data of four sites in Libya and to predict the annual energy that can be obtained, and the cost of Kwh per site, as well as the impact of the size of the turbine in terms of cost and production.

- Assessment of wind turbine and prediction Annual energy for four sites in Libya
- Study the preconditioning effects on wind turbine CFD simulations. Since the Mach number is very low, preconditioners are needed.
- Study different low Reynolds number turbulence models on one test case and see which one gives closer results to experiments.

- Study the effect of sizing and pitch on the power performance of HAWT. The NREL Phase VI is baseline blade for this study.

1.12 . Thesis Outline

The current thesis consists of 6 chapters.

Chapter 1: Introduction to wind turbines, their history, regulation methods, use of aerodynamic energy in Libya and literature review.

Chapter 2: Technical and economical evaluation analysis of wind power generation in four sites using different Weibull parameters.

Chapter3: Computational fluid dynamic and numerical solution applied for simulation. This chapter also states different turbulence models and preconditions for the RANS solver. Information pertaining to the boundary conditions has been mentioned.

Chapter 4: A test case has been investigated and analyzed in the NREL Phase VI. The results have been compared with the experimental results for two different turbulence models. This chapter is important because it validates the solver and helps choosing the most suitable turbulence model for further simulations.

Chapter 5: Predictions regarding optimum pitch angle, blade size, and the *AEP* have been carried out in this chapter besides carrying out the cost analysis of baseline wind turbine, wind turbine with optimum pitch and wind turbine with different scales.

Chapter 6: Conclusion.

Chapter 2

Technical and Economical Evaluation Analysis of Wind Power Generation in Four Sites Using Different Weibull Parameters

The feasibility of wind energy development depends on the particular social, economic, and physical characteristics of both study area and the wind resource.

The study deals with analysis of four methods for determining the parameters of the Weibull distribution, using wind speed data collected in the *REAOL* Libya. The Weibull distribution is a two-parameter function commonly used to fit the wind speed frequency distribution. This family of curves has been shown to give a good fit to measured wind speed. Three methods for calculating the parameters of the Weibull wind speed distribution for wind energy analysis are presented: The *Graphical Method (GM)*, the Empirical method (*EM*), the Maximum likelihood method (*MLM*), the proposed Energy pattern factor method. The application of each method is demonstrated using a sample wind speed data set and a comparison of the accuracy of each method is also performed using some statistical methods of analysis. The study helps to determine which one is effective in determining the parameters of Weibull distribution and to establish the wind energy resource

2.1. WIND DATA

Knowledge of the characteristics of the wind regimes in any location is important in the evaluation and usage of wind resources. The present study is to carry out wind energy assessment for 4 different sites (Almqrun, Tolmeta, Tarhuna and Alazeeziya) located along the Libyan coast as shown in Figure 2.1.



Figure 2.1. The Location of the Sites in Libya.

The assessment includes annual energy production and capacity factor calculations and cost analyses to check for the feasibility of the sites. The assessment is based on real measurements of wind speeds at different heights. The data were obtained from the Libyan Meteorological Authority and New & Renewable Energy Authority in Libya. Table 2.1 shows the physical features of the meteorological stations.

Table 2.1. Physical Features of the Meteorological Stations

Station (Site)	Latitude	Longitude	Altitude (m)
Tolmeita	32.42178°	20.56388°	80
Almqrun	31.43784°	20.14928°	65
Alazeeziya	32.31550°	13.01030°	180
Tarhuna	32.26020°	13.38040°	398

The wind speeds were measured for each site at three different heights; 20m, 40m and 60m. The mean wind speed is the most commonly used indicator of wind energy potential. It is defined as [39]:

$$V_m = \frac{1}{N} \sum_{i=1}^N v_i \quad (2.1)$$

Where, V_m , is the mean wind speed, v_i is the hourly measured wind speed and N is the number of measured hourly wind speed data. Tables 2.2, 2.3 and 2.4 show the monthly and annual averages of the measured wind speeds in each site at heights of 20m, 40m and 60m respectively.

Table 2.2. Average Wind Speeds at 20 m Height

Site	Monthly Average Wind Speeds (m/s)												Annual Averages (m/s)
	Jan.	Feb.	Mar	Apr.	May	Jun.	Jul.	Aug	Sep.	Oct.	Nov.	Dec.	
Tolmeta	5.94	4.89	5.13	5.30	3.70	3.32	3.02	2.87	4.42	4.09	5.10	6.17	4.50
Almqrun	4.47	4.59	5.29	5.47	5.28	5.08	5.22	4.70	4.62	3.76	4.09	5.06	4.80
Alazeeziya	5.50	6.72	6.58	7.57	5.78	6.18	4.67	5.47	5.01	6.11	5.90	6.12	5.97
Tarhuna	5.63	7.26	6.80	9.66	6.88	7.37	5.95	6.38	6.41	7.02	6.15	5.60	6.76

Table 2.3: Average Wind Speeds at 40 m Height

Site	Monthly Average Wind Speeds (m/s)												Annual Averages (m/s)
	Jan.	Feb.	Mar	Apr.	May	Jun.	Jul.	Aug	Sep.	Oct.	Nov.	Dec.	
Tolmeta	6.51	4.89	5.53	5.77	3.90	4.46	3.16	2.87	4.69	4.40	5.56	6.75	4.87
Almqrun	5.25	5.33	6.07	6.22	5.93	5.66	5.84	5.27	5.23	4.42	4.85	5.87	5.50
Alazeeziya	6.40	7.49	7.92	9.25	7.36	7.81	6.14	6.97	6.39	7.25	6.88	7.12	7.25
Tarhuna	6.05	7.59	7.23	10.0	7.16	7.77	6.18	6.73	6.72	7.44	6.65	5.91	7.12

Table 2.4. Average Wind Speeds at 60 m Height

Site	Monthly Average Wind Speeds (m/s)												Annual Averages (m/s)
	Jan.	Feb.	Mar.	Apr.	May	Jun.	Jul.	Aug.	Sep.	Oct.	Nov.	Dec.	
Tolmeita	7.25	5.57	5.96	6.27	4.23	3.64	3.16	3.01	5.00	4.82	6.02	7.45	5.22
Almqrun	6.12	6.04	6.86	7.04	6.59	6.26	6.53	5.91	5.89	5.12	5.72	6.71	6.24
Alazeeziya	6.63	8.19	8.15	9.52	7.44	7.94	6.15	7.11	6.48	7.47	7.12	7.39	7.47
Tarhuna	6.74	8.78	8.39	11.5	8.48	8.98	7.44	7.88	7.84	8.47	7.31	6.68	8.70

From the table 2.4 above, the maximum value (11.54 m/s) was measured at height of 60 m at Tarhuna in April while the minimum average value (3.01 m/s) was measured Tolmeita in August. Figures 2.2, 2.3 and 2.4 show a comparison of the monthly mean wind speeds between the sites for different heights.

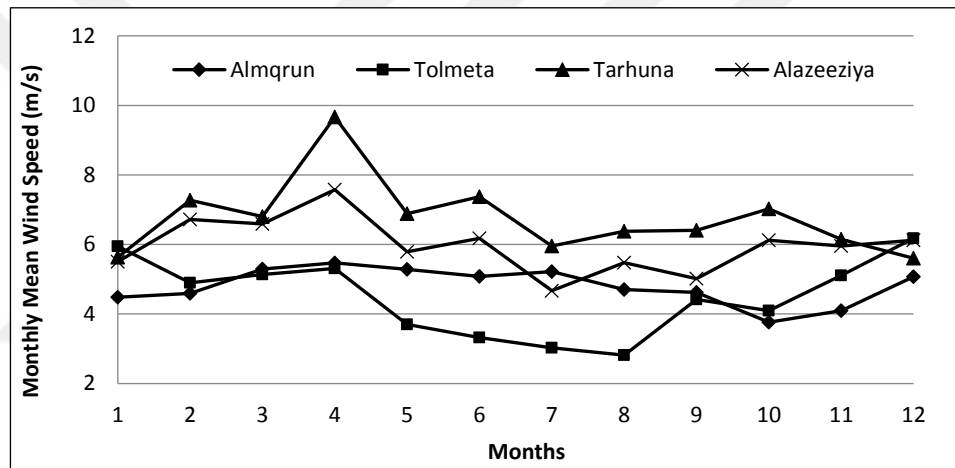


Figure 2.2. Monthly Variation of Wind Speeds for the Selected Sites at 20m Height

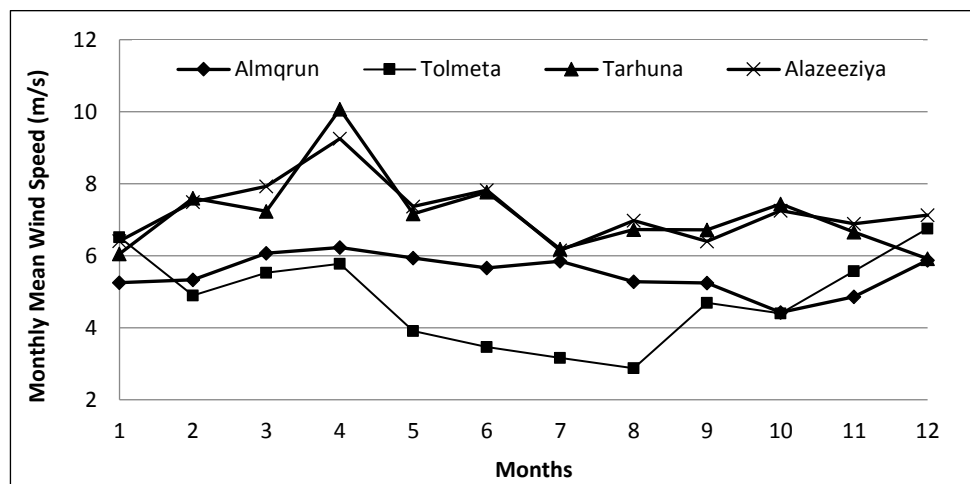


Figure 2.3. Monthly Variation of Wind Speeds for the Selected Sites at 40m Height

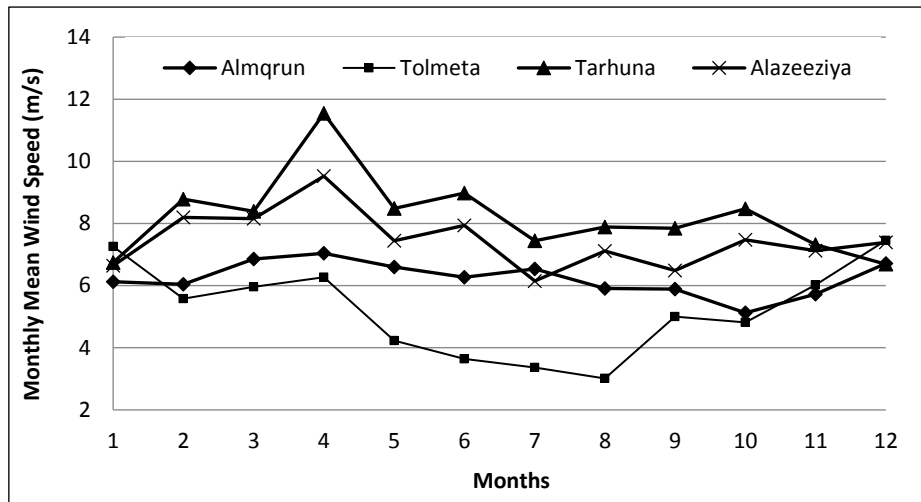


Figure 2.4. Monthly Variation of Wind Speeds for the Selected Sites at 60m Height

The figures show that Tarhuna and Alazeeziya have the highest mean wind speeds along the year and their highest wind speeds were recorded in April. On the other hand, Tolmeta has the lowest wind speeds compare to the other sites along the year.

From this point after, the measurements that will be considered for further investigations are the ones correspond to 60m height. The annual mean wind speeds for the different sites at 20m, 40m and 60m heights are shown below:

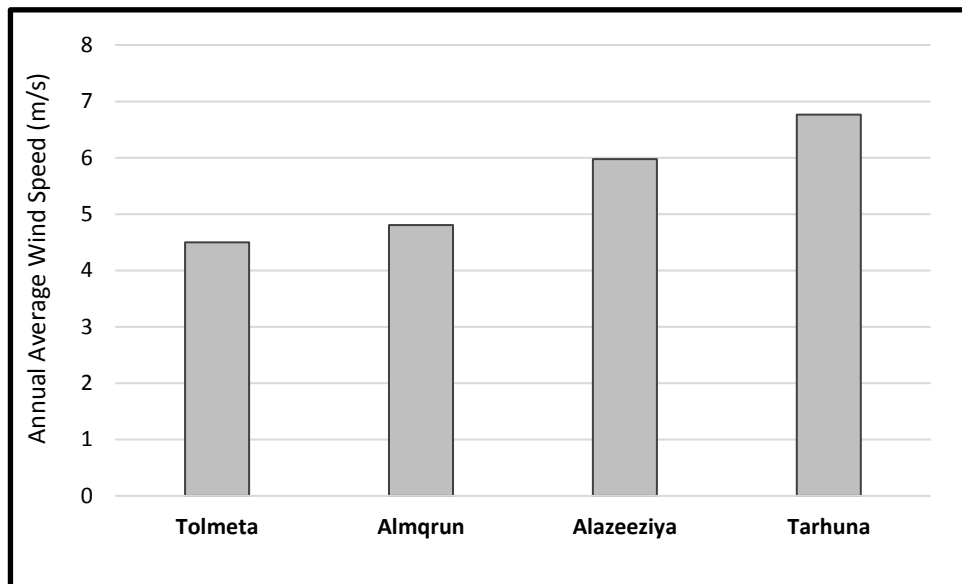


Figure 2.5. Annual Mean Wind Speeds for the Selected Sites at 20m Height

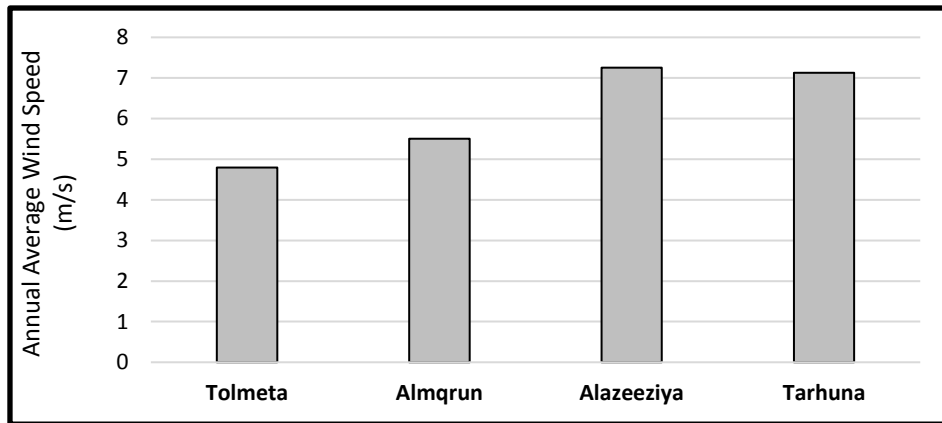


Figure 2.6. Annual Mean Wind Speeds for the Selected Sites at 40m Height

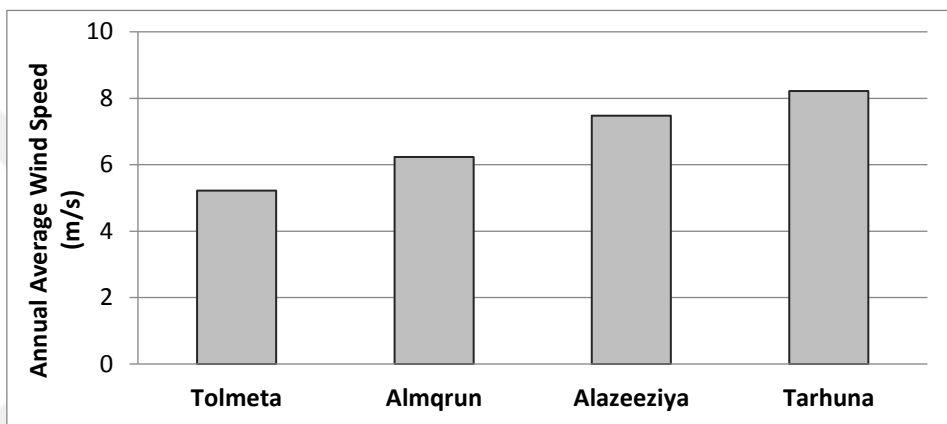


Figure 2.7. Annual Mean Wind Speeds for the Selected Sites at 60m Height

The measured annual wind speed frequency curves are plotted for all the sites in Figures 2.8, 2.9 and 2.10.

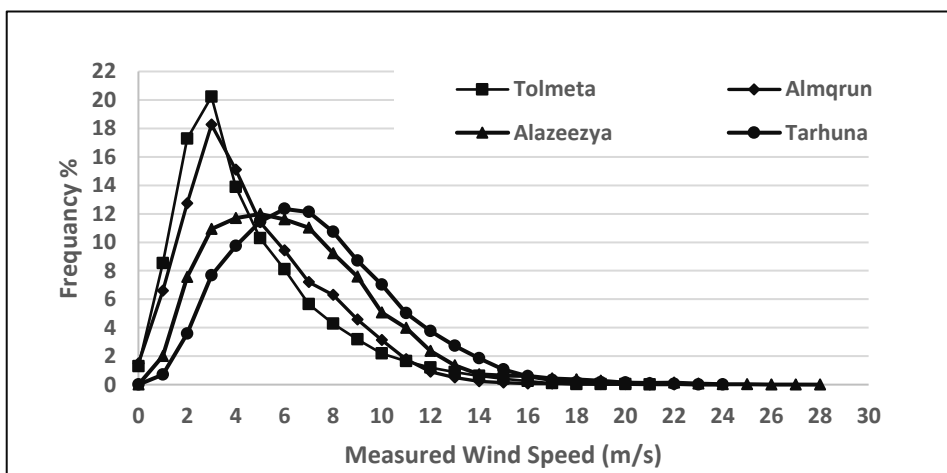


Figure 2.8. Measured Annual Frequency Distribution at Height 20 m

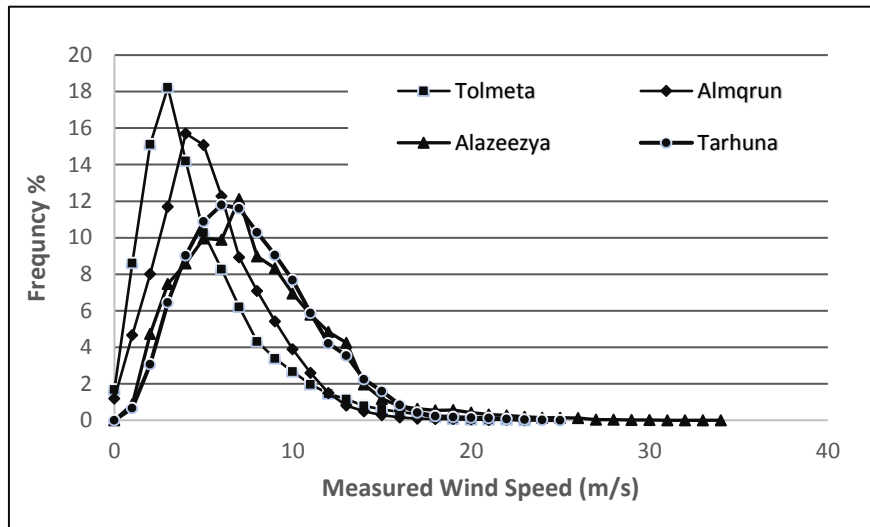


Figure 2.9. Measured Annual Frequency Distribution at Height 40 m

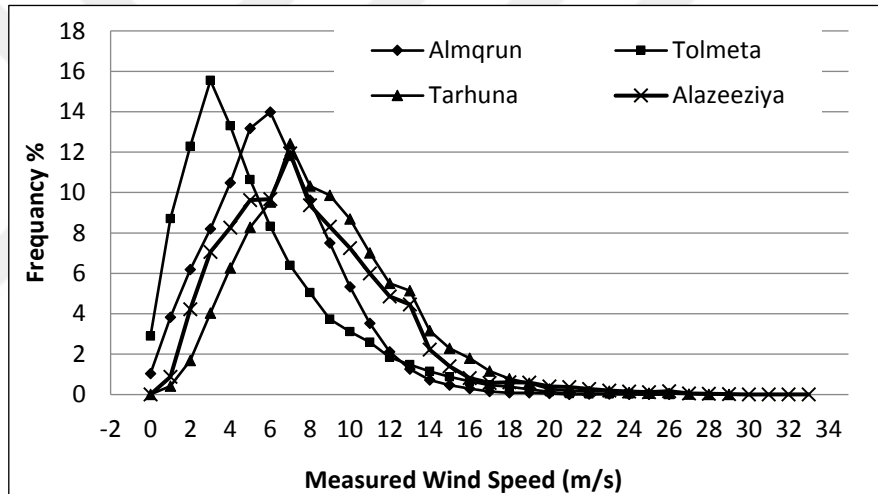


Figure 2.10. Measured Annual Frequency Distribution at Height 60 m

From Figure 2.10 one may notice that the distribution curves of the sites have similar trends, they increase to reach a peak value and decrease after that. The peak value is close to the annual mean speed of a certain site. All the sites have a peak value between 12 % and 16 %.

2.2. Analysis Method

The main purpose of this study is to calculate the annual energy production for each of the selected sites as well as carry out cost analysis. To calculate the annual energy production, information about the Probability Density Function (*PDF*) and Cumulative Distribution Function (*CDF*) should be known. Typically, the *PDF* is given by either

Rayleigh or Weibull distribution. The Rayleigh PDF and **CDF** are given by the mean velocity only as [39]:

$$PF(v) = \frac{\pi}{2} \left(\frac{v}{v_m^2} \right) \exp \left[-\frac{\pi}{4} \left(\frac{v}{v_m} \right)^2 \right] \quad (2.2)$$

$$F(v) = 1 - \exp \left[-\frac{\pi}{4} \left(\frac{v}{v_m} \right)^2 \right] \quad (2.3)$$

The Weibull distribution considers some corrections to account for the site conditions (e.g. landscape, vegetation and obstacles). Those corrections are modeled through a shape factor, **k**, and scale factor, **c**, as below [39]:

$$PF(v) = \left(\frac{k}{c} \right) \left(\frac{v}{c} \right)^{k-1} \exp \left[-\left(\frac{v}{c} \right)^k \right] \quad (2.4)$$

$$F(v) = 1 - \exp \left[-\left(\frac{v}{c} \right)^k \right] \quad (2.5)$$

Where, **PF(v)**, is the probability density function, **F(v)**, is the cumulative distribution function and, **v**, is the wind speed. In this study the more general Weibull distribution which is in agreement with many other works [40-43] will be used. However, first the Weibull parameters, **k** and **c**, must be found for each site. There are different ways to estimate the Weibull parameters. Three methods will be used in this study as shown in the discussion below:

2.2.1. Graphical Method (GM)

The Graphical Method is used to estimate the Weibull parameters from the measured wind speed data. Equation 2.5 can be written as:

$$1 - F(v) = \exp \left[-\left(\frac{v}{c} \right)^k \right] \quad (2.6)$$

Taking the double logarithmic transformation of Equation (2.6):

$$\ln[-\ln(1 - F(v))] = k \ln v - k \ln c \quad (2.7)$$

Plotting $\ln[-\ln(1 - F(v))]$ versus $\ln v$ will yield approximately a straight line. The gradient of the line is **k** parameter and the intercept with **y**-axis is $-k \ln(c)$.

2.2.2. Empirical Method (*EM*)

The empirical method is considered as special case of the moment method, where the Weibull parameters, k , and, c , are given by the equations shown below [44]:

$$k = \left(\frac{\sigma}{V_m} \right)^{-1.086} \quad (2.8)$$

$$c \approx \frac{V_m k^{2.6674}}{0.184 + 0.816 k^{2.73855}} \quad (2.9)$$

Where, σ , is the standard deviation of the observed data defined as [45]:

$$\sigma = \sqrt{\frac{1}{N-1} \sum_{i=1}^N (v_i - V_m)^2} \quad (2.10)$$

2.2.3. Maximum Likelihood Method (*MLM*)

The Maximum Likelihood Estimation method (*MLM*) is a mathematical expression known as a likelihood function of the wind speed data in time series format used to estimate the parameters, k and, c , by the following formula [40]:

$$k = \frac{\pi}{\sqrt{6}} \left[\frac{N(N-1)}{N(\sum \ln^2(v_i)) - (\sum \ln(v_i))^2} \right]^{0.5} \quad (2.11)$$

$$c = \left(\frac{\sum (v_i)^k}{N} \right)^{\frac{1}{k}} \quad (2.12)$$

2.3. Error Analysis

The error analysis is carried out to verify the accuracy of the Weibull distributions which are obtained by the different methods mentioned in the previous section. To do so, the coefficient of determination, R^2 , the Root Mean Square Error, *RMSE*, the Mean Bias Error, *MBE*, and the Mean Bias Absolute Error, *MAE*, are calculated. The coefficient of determination, R^2 , is the square of the ratio between the Weibull frequencies to the actual frequencies. It is defined in Eq. (2.13) [46,47,48,49]

$$R^2 = \frac{(\sum_{i=1}^N (y_i - z_i)^2 - \sum_{i=1}^N (y_i - x_i)^2)}{\sum_{i=1}^N (y_i - z_i)^2} \quad (2.13)$$

Where, N , is the number of observations (number of actual data), y_i , is the actual frequency, x_i , is the Weibull frequency and, z_i , is the average wind speed. The root mean Square Error, **RMSE**, is a measure of the residuals between Weibull frequency and the actual frequency. It is defined in Eq. (2.14) as [46,49,50]:

$$RSME = \sqrt{\frac{1}{N} \sum_{i=1}^N (y_i - x_i)^2} \quad (2.14)$$

The Mean Bias Error, **MBE**, is a measure of how closely the Weibull frequencies match with the actual frequencies. It is calculated from Eq. (2.15) [46,47,48,50].

$$MBE = \frac{1}{N} \sum_{i=1}^N (y_i - x_i) \quad (2.15)$$

Similarly, the Mean Bias Absolute Error, **MAE**, is another measure found from Eq. (2.16) [46,47,48,49]

$$MAE = \frac{1}{N} \sum_{i=1}^N |y_i - x_i| \quad (2.16)$$

2.4. Weibull Parameters

The Weibull parameters are calculated using the three different methods mentioned above. The results corresponding to the graphical method are obtained from the plots shown in Figures 2.11, 2.12 and 2.13.

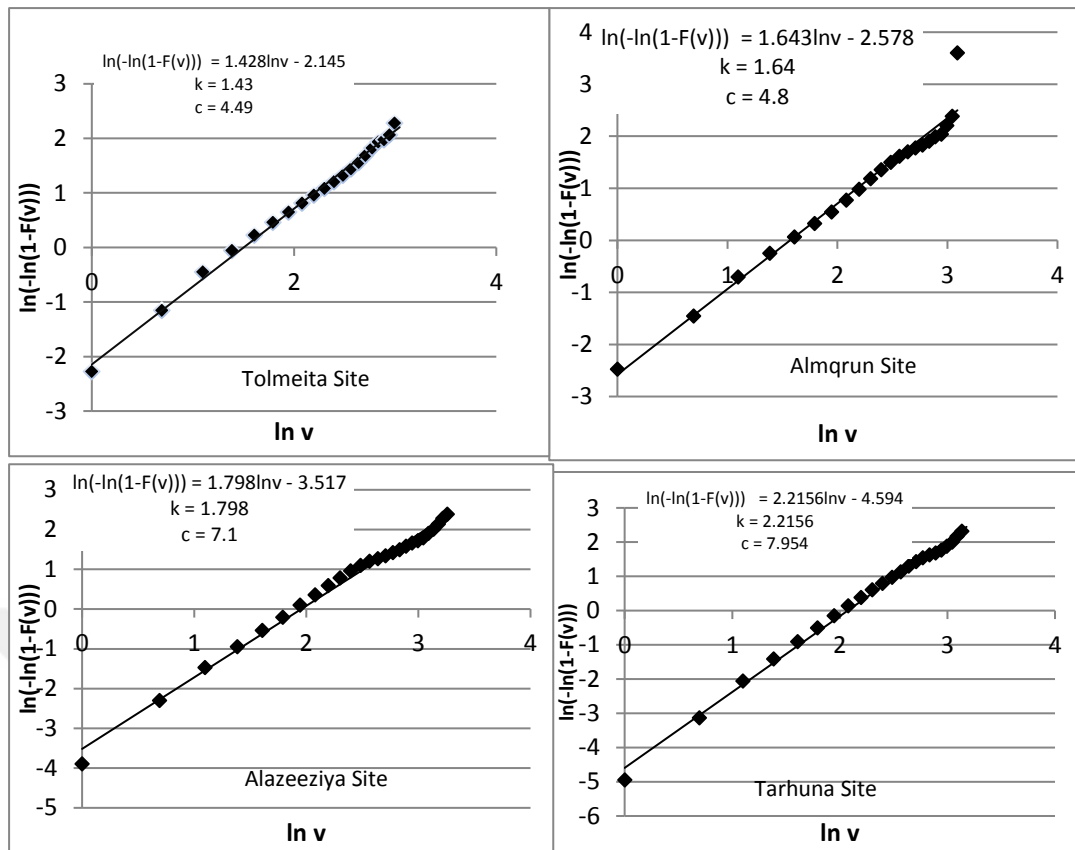


Figure 2.11. Graphical Method to Estimate the Weibull Parameters at 20m

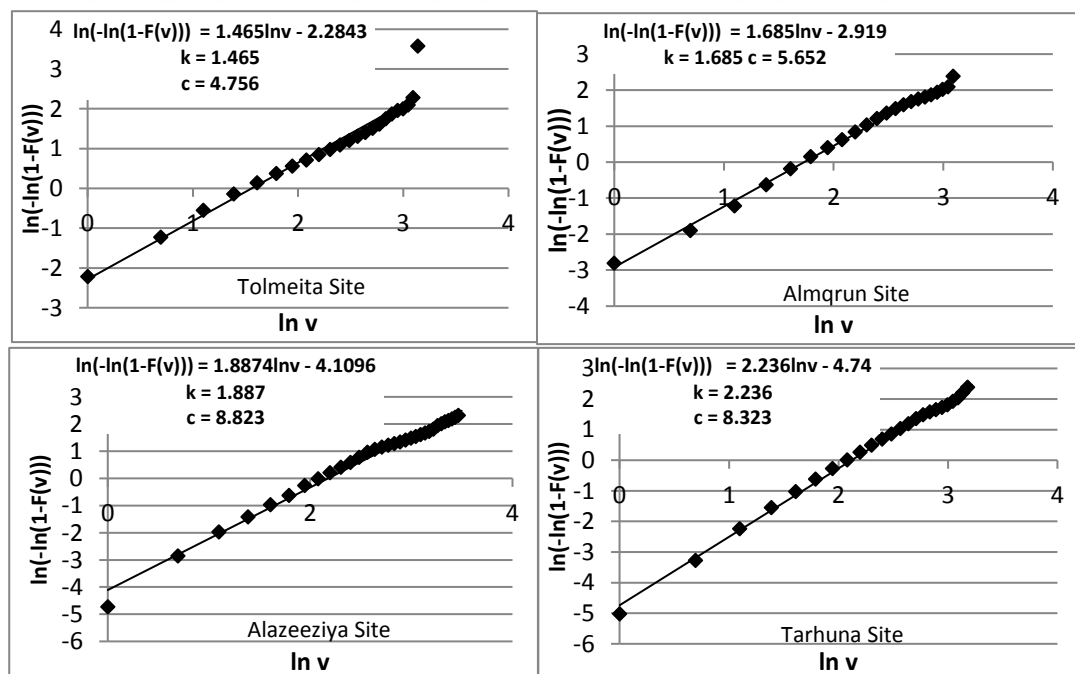


Figure 2.12. Graphical Method to Estimate the Weibull Parameters at 40m

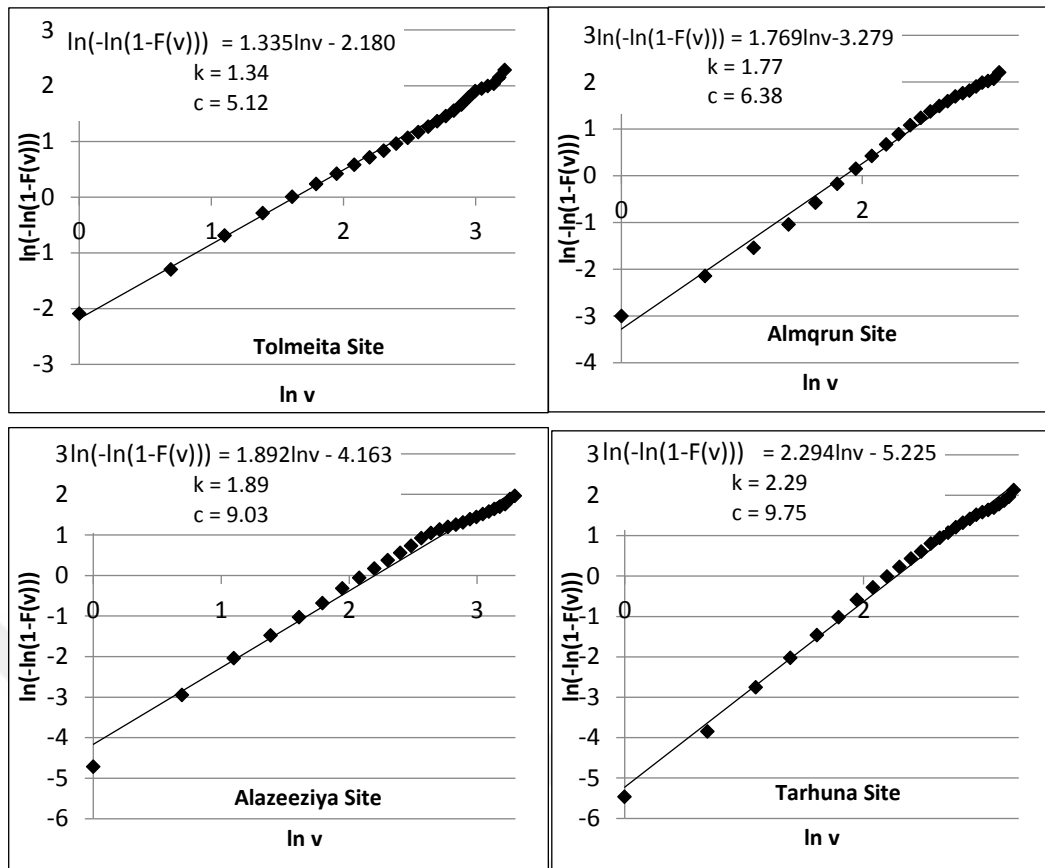


Figure 2.13. Graphical Method to Estimate the Weibull Parameters at 60m

The Weibull parameters results for the different sites at 20m, 40 and 60m height are shown in Tables 2.5, 2.6 and 2.7.

Table 2.5. Weibull Parameters Estimated by Three Methods at 20m Height

Site	Methods					
	GM		EM		MLM	
	k	c	k	c	k	c
Tolmeta	1.43	4.49	1.77	5.87	1.92	5.33
Almqrn	1.64	4.8	2.08	7.05	2.00	5.59
Alazeeziya	1.79	7.1	2.25	9.00	2.22	7.52
Tarhuna	2.21	7.95	2.60	9.80	2.55	8.34

Table 2.6. Weibull Parameters Estimated by Three Methods at 40m Height

Site	Methods					
	GM		EM		MLM	
	k	c	k	c	k	c
Tolmeta	1.463	4.756	1.62	5.83	1.84	5.66
Almqrun	1.68	5.65	2.18	7.05	2.11	6.32
Alazeeziya	1.8874	8.823	2.08	9.00	2.28	9.06
Tarhuna	2.2368	8.324	2.59	9.80	2.55	8.74

Table 2.7. Weibull Parameters Estimated by Three Methods at 60m Height

Site	Methods					
	GM		EM		MLM	
	k	c	k	c	k	c
Tolmeta	1.34	5.12	1.43	5.73	1.72	6.09
Almqrun	1.77	6.38	2.12	7.05	2.12	7.06
Alazeeziya	1.89	9.03	2.04	9.0	2.29	9.27
Tarhuna	2.29	9.75	2.42	9.81	2.64	10.02

The results show that all the methods give close estimation for the Weibull parameters to each other. However, **MLM** gave higher values for the parameters in all the sites. On the other hand, **GM** gave lower values for the parameters in Almqrun and Tolmeta, where the mean wind speeds are lower, and middle values for Tarhuna and Alazeeziya sites, where the mean wind speeds are higher. This difference in the results will affect the technical and economical predictions as shown in the next sections.

The errors associated with the different Weibull methods are calculated using equations (2.13-2.16) and for the example at 60 m the error results are shown in Table 2.8. The small values for **RSME**, **MBE** and **MAE** verify that the methods for calculating the Weibull parameters in this study are accurate and can be used for wind energy assessment. Also, the **R²** values are close to **1.0** for all the methods in all the sites which proves the accuracy of the used methods once more.

Table 2.8. Error Analysis Results.

Site	Method	R^2	RSME	MBE	MAE
Tolmeita	GM	0.99287	0.02877	7.81E-05	0.00034
	EM	0.99576	0.02218	5.25E-05	0.00027
	MLM	0.99335	0.02778	2.07E-05	0.00041
Almqrun	GM	0.98842	0.03603	1.64E-05	0.00050
	EM	0.99837	0.01353	4.04E-06	0.00018
	MLM	0.99831	0.01376	4.18E-06	0.00019
Alazeeziya	GM	0.99831	0.01938	5.81E-06	0.00028
	EM	0.99905	0.01457	3.38E-06	0.00021
	MLM	0.99863	0.01746	1.18E-06	0.00031
Tarhuna	GM	0.99821	0.01606	1.06E-06	0.00022
	EM	0.99860	0.01421	5.88E-07	0.00019
	MLM	0.99781	0.01780	1.83E-07	0.00027

2.5. Probability Density and Cumulative Distribution Functions

The probability density function and cumulative distribution function are calculated by substituting the Weibull parameters, k , and, c , into equations 2.4 and 2.5. The probability density function indicates the frequency of the wind blowing at a certain speed. The calculated probability density function using Weibull parameters computed from different methods are fitted against the frequency of the actual wind data in Figures below. Figure 2.14, 2.15 and 2.16 show that for the sites where the wind speed is low (Tolmeita and Almqrun) the computed *PDF* deviates from the actual data. For the other two sites (Alazeeziya and Tarhuna), where the wind speed is high, it is noticed that the computed probability density function matches well with the actual data for all the used methods with the *MLM* giving better agreement with the actual data for all the sites.

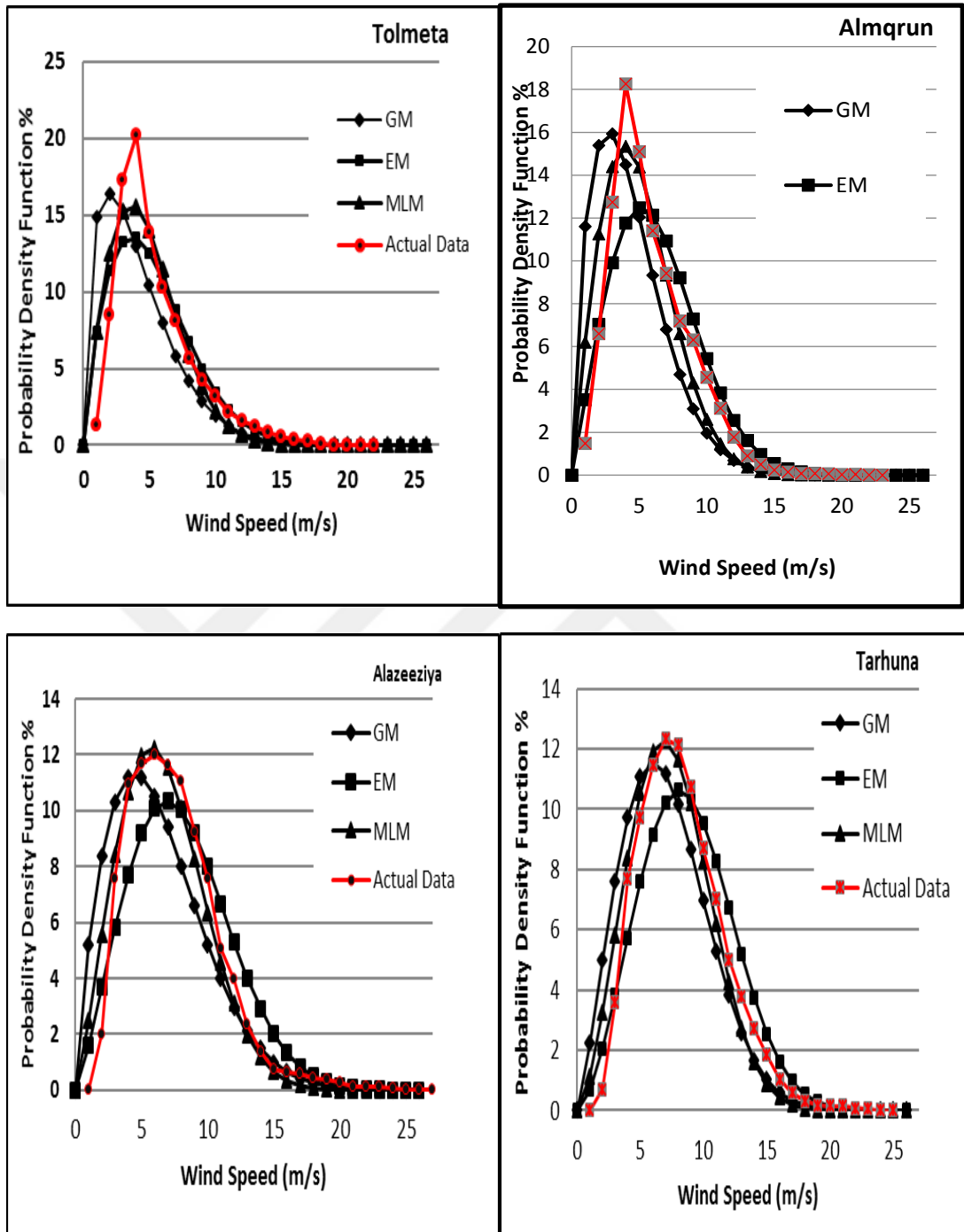


Figure 2.14. Probability Density Function for the Sites at 20m Height.

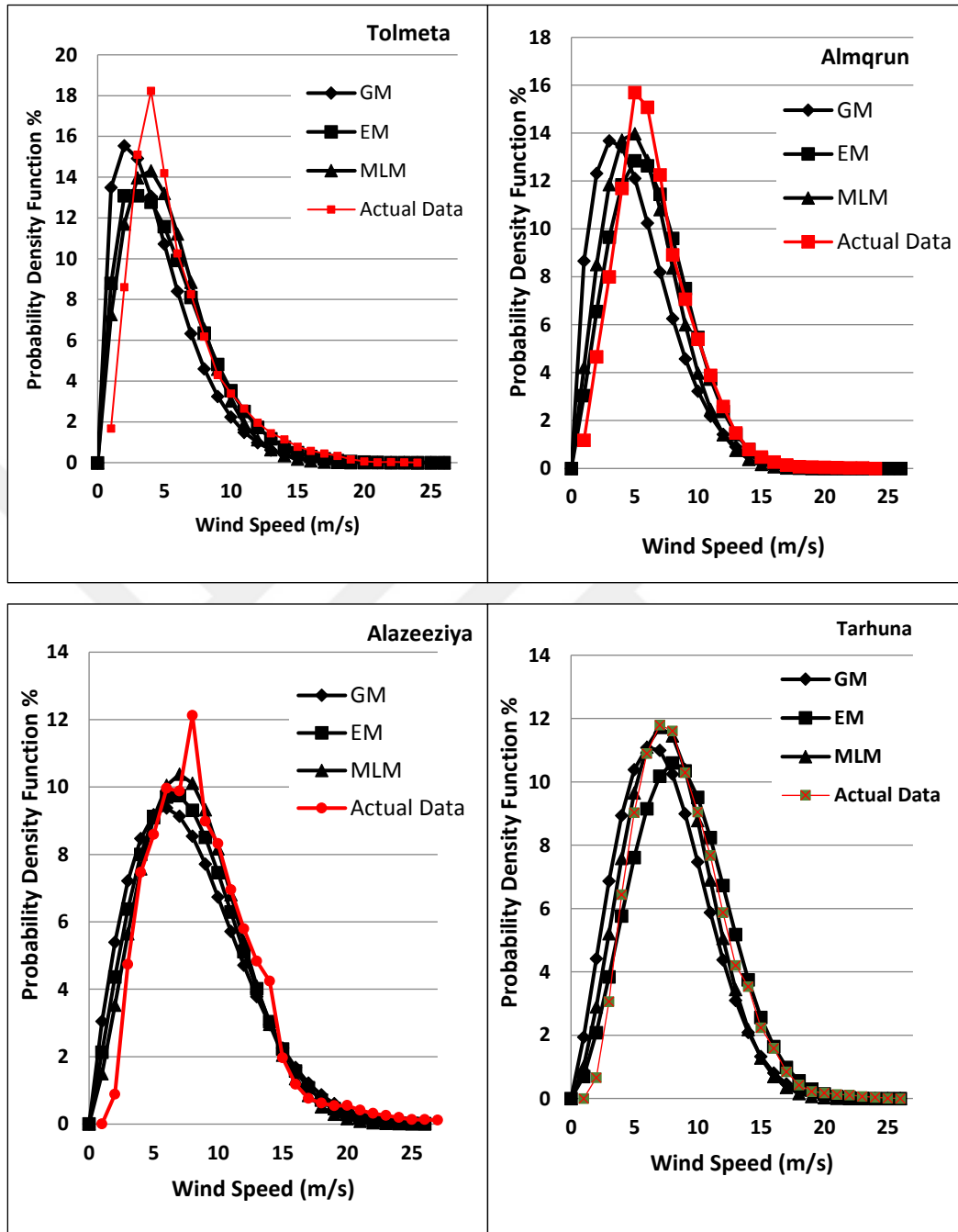


Figure 2.15. Probability Density Function for the Sites at 40m Height.

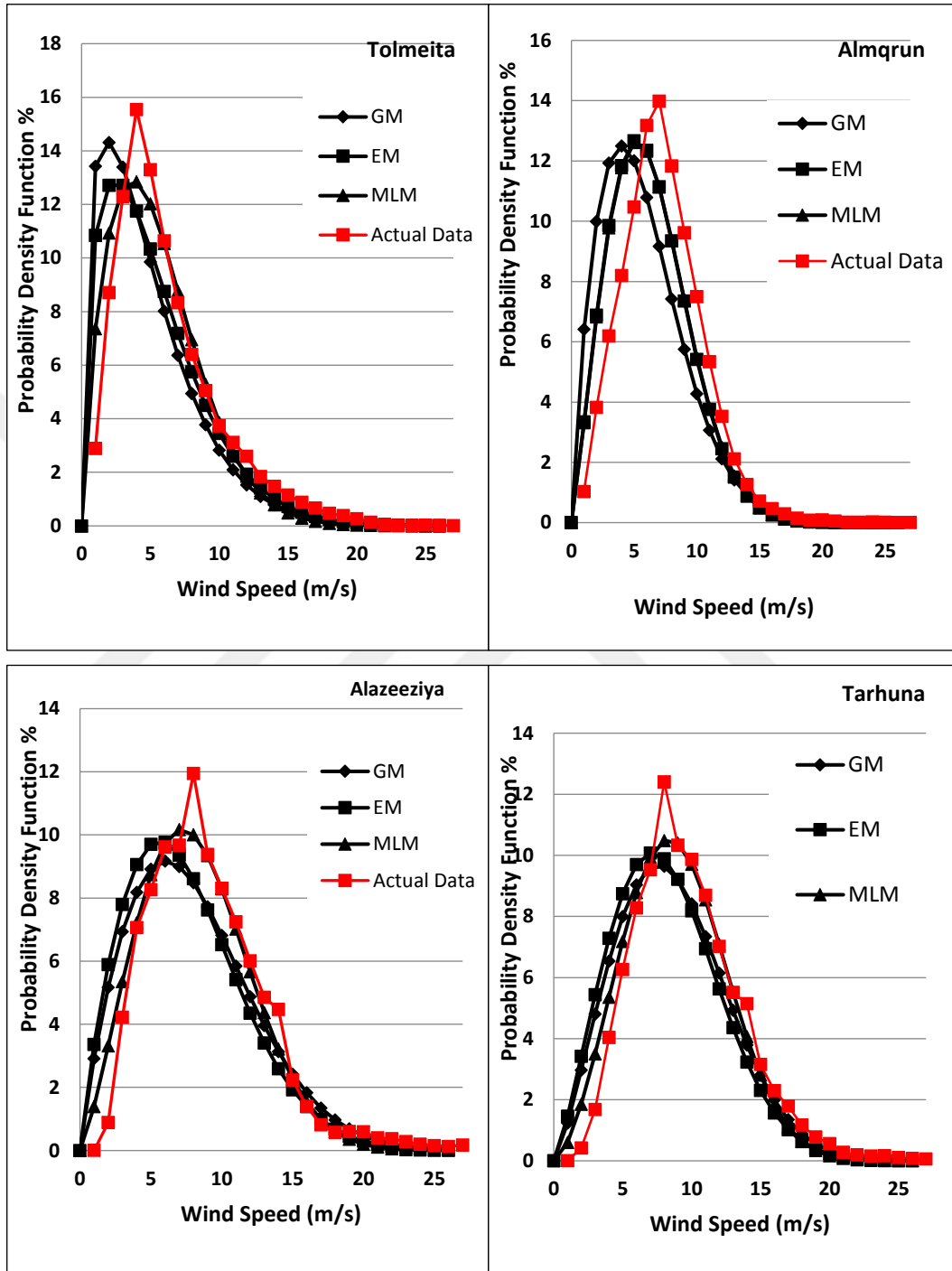


Figure 2.16. Probability Density Function for the Sites at 60m Height

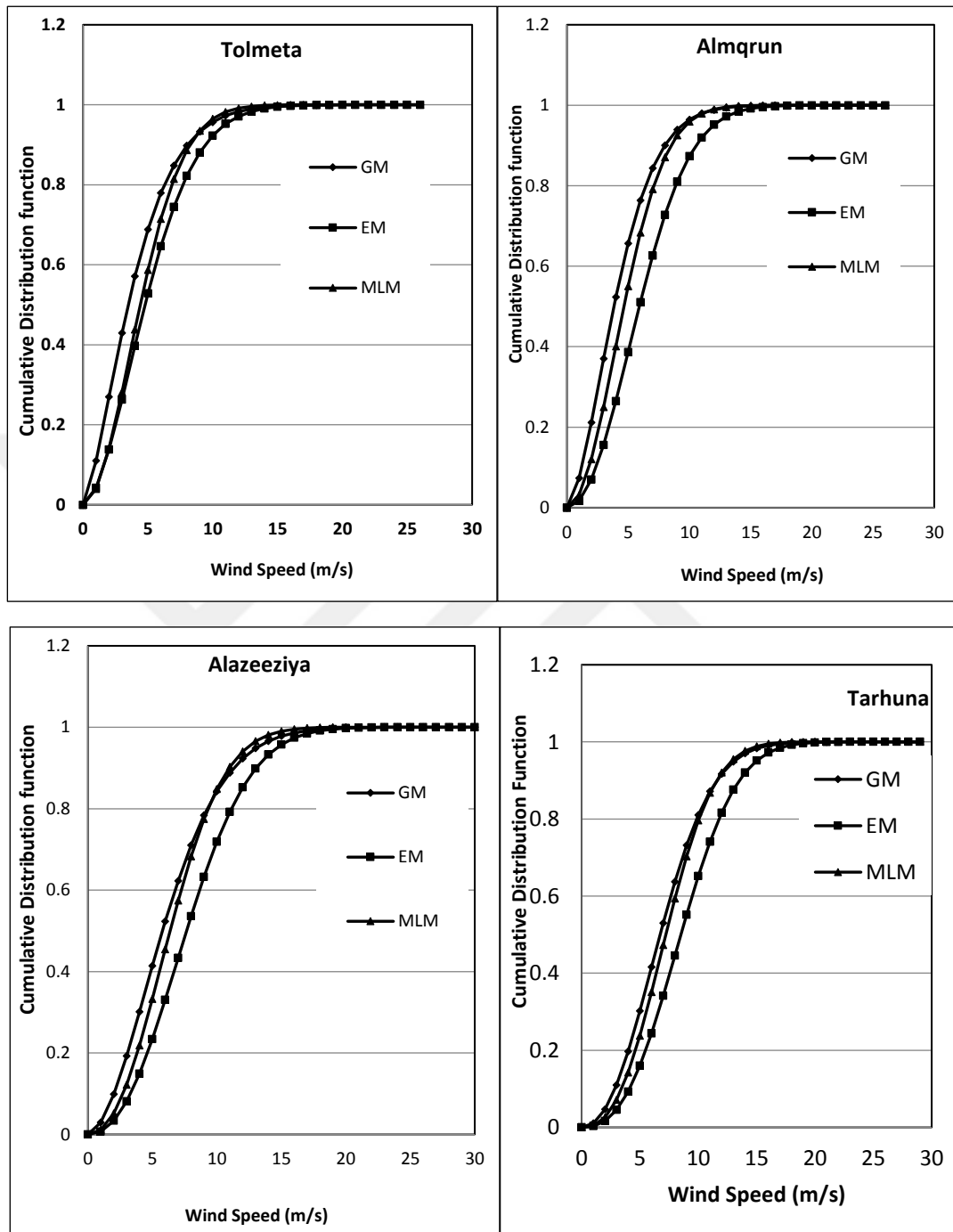


Figure 2.17. Cumulative Distribution Function for the Sites at 20m Height.

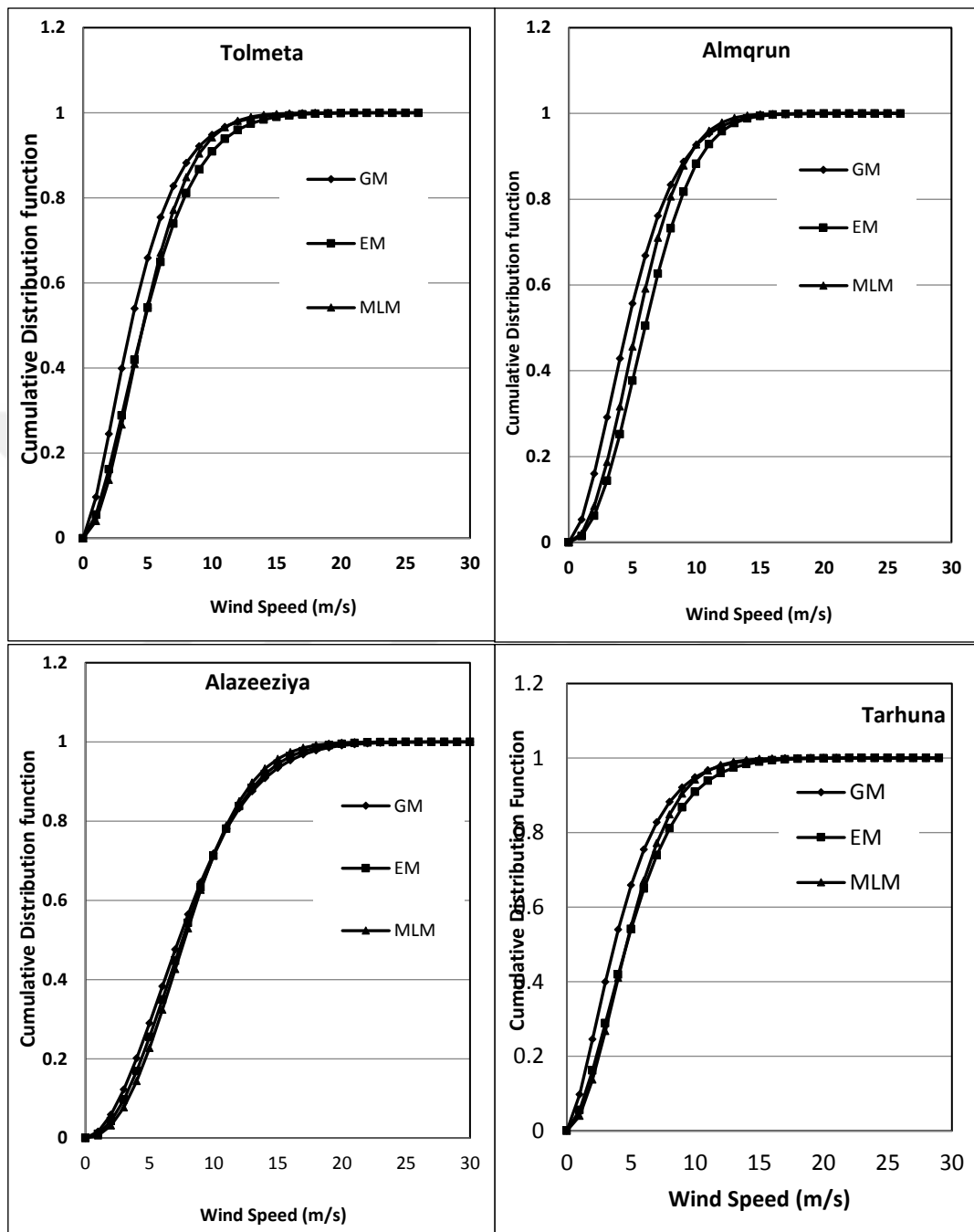


Figure 2.18. Cumulative Distribution Function for the Sites at 40m Height.

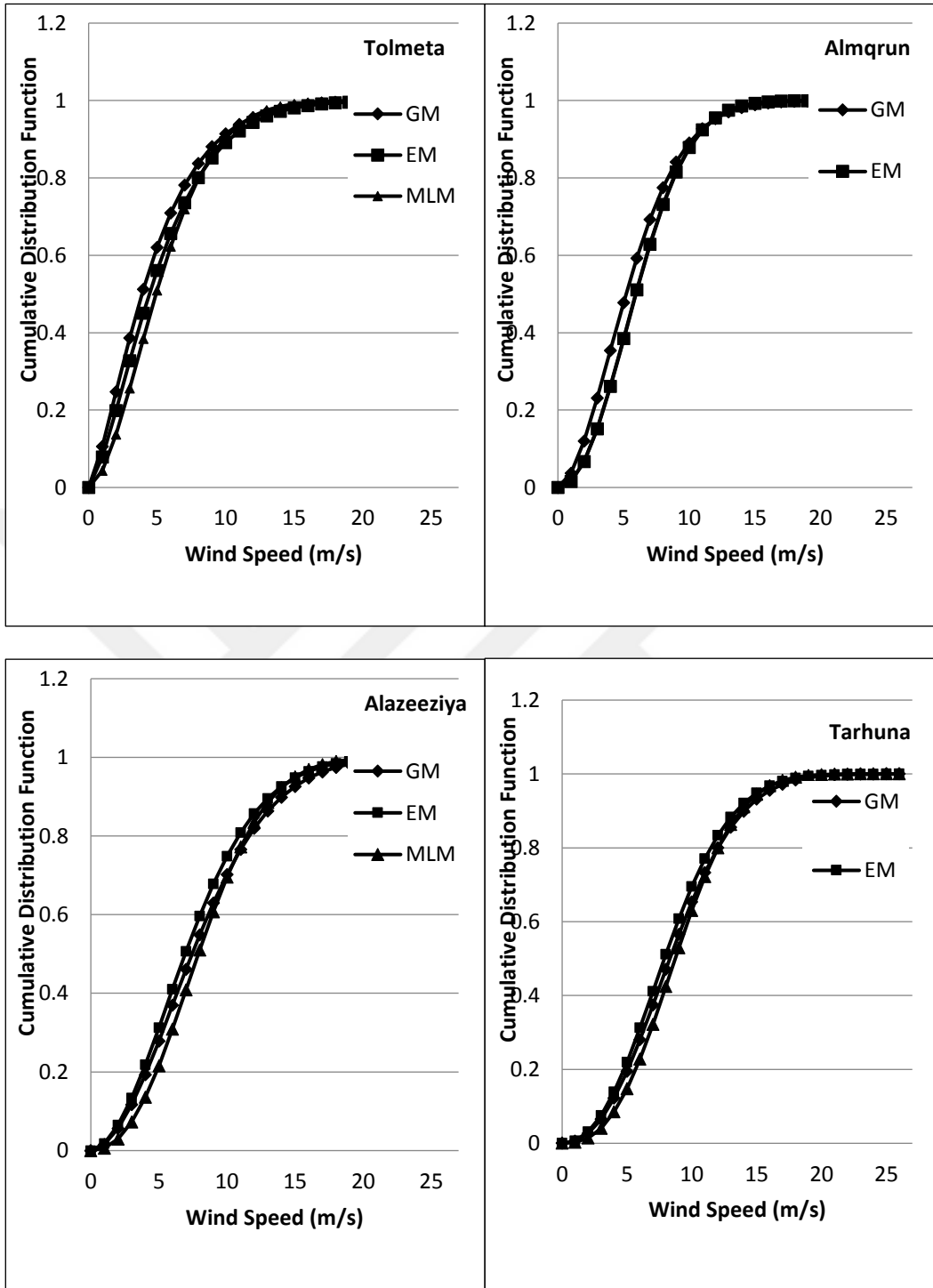


Figure 2.19. Cumulative Distribution Function for the Sites at 60m Height.

The results in Figures 2.17, 2.18 and 2.19 show once again that all the methods give closer results to each other.

2.6. Annual Energy Production and Capacity Factor

The annual energy production calculations are very vital in the evaluation of any wind energy project. The long-term wind speed distribution is combined with the power curve of a specific wind turbine to give the energy generated at each wind speed and hence the total energy generated overall the year. The annual energy production (*AEP*) can be expressed mathematically as follow [51]. The probability that a wind speed v_0 will fall between two wind speeds v_i and v_{i+1} is obtained from the cumulative distribution function as:

$$F(v_i < v_0 < v_{i+1}) = \exp\left[-\left(\frac{v_i}{c}\right)^k\right] - \exp\left[-\left(\frac{v_{i+1}}{c}\right)^k\right] \quad (2.17)$$

The total annual energy production is calculated as:

$$AEP = \sum_{i=1}^{N-1} \frac{1}{2} [P(v_{i+1}) + P(v_i)] \cdot F(v_i < v_0 < v_{i+1}) \cdot 8760 \quad (2.18)$$

Where, $P(v_i)$ is the power output of a certain wind turbine at wind speed v_i and **8760** is the number of hours in the year.

Another important measure for the wind turbine productivity is the capacity factor, C_f , defined as the ratio of the actual yearly energy generated to the yearly energy produced by the wind turbine if it had run at its rated power.

$$C_f = \frac{\text{energy generated per year (Kwh)}}{\text{wind turbin rated power (kw)} \times 8760} \quad (2.19)$$

To calculate *AEP* and C_f , information about a certain wind turbine must be available including the power curve. In this study the selected model wind turbine is Enercon *E53-800 kW*. This turbine has a relatively low rated wind speed and an available hub height of 60m (the same height at which the measured wind data are available). The technical specifications and power curve of this turbine are given in Table 2.9 and Fig.2.20[52]

Table 2.9. Technical Specifications of the Model Wind Turbine

Item	Description
Turbine Model	Enercon E53-800 kW
Configuration	Three blade, horizontal axis, upwind
Rated Power	800 kW
Cut-in wind speed	2 m/s
Rated wind speed	12 m/s
Cut-out wind speed	28 – 34 m/s
Rotor Speed	12 – 28.3 RPM
Rotor diameter	52.9 m
Swept area	2,198 m ²
Hub height	60 m
Estimated unit price	1,230,000 USD

The power curve of the turbine is shown in Figure 2.20.

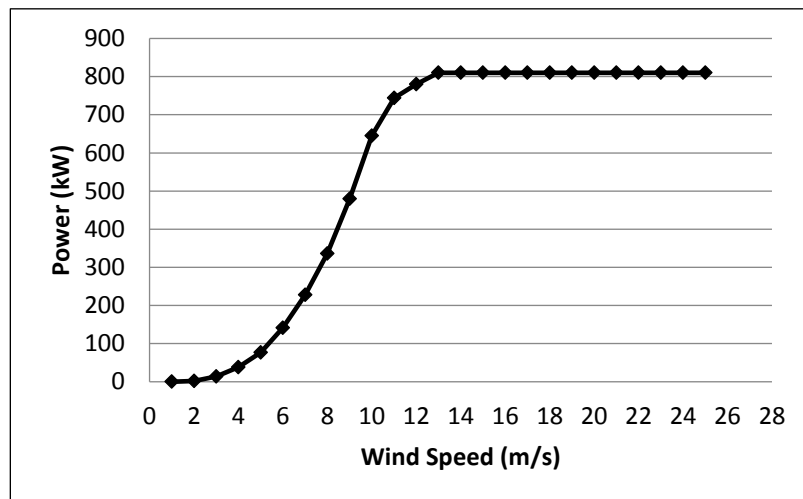


Figure 2.20: Power Curve of the Model Wind Turbine

The hub height is **60m** which means that the wind data measured at **60m** can be used in the calculations without the necessity for hub height extrapolation.

Using equations (2.17-2.19), the annual energy production and capacity factor can be calculated. The results for *AEP* and *C_f* are shown in Table 6 for the different Weibull methods.

Comparison of the annual energy production among the sites is shown in Fig. 2.21. Table 2.10 and Fig.2.21 show that, for the low wind speed cases (Tolmeita and Almqrn), EM and MLM methods yield close estimations for *AEP* to each other. On the other hand, at high wind speeds (Alazeeziya and Tarhuna), *GM* and *EM* give close results to each other.

As seen in Table 2.10, the capacity factor for Alazeeziya and Tarhuna is very high. This high value in *C_f* means that the wind in those sites used to blow at a speed close to the rated speed of the wind turbine. In fact, from the wind data of the sites, the frequency of wind speeds above 10 m/s was around 30 % for Alazeeziya and 35% for Tarhuna. On the other hand, for Tolmeita and Almqrn sites, the wind speed frequency for speeds above 10 m/s were only 9.5% and 11% respectively.

Table 2.10. Annual Energy Production and Capacity Factor for All Sites for 60m

Site	GM		EM		MLM	
	AEP (kWh)	<i>C_f</i> (%)	AEP (kWh)	<i>C_f</i> (%)	AEP (kWh)	<i>C_f</i> (%)
Tolmeita	1326254	18.92	1579265	22.54	1635920	23.34
Almqrn	1779710	25.40	2069157	29.53	2087639	29.79
Alazeeziya	3174948	45.30	3194849	45.59	3389674	48.37
Tarhuna	3639931	51.94	3710428	52.95	3888651	55.49

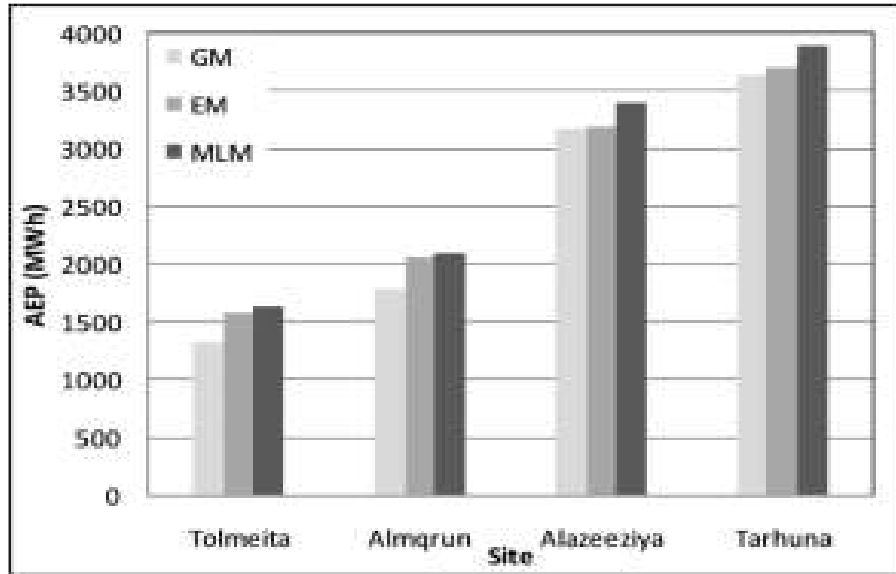


Fig. 2.21. Comparison of *AEP* Among the Sites Using Different Weibull Methods for **60m**

2.7 Present Value Cost and Electricity Price

To calculate the present value cost, *PVC*, the values of the different terms in Eq. (2.20) should be known. In this study those values have been calculated based on the values in [53,54,55]. The calculated and assumed terms are listed in Table 2.11.

$$PVC = I + C_{omr} \left[\frac{1+i}{r-i} \right] \times \left[1 - \left[\frac{1+i}{1+r} \right]^t \right] - S \left[\frac{1+i}{1+r} \right]^t \quad (2.20)$$

Table 2.11. The Values of the Terms in the Present Value Cost Equation.

Term	Assumed/Calculated Value
Turbine Life, <i>t</i> 20 years	20 years
Investment, <i>I</i>	1,476,000 USD
Operation, Maintenance and Repair cost, <i>Comr</i>	15,375 USD
Inflation Rate, <i>i</i>	0.12
Interest Rate, <i>r</i>	0.15
Scrap Value, <i>S</i>	147,600 USD

Those values are used for all the studied sites in this study. The turbine cost was estimated according to [56] as 1600 USD/kW. The cost of each kWh produced by the turbine in, USD cent/kWh, is calculated from Eq. (2.21). The results of the electricity price for each site are shown in Table 2.12.

$$KWh\ price = \frac{PVC}{AEP \times T} \times 100 \quad (2.21)$$

Table 2.12. Electricity Cost of Each kWh for Each Site.

Site	Electricity (USD cent/Kwh)		
	GM	EM	MLM
Tolmeita	6.13	5.14	4.97
Almqrun	4.56	3.93	3.89
Alazeeziya	2.56	2.54	3.40
Tarhuna	2.23	2.19	2.09

Those calculated electricity costs correspond to the minimum price at which the electricity produced by the wind turbine should be sold such that the turbine will be able to payback itself within the specified turbine life. Table 2.12 shows that the **GM** method, gives higher values for the electricity cost for all the site while **MLM** gives lower results. The average difference in the electricity cost between **GM** and **MLM** is around 13% all over the sites. For the low wind speed sites (Tolmeita and Almqrun), the difference in the electricity cost estimation is in the range of 20%. Where, for the high wind speed sites (Alazeeziya and Tarhuna), the difference decreases to around 7.0 %.

According to statista website, the electricity tariff in 2015 is between 6 cent/kWh and 15 cent/kWh with an average of about 11 cent/kWh in Europe and 9.43 cent/kWh in USA. The average price in the world is around 8 cent/kWh. This means that, even using the **GM** method which gives the highest price, still wind energy projects in the selected sites would be feasible especially in Tarhuna and Alazeeziya. And the

outcome of the turbines would cover the turbine cost in fewer years than the assumed turbine life time.

2.8. Greenhouse Gases Emission Reduction

GHG reduction is calculated from Eq. (2.22). In this study, the base case emission factor for Libya is published by the International Energy Agency [57] as, 0.87 tCO₂/MWh. Since the proposed case is the wind turbine which makes use of wind energy for electricity generation, the proposed case **GHG** emission factor is taken as zero. The **T&D** losses factor is suggested by RETScreen [58] to be 16% for the developing countries such as Libya. Assuming that there is no credit transfer fee, one may take, **ecr**, equals to zero. Using the annual **GHG** reduction formula (Eq. 2.22) and substituting the above data together with the calculated annual energy production for each site, the annual **GHG** reduction can be calculated. The annual **GHG** reduction results are shown in Table 2.13.

$$\Delta GHG = (e_{base} - e_{prop}) E_{prop} (1 - \lambda_{prop}) (1 - e_{cr}) \quad (2.22)$$

Where, **e_{base}**, is the base case **GHG** emission factor (tCO₂/MWh), **e_{prop}**, is the proposed case **GHG** emission factor (tCO₂/MWh) and, **E_{prop}**, is the proposed case annual electricity produced (MWh). **E_{prop}**, is the annual electricity produced by the wind turbine in the different sites calculated previously. **λ_{prop}**, is the fraction of the electricity loss in transmission and distribution (**T&D losses**) for the proposed case and, **ecr**, is the **GHG** emission reduction credit transaction fee.

To see the **GHG** reduction effect on the cost analysis, we need to know the price of tons of CO₂. Using the same cost analysis stated before and adding the **GHG** reduction effect, the new electricity cost is calculated form Eq. (2.23).

$$KWh \text{ Cost} = \frac{PVC \text{ without } GHG - \text{price of annual } GHG \text{ red} \times t}{AEP \times t} \times 100 \quad (2.23)$$

Table 2.13. Annual GHG Reduction for Each Site.

Site	Annual GHG Reduction (tCO ₂ /MWh)		
	GM	EM	MLM
Tolmeita	980.4	1167.4	1209.3
Almqrun	1315.6	1529.5	1543.2
Alazeeziya	2346.9	2361.6	2506.6
Tarhuna	2690.6	2742.7	2874.5

Again, one notices that the different Weibull methods determine different values for the annual **GHG** reduction with **GM** giving the lowest values while **MLM** gives the highest values.

To see the GHG reduction effect on the cost analysis, a knowledge of the price of tons of CO₂ is needed. According to P. Luckow et al [59], the mid case CO₂ forecast shows that the price of CO₂ will start at \$20 per ton in 2020 and will increase to \$26 per ton in 2030. In this analysis, a lower price of \$8 per tCO₂ will be used to increase the reliability of the results. The new electricity price is calculated from Eq. (2.23). The results of the updated electricity cost after adding the **GHG** reduction effects are shown in Table 2.14. Comparing the results in Table 2.14 with the ones in Table 2.12, it is observed that the electricity cost has been reduced by an average of around 18% after adding the **GHG** reduction effects to the cost calculations.

Table 2.14. Cost of kWh for each Site Considering the GHG Reduction Effect

Site	Electricity cost with GHG effect (USD cent/kWh)		
	GM	EM	MLM
Tolmeita	5.53	4.55	4.37
Almqrun	3.97	3.33	3.30
Alazeeziya	1.97	1.95	1.81
Tarhuna	1.64	1.60	1.50

Chapter 3

Computational Fluid Dynamic and Numerical Solution

The fluid flow is mathematically explained with the help of equations pertaining to momentum, conservation of mass, and energy. The partial differential equations (*PDEs*) describe the fluid as a continuous medium. These techniques were used for solving the problem by replacing *PDEs* by algebraic equations when the physical domain was divided into several discrete control volumes. They are termed as cells or elements. These cells show algebraic relationships as to how the flow variables including temperature, velocity, and pressure vary in the local settings with space coordinates, which is the main idea behind *Computational Fluid Dynamics*. On the other hand, Computational Fluid Dynamics (*CFD*) simulates fluid engineering systems with the help of mathematical modeling as well as solvers, discretization methods, grid generation, and numerical parameters. It is described in Figure 3.1.

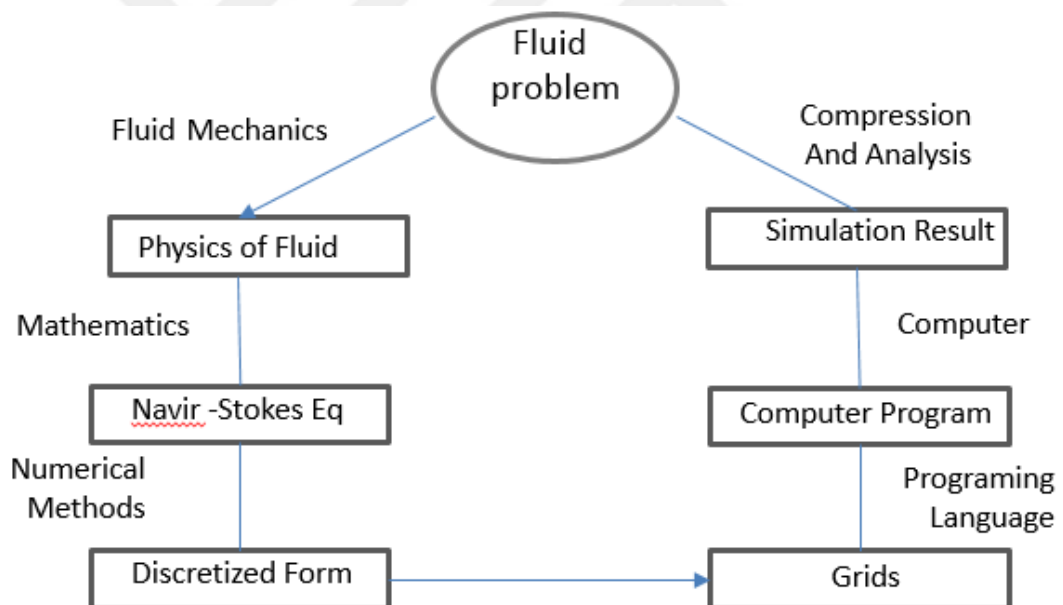


Figure 3.1. Process of Computational Fluid Dynamics

Following a CFD approach leads to many valuable benefits to resolve a fluid dynamic issue:

CFD is cheaper and quicker to execute. A considerable time and cost reduction help solving the problems more conveniently as compared to using traditional approaches. The solution assessment is possible during the early phases of the design process for

sufficiently fitting with the requested tasks. The experimental tests will be conducted on few models after their CFD analysis.

- The full-spectrum analysis is difficult-to-performed on large systems such as modern wind turbines, which, of course, have extreme thermo-flow conditions and narrow geometries. The CFD studies are favorable for such cases.
- A basic and significant quality of CFD is finding a detailed solution using the latest techniques and technologies for complex systems and time-dependent flows.
- The application of numerical models resolves physical problems with high accuracy and greater reliability and helps to make mathematical improvements in solution schemes and turbulence models.
- After the latest advancements, predicting a fluid dynamic problem is no more and issue in most cases because it doesn't require a powerful and dedicated workstation. Only a personal computer is sufficient for that purpose.

3.1. Navier-Stokes Equations

They are governing equations of CFDs, which are based on the law of conservation of fluids' physical properties. This principle describes how fluid properties change. These properties include momentum, mass, and energy that depend on the output and the input. When the law of conservation of mass, momentum and energy is applied, a continuity equation can be derived in addition to the energy equation and the momentum equation, which are as follows:

Continuity Equation:

$$\frac{D\rho}{Dt} + \rho \frac{\partial U_i}{\partial x_i} = 0 \quad (3.1)$$

Momentum Equation:

$$\rho \frac{\partial U_j}{\partial t} + \rho U_i \frac{\partial U_j}{\partial x_i} = -\frac{\partial P}{\partial x_j} - \frac{\partial \tau_{ij}}{\partial x_i} + \rho g_j \quad (3.2)$$

Where

$$\tau_{ij} = -\mu \left(\frac{\partial U_j}{\partial x_i} + \frac{\partial U_i}{\partial x_j} \right) + \frac{2}{3} \delta_{ij} \mu \frac{\partial U_k}{\partial x_k} \quad (3.3)$$

$\rho \frac{\partial U_j}{\partial t}$: Change in local energy with time

$\rho U_i \frac{\partial U_j}{\partial x_i}$: Momentum convection

$-\frac{\partial P}{\partial x_j}$: Surface force
 $\frac{\partial \tau_{ij}}{\partial x_i}$: Diffusion
 ρg_j : Mass force

Energy Equation:

$$\rho c_\mu \frac{\partial T}{\partial t} + \rho c_\mu U_i \frac{\partial T}{\partial x_i} = -P \frac{\partial U_i}{\partial x_i} + \lambda \frac{\partial^2 T}{\partial x_i^2} - \tau_{ij} \frac{\partial U_j}{\partial x_i} \quad (3.4)$$

Here:

$\rho c_\mu \frac{\partial T}{\partial t}$: Local energy change with time

$\rho c_\mu U_i \frac{\partial T}{\partial x_i}$: Convection term

$-P \frac{\partial U_i}{\partial x_i}$: Pressure work

$\lambda \frac{\partial^2 T}{\partial x_i^2}$: Heat flux (diffusion)

$\tau_{ij} \frac{\partial U_j}{\partial x_i}$: irreversible transfer of mechanical energy into heat

When a fluid is compressible, the continuity and the momentum equations can be simplified as given below:

Continuity Equation:

$$\frac{\partial U_i}{\partial x_i} = 0 \quad (3.5)$$

Momentum Equation:

$$\rho \frac{\partial U_j}{\partial t} + \rho U_i \frac{\partial U_j}{\partial x_i} = -\frac{\partial P}{\partial x_j} - \mu \frac{\partial^2 U_j}{\partial x_i^2} + \rho g_j \quad (3.6)$$

For simplifying Navier-Stokes equations, their general form is as follows:

$$\frac{\partial(\rho\Phi)}{\partial t} + \frac{\partial}{\partial x_i} \left(\rho U_i \Phi - \Gamma_\Phi \frac{\partial \Phi}{\partial x_i} \right) = q_\Phi \quad (3.7)$$

As $\Phi = 1, U_j, T$; it is possible to get the momentum and continuity equations, and energy [60], [61], [62], [63]

Basically, the Navier-Stokes equations are analytical in nature, so understanding and solving them is possible using the human mind, but in order to find their computerized or automated solution, their discrete form will be required, which is possible through a method called discretization. The traditional discretization

processes include finite element, finite difference and finite volume. In this case, we will use finite volume method.

The 3D Navier-Stokes equations are in a conservative, integral, or vector form, which are bounded by the surface S and written over a space volume V , and *NUMECA software* support this process as follows:

$$\frac{\partial}{\partial t} \int_V Q \, dV + \oint_S (F \cdot n) \, ds - \oint_S (F_v \cdot n) \, ds = \int_V S_T \, dV \quad (3.8)$$

Here Q stands for the vector of conservative variables:

$$Q = \begin{pmatrix} \rho \\ \rho u_1 \\ \rho u_2 \\ \rho u_3 \\ \rho e_0 \end{pmatrix} \quad (3.9)$$

Here, ρ , u_i and e_0 respectively represent density, Cartesian velocity component, and the total energy.

F stands for the inviscid flux, and F_v shows the viscous flux:

$$F_j = \begin{pmatrix} \rho u_j \\ \rho u_1 u_j + p \delta_{1j} \\ \rho u_2 u_j + p \delta_{2j} \\ \rho u_3 u_j + p \delta_{3j} \\ \rho h_0 u_j \end{pmatrix}, \quad F_{vj} = \begin{pmatrix} 0 \\ \tau_{1j} \\ \tau_{2j} \\ \tau_{3j} \\ u_i \tau_{ij} - q_j \end{pmatrix} \quad (3.10)$$

The index $(i, j) = 1, 2, 3$ that refer to each coordinate component while p and h_0 represent pressure and total enthalpy.

S_T includes the source terms and it can be expressed as:

$$S_T = \begin{pmatrix} \rho \\ \rho f_{e1} \\ \rho f_{e2} \\ \rho f_{e3} \\ w_f \end{pmatrix} \quad (3.11)$$

Here f_{e1} , f_{e2} and f_{e3} are the external force components and w_f is represents work performed by the external forces.

$$W_f = \rho f_e \cdot u \quad (3.12)$$

The total enthalpy h_0 is related to the total energy e_0 :

$$h_0 = e_0 + \frac{p}{\rho} \quad (3.13)$$

The total energy is given by:

$$e_0 = e + \frac{1}{2}u_i u_i \quad (3.14)$$

Thus,

$$h_0 = h + \frac{1}{2}u_i u_i \text{ and } h = e + \frac{p}{\rho} \quad (3.15)$$

Here e represents internal energy while h shows enthalpy. The heat flux q_j is taken from the energy equation and shows thermal conduction. After applying Fourier's law, it will be:

$$q_j = -k \frac{\partial T}{\partial x_j} \quad (3.16)$$

Here, k is the thermal conductivity coefficient while T stands for the temperature.

In case of a Newtonian fluid, the viscous stress tensor τ_{ij} can be obtained through the following equation. For this purpose, Eq. 3.10 has been used:

$$\tau_{ij} = 2\mu S_{ij} + \lambda \frac{\partial u_k}{\partial x_k} \delta_{ij} \quad (3.17)$$

So, μ represents dynamic viscosity, which is second viscosity coefficient. The Kronecker delta S_{ij} and is the strain-rate tensors μ and λ are linked with each other as follows:

$$k = \frac{2}{3}\mu + \lambda \quad (3.18)$$

The Stokes' hypothesis, for incompressible/low Mach number flows ($k = 0$), will change the Eq. 3.18 as follows:

$$\lambda = -\frac{2}{3}\mu \quad (3.19)$$

Now the strain-rate tensor S_{ij} will be:

$$S_{ij} = \frac{1}{2} \left(\frac{\partial u_i}{\partial x_j} + \frac{\partial u_j}{\partial x_i} \right) \quad (3.20)$$

If we substitute Eq. 3.19 and Eq. 3.20 into Eq. 3.10, the viscous stress tensor will be:

$$\tau_{ij} = \mu \left[\left(\frac{\partial u_i}{\partial x_j} + \frac{\partial u_j}{\partial x_i} \right) - \frac{2}{3} \left(\frac{\partial u_k}{\partial x_k} \right) \delta_{ij} \right] \quad (3.21)$$

For closing the Navier-Stokes equations, the relations between different thermodynamic variables (ρ, p, T, e, h) should be found. Assuming and using perfect gas relations, we get the following:

$$e = C_v T, \quad h = C_p T, \quad \gamma = \frac{C_p}{C_v}, \quad C_v = \frac{R}{\gamma - 1}, \quad C_p = \frac{\gamma R}{\gamma - 1} \quad (3.22)$$

The pressure can be computed using the equation of status for perfect gas as follows:

$$p = (\gamma - 1)\rho e = (\gamma - 1)\rho \left(e_0 - \frac{1}{2} u_i u_i \right) \quad (3.23)$$

3.2. Turbulence Models

Fundamentally, the Navier-Stokes equations explain laminar as well as turbulent flows without needing any extra information but the turbulent flows having realistic Reynold's numbers, which show a greater turbulent length range as well as time scales that involve length scales. These length scales are substantially smaller as compared to the smallest finite volume mesh that is practically utilized for the numerical analyses. The Direct Numerical Simulation (**DNS**) of such flows need computation power that should have higher magnitude as compared to what will be available in the predictable future.

For predicting the impact of turbulence, a significant proportion of the **CFD** research concentrated on processes that utilize the *turbulence models*. Those turbulence models are specially developed to create the turbulence impact without recourse to a prohibitively fine mesh or without direct numerical simulation. A majority of the turbulence models are actually statistical in nature. [64]

3.2.1. Closure Problem and the Statistical Turbulence Models

Generally, the turbulence models substantially modify the unsteady Navier-Stokes equations because they introduce fluctuating as well as averaged quantities for

producing the Reynolds Averaged Navier-Stokes (**RANS**) equations, which only represent the mean flow quantities, and at the same time, they model turbulence impact without resolving the turbulent fluctuations. All the turbulence field scales have been modeled. The turbulence models, which are (**RANS**)-based, are also termed as statistical turbulence models because they require statistical averaging procedure for obtaining equations. (**RANS**) equations' simulation substantially decreases the computational efforts by directly comparing the results with the numerical simulation, and this process has been used for real-time engineering computations. [64]

The averaging procedure brings in additional unknown constants and variables, which have fluctuating quantities, and they perform as additional stresses in a fluid. They are termed as ‘turbulent’ or ‘Reynolds’ stresses, which are very difficult to measure in a direct way, and they are unknowns. These Reynold's stresses should be modeled using extra equations with known quantities for reaching the “closure,” which means existence of sufficient number of equations to calculate the unknowns, such as the Reynolds-Stress tensor. The equations generally define the turbulence model types, which are mentioned below:

3.3. Reynolds Averaged Navier-Stokes (RANS) Equations

Normally, the RANS equations can be derived through decomposition of the flow variables. They can be expressed in integral form as given below:

$$\frac{\partial}{\partial t} \int_V Q \, dV + \oint_S (F \cdot n) \, ds - \oint_S (F_v \cdot n) \, ds = \int_S S_T \, dV \quad (3.24)$$

Where,

$$Q = \left\{ \begin{array}{c} \bar{\rho} \\ \bar{\rho} \bar{u}_1 \\ \bar{\rho} \bar{u}_2 \\ \bar{\rho} \bar{u}_3 \\ \bar{\rho} \bar{e}_0 + (\bar{\rho} \bar{e} + k) \end{array} \right\}, \quad F_j = \left\{ \begin{array}{c} \bar{\rho} \bar{u}_j + \bar{\rho} \bar{u}_j \\ \bar{\rho} \bar{u}_1 \bar{u}_j + \bar{p} \bar{\delta}_{1j} + \bar{u}_1 \bar{\rho} \bar{u}_j + \bar{\rho} \bar{u}_1 \bar{u}_j \\ \bar{\rho} \bar{u}_2 \bar{u}_j + \bar{p} \bar{\delta}_{2j} + \bar{u}_2 \bar{\rho} \bar{u}_j + \bar{\rho} \bar{u}_2 \bar{u}_j \\ \bar{\rho} \bar{u}_3 \bar{u}_j + \bar{p} \bar{\delta}_{3j} + \bar{u}_3 \bar{\rho} \bar{u}_j + \bar{\rho} \bar{u}_3 \bar{u}_j \\ \bar{\rho} \bar{h}_0 \bar{u}_j + \bar{e}_0 \bar{\rho} \bar{u}_j + (\bar{\rho} \bar{e} + k) \bar{u}_j \end{array} \right\} \quad (3.25)$$

And

$$F_{vj} = \left\{ \begin{array}{c} 0 \\ \bar{\tau}_{1j} - \tau_{1j}^T \\ \bar{\tau}_{2j} - \tau_{2j}^T \\ \bar{\tau}_{3j} - \tau_{3j}^T \\ \bar{u}_i \bar{\tau}_{ij} - \bar{q}_j + \theta_j^T \end{array} \right\} \quad (3.26)$$

Here, the turbulent fluctuations possess kinetic energy and the Reynolds stress tensor τ_{ij}^T which are given below:

$$k = \frac{1}{2} \overline{\rho \dot{u}_i \dot{u}_i} \quad (2.27)$$

$$\tau_{ij}^T = \frac{1}{2} \overline{\rho \dot{u}_i \dot{u}_j} \quad (2.28)$$

θ_j^T has a turbulent heat flux tensor q_j^T as well as some other turbulent terms emerging out of the density-velocity correlations and the triple velocity correlations. They are mathematically expressed below:

$$\theta_j^T = w_j^T - q_j^T - k_j^T - E_j^T \quad (2.29)$$

$$w_j^T = -\bar{u}_i \tau_{ij}^T + \bar{u}_i \tau_{ij} \quad (2.30)$$

$$q_j^T = \overline{\rho \dot{h} \dot{u}_j} \quad (3.31)$$

$$E_j^T = \bar{u}_i \overline{\rho \dot{u}_i \dot{u}_j} \quad (2.32)$$

For solving the equations mentioned above, all the turbulent terms should be modeled. It is difficult, so instead, the compressible density weighted averaged *RANS* equations should be used. This density weighted-average is expressed below:

$$\tilde{\phi} = \frac{\overline{\rho \phi}}{\bar{\rho}} \quad (2.33)$$

With the decomposition:

$$\phi = \tilde{\phi} + \ddot{\phi} \quad (2.34)$$

and the relations:

$$\overline{\tilde{\phi}} = \tilde{\phi} \quad \text{and} \quad \overline{\rho \ddot{\phi}} = 0 \quad (3.35)$$

So, we obtain Favre-averaged *RANS* equations as given below:

$$\frac{\partial}{\partial t} \int_v Q \, dV + \oint_s (F \cdot n) \, ds - \oint_s (F_v \cdot n) \, ds = \int_v S_T \, dV \quad (3.36)$$

$$Q = \left\{ \begin{array}{c} \bar{\rho} \\ \bar{\rho} \tilde{u}_1 \\ \bar{\rho} \tilde{u}_2 \\ \bar{\rho} \tilde{u}_3 \\ \bar{\rho} \tilde{e}_0 + k \end{array} \right\}, \quad F_j = \left\{ \begin{array}{c} \bar{\rho} u_j \\ \bar{\rho} \tilde{u}_1 \tilde{u}_j + \bar{p} \delta_{1j} \\ \bar{\rho} \tilde{u}_2 \tilde{u}_j + \bar{p} \delta_{2j} \\ \bar{\rho} \tilde{u}_3 \tilde{u}_j + \bar{p} \delta_{3j} \\ \bar{\rho} \tilde{h}_0 \tilde{u}_j + k \tilde{u}_j \end{array} \right\} \quad (3.37)$$

$$F_{vj} = \left\{ \begin{array}{c} 0 \\ \tilde{\tau}_{1j} - \tau_{1j}^T \\ \tilde{\tau}_{2j} - \tau_{2j}^T \\ \tilde{\tau}_{3j} - \tau_{3j}^T \\ \tilde{u}_i \tilde{\tau}_{ij} - \tilde{q}_j + \theta_j^T \end{array} \right\} \quad (3.38)$$

With

$$k = \frac{1}{2} \overline{\rho \ddot{u}_i \ddot{u}_i} \quad (3.39)$$

$$\tau_{ij}^T = \frac{1}{2} \overline{\rho \ddot{u}_i \ddot{u}_j} \quad (3.40)$$

$$\tau_{ij} = (\mu + \mu_t) \left[\left(\frac{\partial \tilde{u}_i}{\partial x_j} + \frac{\partial \tilde{u}_j}{\partial x_i} \right) - \frac{1}{2} \left(\frac{\partial \tilde{u}_k}{\partial x_k} \right) \delta_{ij} \right] \quad (3.41)$$

$$q_j = -(k + k_t) \frac{\partial \tilde{T}}{\partial x_j} \quad (3.42)$$

$$\theta_j^T = w_j^T - q_j^T - k_j^T \quad (3.43)$$

$$w_j^T = -\bar{u}_i \tau_{ij}^T + \overline{\ddot{u}_i \tilde{\tau}_{ij}} \quad (3.44)$$

$$q_j^T = \overline{\rho \dot{h} \ddot{u}_j} \quad (3.45)$$

$$k_j^T = \frac{1}{2} \overline{\rho \ddot{u}_i \ddot{u}_i \ddot{u}_i} \quad (3.46)$$

Generally, the governing equations for rotating systems can be formulated in relative systems. They are solved for relative velocities, but some applications require far field boundary conditions including the wind turbines and propellers; their equations can be formed in a relative system but solved using absolute velocities. This certainly makes the far field velocities more physical. Ideally, they should not bear the impact of rotating blades; therefore, the flow at the external boundaries remains uniform. In addition, there is a rotating flow around the blade of a wind turbine, which makes the far field unaffected by the blade rotation. The flow is generally rotating near the blade while velocities are relative. The information about the (*RANS*) and the Navier-Stokes has been provided in the references [65,66]. For absolute velocities, the (*RANS*) equations are given as under:

$$\frac{\partial}{\partial t} \int_v Q \, dV + \oint_s (F \cdot n) \, ds - \oint_s (F_v \cdot n) \, ds - = \int_v S_T \, dV \quad (3.47)$$

$$Q = \begin{Bmatrix} \rho \\ \bar{\rho} \tilde{u}_1 \\ \bar{\rho} \tilde{u}_2 \\ \bar{\rho} \tilde{u}_3 \\ \bar{\rho} \tilde{e}_0 + k \end{Bmatrix}, \quad F_j = \begin{Bmatrix} \bar{\rho} \tilde{w} \\ \bar{\rho} \tilde{w}_1 \tilde{w}_j + \bar{p} \delta_{1j} \\ \bar{\rho} \tilde{w}_2 \tilde{w}_j + \bar{p} \delta_{2j} \\ \bar{\rho} \tilde{w}_3 \tilde{w}_j + \bar{p} \delta_{3j} \\ \bar{\rho} \tilde{h}_0 \tilde{w}_j + k \tilde{w}_j \end{Bmatrix} \quad (3.48)$$

$$F_j = \begin{Bmatrix} 0 \\ \tilde{\tau}_{1j} - \tau_{1j}^T \\ \tilde{\tau}_{2j} - \tau_{2j}^T \\ \tilde{\tau}_{3j} - \tau_{3j}^T \\ \tilde{u}_i \tilde{\tau}_{ij} - \tilde{q}_j + \theta_j^T \end{Bmatrix} \quad (3.49)$$

Here w_i represents x_i component at relative velocity u_i . The x_i is the absolute velocity component; therefore, this formulation includes both relative as well as absolute velocity components.

In this case, the source term will be:

$$S_T = \begin{Bmatrix} 0 \\ -\bar{\rho}(\omega \times u) \\ 0 \end{Bmatrix} \quad (3.50)$$

Since ω is the relative angular velocity.

It is mentioned earlier that modeling turbulent terms in the (*RANS*) equations helps solving them. The current study has two different turbulence models for investigations, which include the Spalart-Allmaras [67, 68], and Shear Stress Transport (*SST*)($\mathbf{k} - \omega$) models [69]. They are (*RANS*)-based as well as linear turbulent viscosity models. Here, $\mathbf{v}^2 - \mathbf{f}$ represents the non-linear turbulent viscosity model.

3.4. Spalart-Allmaras Model

This model is a single-equation model, and it is very useful because it is robust and it can handle complex flows. It has some advantages over the ($\mathbf{k} - \epsilon$) model, which include its less CPU/memory usage and its robustness. This model is focused on solving additional transport equation in terms of turbulent viscosity. Its equation has many diffusive, advective, and source terms. In this case, the transport equation will be:

$$\frac{d\tilde{v}}{dt} = \frac{1}{\sigma} \{ \nabla \cdot [(v + \tilde{v})\nabla\tilde{v}] + c_{b2}(\nabla\tilde{v})^2 \} + c_{b1}\tilde{S}\tilde{v}(1 - f_{t2}) - \left\{ c_{w1}f_w - \frac{c_{b1}}{k^2} \right\} \left\{ \frac{\tilde{v}}{d} \right\}^2 + f_{t1}(\Delta q)^2 \quad (3.51)$$

The eddy viscosity:

$$v_t = \tilde{v}f_{v1} \quad (3.52)$$

and,

$$f_{v1} = \frac{x^3}{x^3 + c^3_{v1}} \quad x = \frac{\tilde{v}}{v} \quad (3.53)$$

\tilde{v} represents the working variable while v shows molecular viscosity.

The relation between constants and variables appearing in equations (3.46), (3.47) and (3.48) are given below:

$$\tilde{S} = S + \frac{\tilde{v}}{k^2 d^2} f_{v2} \quad f_{v2} = 1 - \frac{x}{1 + x f_{v1}} \quad (3.54)$$

In this case, \mathbf{d} shows the distance to the wall, \mathbf{k} represents the Von Karman constant while \mathbf{S} represents the vorticity magnitude.

Function f_w :

$$f_w = g \left(\frac{1+c_{w3}^6}{g^6+c_{w3}^6} \right)^{\frac{1}{6}} \quad (3.55)$$

When,

$$g = r + c_{w2}(r^6 - r) \quad r = \frac{\tilde{v}}{\xi k^2 d^2} \quad (3.56)$$

Functions f_{t1} and f_{t2} :

$$f_{t1} = c_{t1} g_t \exp \left[-c_{t2} \left(\frac{w_t}{\Delta q} \right)^2 (d^2 + g_t^2 d_t^2) \right], \quad f_{t2} = c_{t3} \exp(-c_{t4} x^4) \quad (3.57)$$

Where:

d_t : Distance between the field point and the travel point that exists on the surface

w_t : Wall vorticity

Δq : Velocity variation between the trip and the field point and at the trip

$g_t: g_t = \min \left[1.0, \Delta q / w_t \Delta x \right]$, at the grid-spacing along the wall.

The constants include:

$$\begin{aligned} \sigma &= \frac{2}{3} & c_{b1} &= 0.1355 & c_{b2} &= 0.1355 & k &= 0.41 \\ c_{w1} &= \frac{c_{b1}}{k^2} + \left(\frac{1+c_{b1}}{\sigma} \right) = 2.5093 & c_{w2} &= 0.3 & c_{w3} &= 2.0 \\ c_{v1} &= 7.1 & c_{t1} &= 1.0 & c_{t2} &= 2.0 & c_{t3} &= 1.1 & c_{t4} &= 2.0 \end{aligned}$$

3.5. Shear Stress Transport/ $k - \omega$ (SST)

This model is also a two-equation model, the first equation is for kinetic turbulent energy k and the second equation expresses turbulent dissipation rate. Just like $(k - \epsilon)$, this model was presented in several versions. The Wilcox $(k - \omega)$ model is a popular version of this model [70,71] that has better numerical stability in comparison with the $(k - \epsilon)$ model specifically pertaining to the viscous sub-layer near the wall but this version has a major disadvantage and that is extreme sensitivity of the results to the value of ω in adverse pressure gradient boundary layer flows and free shear layer; so, the $(k - \omega)$ cannot be termed as ideal for the wake zone application in the boundary layer but the $(k - \epsilon)$ model performs better in the wake regions and the outer portion of the boundary layer. In this case, blending both the

models helps combining their best features. The two (*SST*) model transport equations are:

$$\rho \frac{Dk}{dt} = \frac{\partial}{\partial x_j} \left[(\mu + \sigma_k \mu_t) \frac{\partial k}{\partial x_j} \right] + p_k - \beta^* \rho \omega k \quad (3.58)$$

$$\rho \frac{D\omega}{dt} = \frac{\partial}{\partial x_j} \left[(\mu + \sigma_\omega \mu_t) \frac{\partial \omega}{\partial x_j} \right] + \gamma p_k \frac{\omega}{k} - \beta^* \rho \omega^2 + 2(1 - F_1) \rho \sigma_{\omega 2} \frac{1}{\omega} \frac{\partial k}{\partial x_j} \frac{\partial \omega}{\partial x_j} \quad (3.59)$$

Here the constant $\beta^* = 0.09$ while the last right-side term of Eq. 3.59 is cross diffusion term, which is activated just outside the boundary layer.

F_1 is a blending function to blend the model coefficients with transformed ($k - \epsilon$) model in free stream zones and free shear layer.

The constants given in equations 3.58 and 3.59 in short form are given as:

$$\emptyset = F_1 \emptyset_1 - (1 - F_1) \emptyset_2 \quad (3.60)$$

In this case, \emptyset_1 stands for ($k - \omega$) model constants (at $F_1 = 1$) while \emptyset_2 shows constants linked with the ($k - \epsilon$) model (at $F_2 = 0$).

The γ, β, σ_k and σ_ω are calculated as given below:

- Inner model constants: $\gamma_1 = 0.5532$, $\beta_1 = 0.075$, $\sigma_{k1} = 0.5$, $\sigma_{\omega 1} = 0.5$
- Outer model constants: $\gamma_2 = 0.4403$, $\beta_2 = 0.0828$, $\sigma_{k2} = 1.0$, $\sigma_{\omega 2} = 0.856$

Blending function F_1 :

$$F_1 = \tanh \left\{ \min \left[\max \left(\left(\frac{\sqrt{k}}{\beta^* \omega d}, \frac{500\nu}{\omega d^2} \right), \frac{4\rho\sigma_{\omega 2}k}{CD_{k\omega}d^2} \right) \right] \right\} \quad (3.61)$$

and,

$$CD_{k\omega} = \max \left(2\rho\sigma_{\omega 2} \frac{2}{\omega} \frac{\partial k}{\partial x_j} \frac{\partial \omega}{\partial x_j}, 1.0e^{-20} \right) \quad (3.62)$$

Where d is the distance to the nearest surface.

For this research, the Mach number is quite small (< 0.07) for wind turbine applications. In this case, the *CFD* simulation might have certain convergence problems, and to address that problem, we used pre-conditioning.

3.6. Pre-Conditioning for Low Mach Number Flows

When the Mach number values are low, the time marching algorithms are show less efficient compressible flows. This happens because of two issues such as difference between the values of convective eigenvalues (\mathbf{u}) and the acoustic eigenvalues ($\mathbf{u} + \mathbf{c}$) and ($\mathbf{u} - \mathbf{c}$) that leads to a restrictive time step and causes poor convergence characteristics. Another issue is rounded off errors that happens because of the momentum equations have absolute pressure. It develops a low-speed pre-conditioner to gain convergence speed and solution accuracy in case the Mach number is too low. In case of steady state applications, which are solved with the help of time-marching algorithms, the dependent variables have time derivatives, which are multiplied with a matrix termed as pre-conditioning matrix. It removes the eigenvalue stiffness and introduces reduced flow variables including dynamic enthalpy and dynamic pressure. In the nutshell, they reduce the rounded off errors for low Mach numbers. They replace the acoustic wave speed c using a pseudo wave speed \mathbf{c}' that has the same magnitude order for a specific a fluid speed.

We will introduce one of the pre-conditioning models called the Hakimi pre-conditioning [72], [73] that gives reliability to a solution.

3.6.1 Hakimi Preconditioning

The Hakimi pre-conditioning has proved to give efficient convergence rates and accurate solutions for Mach numbers between 10^{-6} to 0.1 and Reynolds numbers from 10^{-6} to 10^6 and aspect ratios from 1 to 2000 [73].

The pre-conditioned (RANS) equations will be:

$$\int_v \Gamma^{-1} \frac{\partial \mathbf{u}}{\partial t} dV + \oint_s (\mathbf{F} \cdot \mathbf{n}) ds - \oint_s (\mathbf{F}_v \cdot \mathbf{n}) ds = \int_v S_T dV \quad (3.63)$$

and,

$$U = \begin{Bmatrix} p_g \\ u_1 \\ u_2 \\ u_3 \\ E_g \\ \rho k \\ \rho \varepsilon \end{Bmatrix} \quad (3.64)$$

Now the gauge pressure can be expressed as:

$$p_g = p - p_{ref} \quad (3.65)$$

The total gauge energy E_g can be defined for perfect gas as follows:

$$E_g = C_v(T - T_{ref}) + \frac{u^2}{2} \quad (3.66)$$

Now the Hakimi pre-conditioning matrix will be used to describe turbulence transport equations in case of a compressible flow, which is given by:

$$\left(\begin{array}{cccccccc} \frac{1}{\beta^2} & 0 & 0 & 0 & 0 & 0 & 0 & \dots\dots\dots 0 \\ \frac{(1+\alpha)u_1}{\beta^2} & \rho & 0 & 0 & 0 & 0 & 0 & \dots\dots\dots 0 \\ \frac{(1+\alpha)u_2}{\beta^2} & 0 & \rho & 0 & 0 & 0 & 0 & \dots\dots\dots 0 \\ \frac{(1+\alpha)u_3}{\beta^2} & 0 & 0 & \rho & 0 & 0 & 0 & \dots\dots\dots 0 \\ -\frac{\alpha u^2 + E_g}{\beta^2} & 0 & 0 & 0 & 0 & \rho & 0 & \dots\dots\dots 0 \\ 0 & 0 & 0 & 0 & 0 & 0 & \rho & \dots\dots\dots 0 \\ 0 & 0 & 0 & 0 & 0 & 0 & \rho & \dots\dots\dots 0 \end{array} \right) \quad (3.67)$$

Pre-conditioning parameters:

$$\alpha = -1, \quad \beta = \sqrt{\beta^* U_{ref}} \quad (3.68)$$

When U_{ref} represents reference velocity while β^* stands for the coefficient.

3.7. Boundary Conditions

There are two types of boundary conditions for the *CFD* simulations in case of wind turbine rotor blade: The solid wall boundary conditions and the external boundary conditions.

3.7.1 Solid Wall Boundary Conditions

They are mentioned below:

- a) Spalart-Allmaras Model:

The Spalart-Allmaras turbulence model applies when the turbulent working variable tends to zero for a solid wall:

$$\tilde{\nu} = 0 \quad (3.69)$$

b) $k - \epsilon$ Model:

This model applies when the k and ϵ values are imposed on a solid wall.

c) $k - \omega$ Model:

It applies where the following boundary conditions matter (on the solid wall):

$$\omega_{wall} = \frac{60\nu}{\beta_1 d^2} \quad (3.70)$$

$$k_{wall} = 0 \quad (3.71)$$

d) $v^2 - f$ Model:

This model is chosen when the following boundary conditions are met for a solid wall:

$$k_{wall} = 0 \quad (3.72)$$

$$\epsilon_{wall} = 2\nu \frac{k}{y^2} \quad (3.73)$$

$$v_{wall}^2 = 0 \quad (3.74)$$

$$f_{wall} = 0 \quad (3.75)$$

3.7.2. External Boundary Conditions

These conditions make use of the Riemann invariants. Their details have been provided in the references section [74]. The far-field boundary conditions are generally uniform because their velocities remain unaffected by the blade rotation. Those blocks, which are closer to the blade, affect the flow. The rotating-non-rotating block interaction is managed with the help of a code.

The static pressure values, axial velocity and the temperature define the external boundary conditions, which are obtained from the experimental data while the turbulent viscosity, the turbulent dissipation and the turbulent kinetic energy can be computed as given below: The Sutherland's law is used for calculating the dynamic viscosity [75]:

$$\mu = \mu_{ref} \left(\frac{T}{T_{ref}} \right)^{3/2} \frac{T_{ref} + S}{T + S} \quad (3.76)$$

So,

- T_{ref} : Reference temperature.
- μ_{ref} : Viscosity at.
- S : Sutherland temperature.

When air can act as a perfect gas, the Sutherland's law coefficients will be as follows:

Table 3.1: Sutherland's Law Coefficient

	Air as perfect gas
$\mu_{ref}(kg/ms)$	$1.716x^{-5}$
$T_{ref}(K)$	273.15
$S(K)$	110

he kinematic viscosity has been calculated using Eq. 3.73:

$$v = \mu/\rho \quad (3.77)$$

Consequently, the external flows for turbulent viscosity can be computed [76]:

$$v_{T \text{ external}} = v_{\text{external}} \quad (3.78)$$

The turbulent kinetic energy k is computed using turbulent T_u intensity by the following formula:

$$T_u = \frac{\sqrt{\overline{u^2}}}{u_{ref}} \quad (3.79)$$

$$k = \frac{3}{2} (\sqrt{\overline{u^2}})^2 \quad (3.80)$$

The turbulent dissipation ε is computed as given below:

$$\varepsilon = c_\mu \frac{\mu}{\mu_t} \frac{\rho_{ref} k^2}{\mu} \quad (3.81)$$

With $c_\mu = 0.09$

Chapter 4

CFD Simulations for Test Cases: NREL Phase VI (HAWT Rotors)

This section consists of the investigation results of *3D* steady state computational Fluid dynamics (*CFD*), which was conducted on the turbine used in the experiments according to the guidelines of the National Energy Laboratory. A horizontal wind turbine (*HAW*) has been selected for the process of investigation and validation, which were conducted using the Numeca Fine/Turbo solver. Two different models were used during the investigation. The Spalart- Allmaras (extended wall function) and the Shear Stress Transport (*SST*) have been selected to process the experimental values of this study.

4.1. Experimental Data and Real Blade Description of the Test Case

The mentioned *NREL-VI* turbine was chosen in this study to simulate *CFD*. It consists of a rotor with diameter 10.058m and two blades. It was adopted in the design of the rotor, which is based on airfoil S809. These turbines were tested in a wind tunnel (Size: 24.4x36.6m) like *NASA Ames* wind tunnel (Hand et al., 2001). The following figure shows the mentioned turbine in the test tunnel.



Figure 4.1. NREL-VI Wind Turbine Inside the NASA Ames Wind Tunnel. [77]

As mentioned above, it is an upwind/horizontal axis turbine consisting of two blades with a twist. The following figures and a table show the description of the blade used for the turbine.

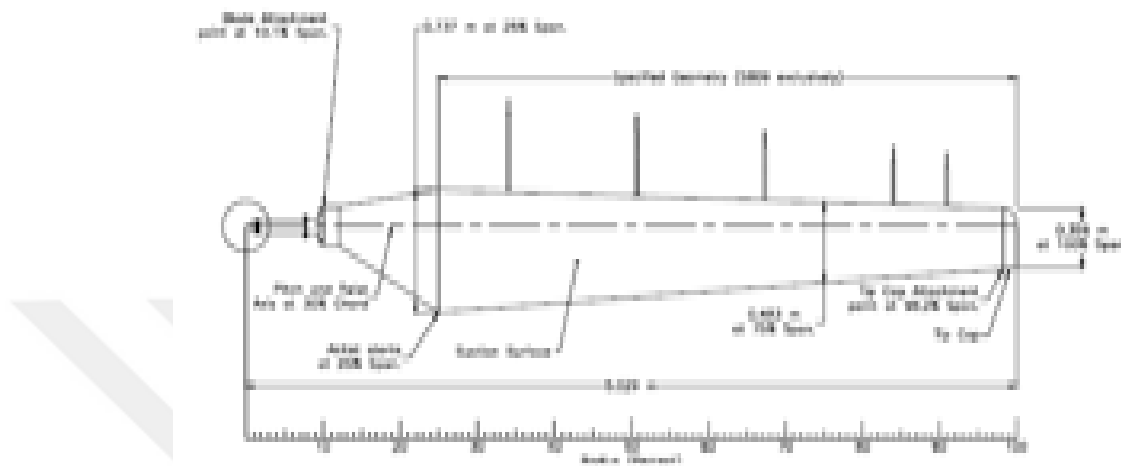


Figure 4.2. Baseline Plan Form View

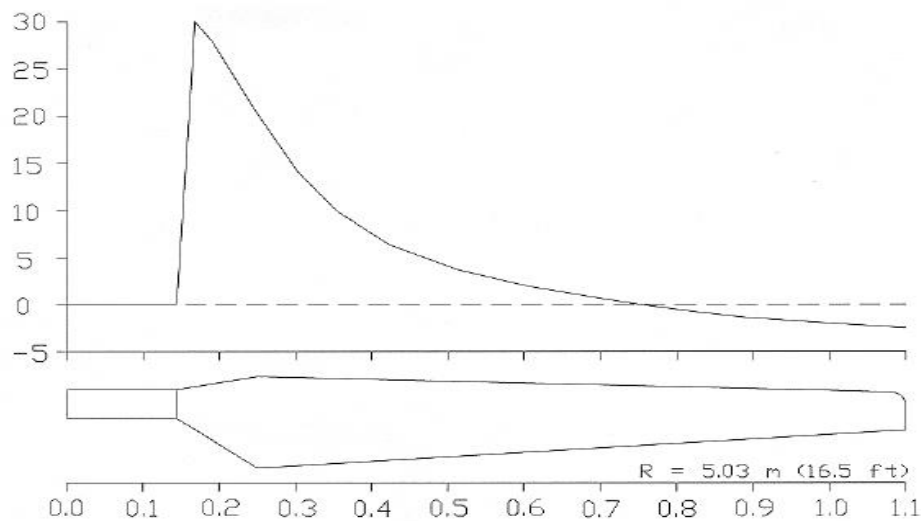


Figure 4.3. Baseline Twist Distribution Along the Blade

Table 4.1. NREL Phase VI Blade Description

Number of blades	2 blades
Rotor Diameter	10.58m
Hub Height	12.192m
Rotational Speed	71.63rpm
Cone angle	0 degree
Power Regulation	Stalled
Blade tip pitch angle	3 degrees
Rotor location	Upwind
Rotational Direction	CCW
Twist angle	Non-linear twist
Airfoils	S809 with multiple angles and scales
Blade chord length	0.358m–0.728m (linear taper)
Blade thickness	t/c = 21% during the span

4.2 Geometric Blade

4.2.1 Airfoil Features

In general, the main component of the wind turbine design for power generation is the blade; however, its properties depend on the airfoil shape and features. The airfoil shape design is the most important factor affecting the movement of airflow on the surface of the blade, and thus, on the ratio of lifting (force-to-drag ratio) as well.

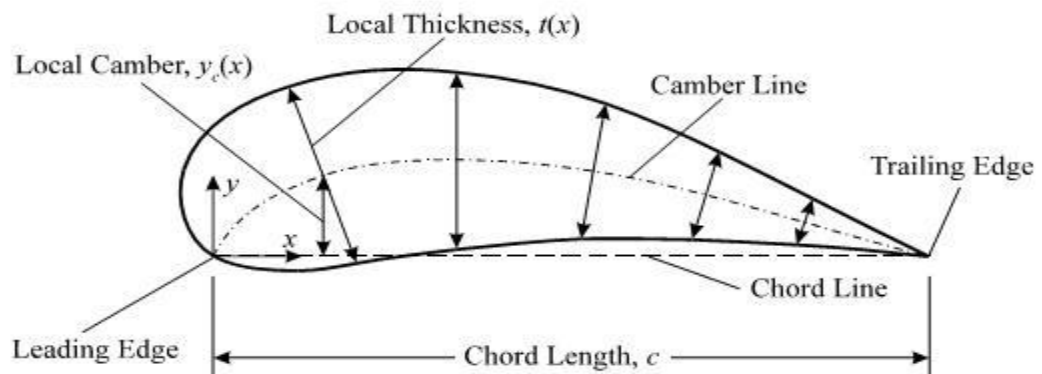


Figure 4.4: Geometric Blade

4.2.2. S809 Wind Turbine Airfoil

In 1986, S809 design was created for use in wind turbines and other aviation fields. It has been tested in *NASA* laboratories. The experimental design and analysis of the airfoil was also tested at Delft University of Technology at low speeds, which are suitable for wind turbines. The requirements such as low profile drag, maximum lift, and insensitivity to roughness were some features, which were assured, and they exhibited docile stall. The properties of airfoil thickness include 21%, highest possible lift coefficient 1.10, and design lift coeff. 0.5 in addition to Reynold's value 2×10^6

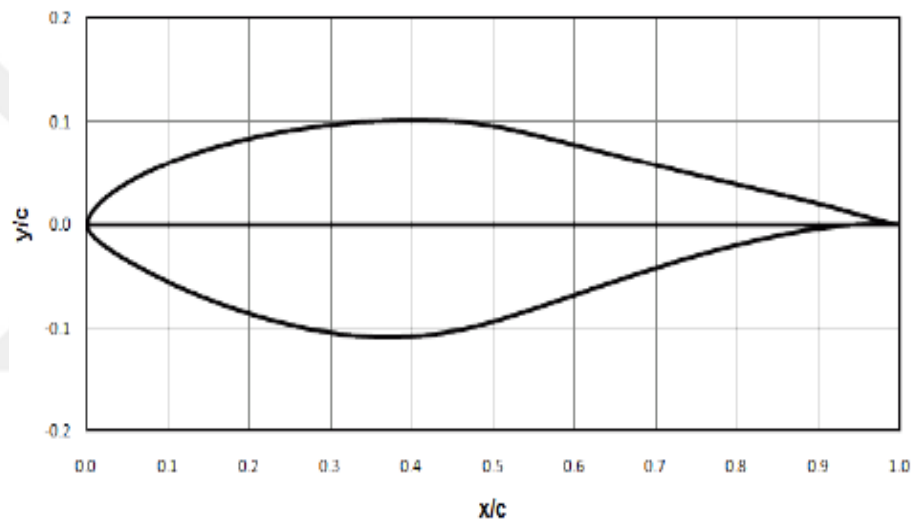


Figure 4.5. S809 Airfoil

Moreover, in the studied case, the geometric blade sections were reduced to 19, which are mentioned in Table 4.2:

- $r = 0$ m: The hub center
- $r = 0.508$ m: The initial part of the blade root. There is a circular blade section.
- $r = 0.883$ m: Shows the blade root ending while, there is a circular blade section.
- from $r = 0.883$ m to $r = 1.275$ m: Cylindrical to S809 Airfoil transition
- from $r = 1.275$ m and $r = 5.029$ m: The S809 airfoil blade sections. There were 26 blade sections.

Table 4.2. Twist and Chord Variations (NREL-VI Rotor Blade)

Section	Radial Distance r (m)	Span Station (r/5.029 m)	Chord length (m)	Twist (degrees)
1	0.508	0.101	0.218	0
2	0.660	0.131	0.218	0
3	1.343	0.267	0.728	18.074
4	1.510	0.300	0.711	14.292
5	1.648	0.328	0.697	11.909
6	1.952	0.388	0.666	7.979
7	2.257	0.449	0.636	5.308
8	2.343	0.466	0.627	4.715
9	2.562	0.509	0.605	3.425
10	2.867	0.570	0.574	2.083
11	3.171	0.631	0.543	1.150
12	3.476	0.691	0.512	0.494
13	3.781	0.752	0.482	-0.015
14	4.023	0.800	0.457	-0.381
15	4.086	0.812	0.451	-0.475
16	4.391	0.873	0.420	-0.920
17	4.780	0.934	0.389	-1.352
18	5.029	0.950	0.381	-1.469
19	5.029	1.000	0.358	-1.775

The cylindrical shape transitioned to the shell 809 shape, which was linearly related to the function of the feather using AutoBlade program (Developer: Numeca software) [78]. The sections that are very close to each other will also be removed. This will help in the solution process and reduce the effort and time required for the treatment unit (CPU).

As pitch angle of the blade is 3 degrees (Sequence: *H*), so, the twist angle of every section was increased by additional 3 degrees. The 2D blade section shape and the 3D blade shape are illustrated in figures 4.6 and 4.7:

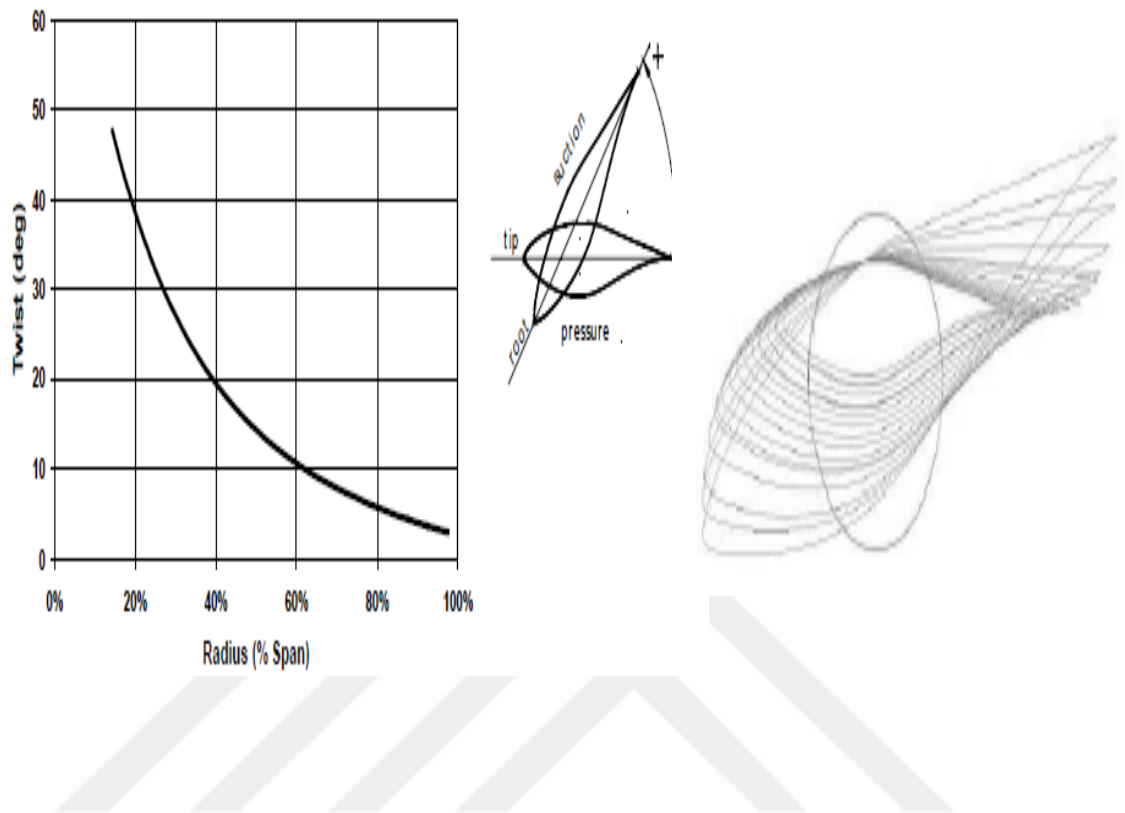


Figure 4.6. Angle and Twist at Different Blade Sections (NREL-VI)

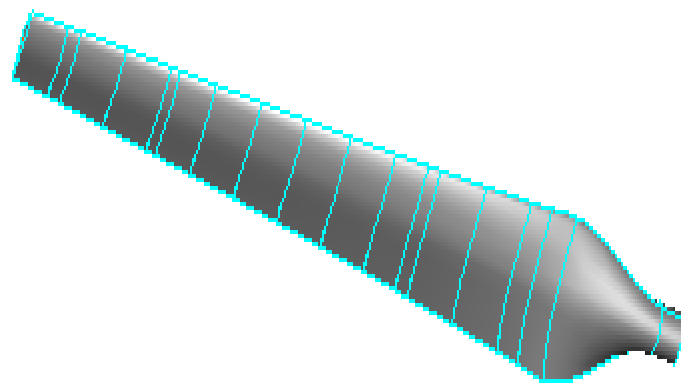


Figure 4.7. *3D NREL-VI* Blade Geometry (Created Using AutoBlade Software)

4.3. Mesh Generation

Grid generation is one of the most important steps taken before processing and also for solutions. It is important to build accurate and robust grid to get the best results. The solutions used in the *CFD* are based on two types of grids: regular (structured) and irregular (unstructured). A structured grid is a collection of regular repeating elements. Such grids are generally represented by quadrilateral elements in *2D* and hexahedral *3D* elements. Since the elements are arranged in a regular repeating pattern, the connectivity information of the elements is stored implicitly. Each cell in the grid is directly addressed by the index (i, j) in *2D* or (i, j, k) in *3D*.

It substantially reduces the amount of computational effort that calculations take. For enhancing the overall *CFD* solution accuracy, the mentioned grids can be processed until they get finer if they are stretched in a specific direction to have several closely-spaced grid points to solve large gradients [79]. Further details about the grid types are given in the references [79,80]

The structured mesh was generated around a blade and the turbine's surrounding air, and the process was repeated for the other blade as well. Keeping the purpose of generating structured hexahedral grid in view, 16 components were obtained after dividing the solution domain. It has been illustrated in Fig.4.8. It was found that the length of the computational domain was six times the blade length (in radial direction) while it was 15 times the length of blade in the axial direction. Numeca AutoGrid was used to generate the mesh.

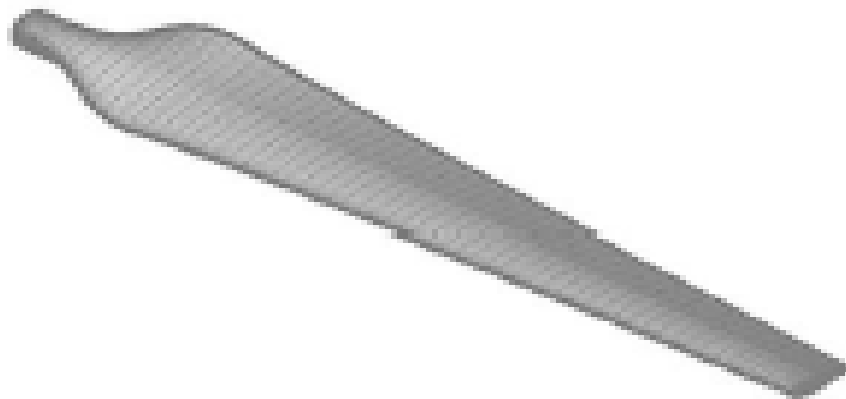


Figure 4.8. 3D Blade

Structured mesh with O4H grid topology is generated around the blades using AutoGrid5 software of NUMECA International.

4.3.1 Mesh Study

The mesh was generated for a single blade and the periodic boundary conditions were imposed to account for the other blade. The number of points on the entire mesh including the blade and external flow is around 7.0 million points. The thickness of the first cell to the wall was set as 3×10^{-6} m to obtain a y^+ value close to 1. Mesh contour is shown in Fig.4.9. The study was conducted in this case at different wind speed from coarse to fine and finer meshes with resolution of 20000,900000,7000000 nodes respectively. For the tested turbulence models. The mesh quality is shown in Table 4.3.

Table 4.3. Different Grid System for *NREL-VI* at $5m/s$

Mesh	Number of points	Torque (Nm.)	Time
Coarse	120000	230	16minut
Fine	900000	308	2.5hr
Finer	7000000	311	12hr

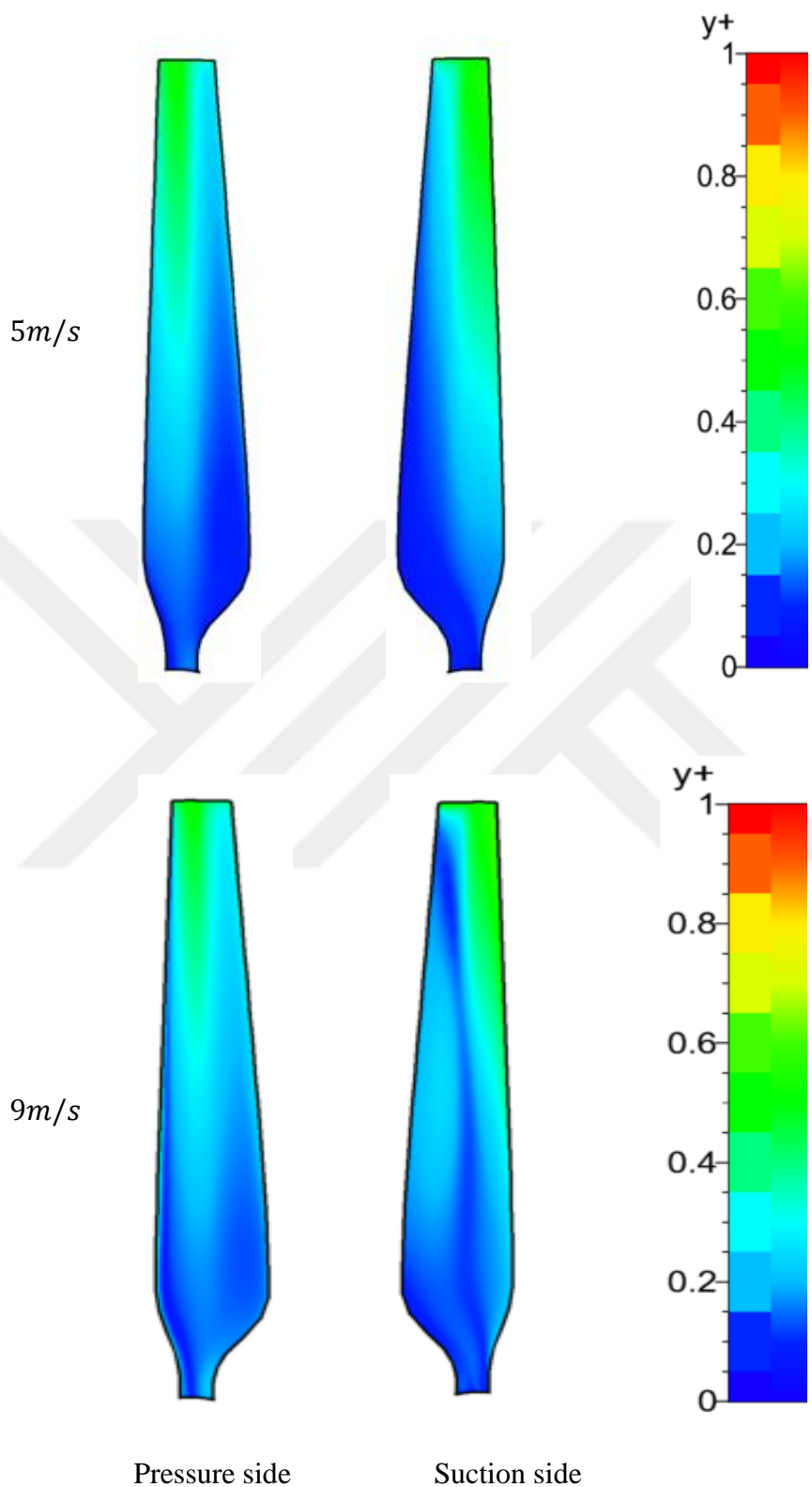


Figure 4.9. Y+ Contours for 5 m/s and 9 m/s

Mesh in blade-to-blade view, and 3D mesh generation around the blade is shown in figures 4.10.

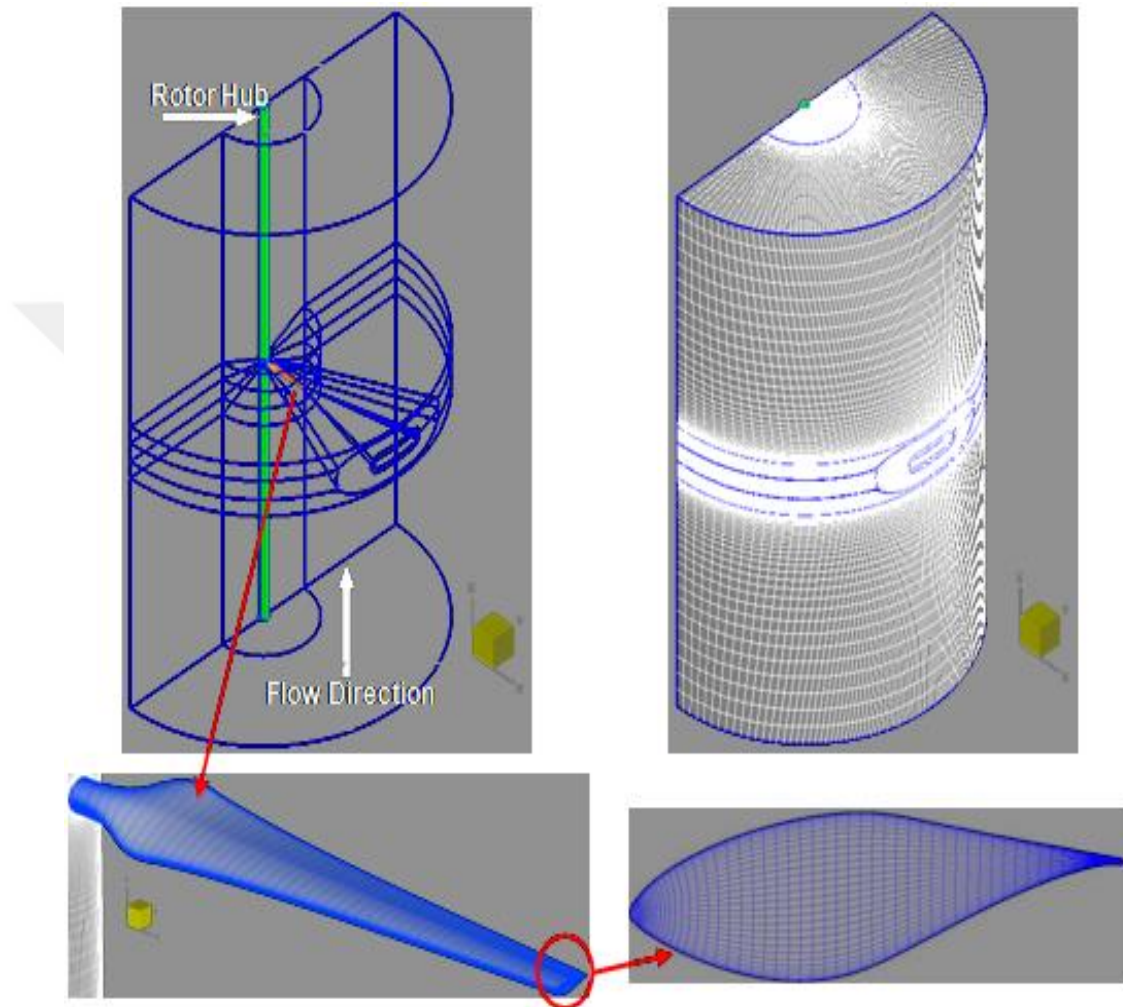


Figure 4.10. 3-D Mesh Structure of the Baseline Blade.

4.4. CFD Simulation and Results

Simulating and solving flow equations is possible through utilizing the validated **3D** Navier–Stokes flow solver, which is based on finite volume discretization. The solver requires a physical model called as the Reynold's Averaged Navier–Stokes equations that applies in rotating frameworks of reference, which is coupled with many turbulence models. The solutions were found until satisfying the convergence

criterion while the global residual was reduced to lower than $10e-5$ for discretized equations.

4.4.1. Flow Simulation

The **3D** steady-state **RANS** equations can be solved with the help of *Fine/Turbo* solver developed by Numeca International. In addition, the Hakim pre-conditioner was used for testing two separate turbulence models. They include *Spalart-Allmaras* and Shear Stress Transport (*SST*). Their performances were tested to evaluate their power production as well as pressure distribution, which were later compared with the experimental data, which is already available. That comparison between the obtained and available data based on separate turbulence models has been shown below:

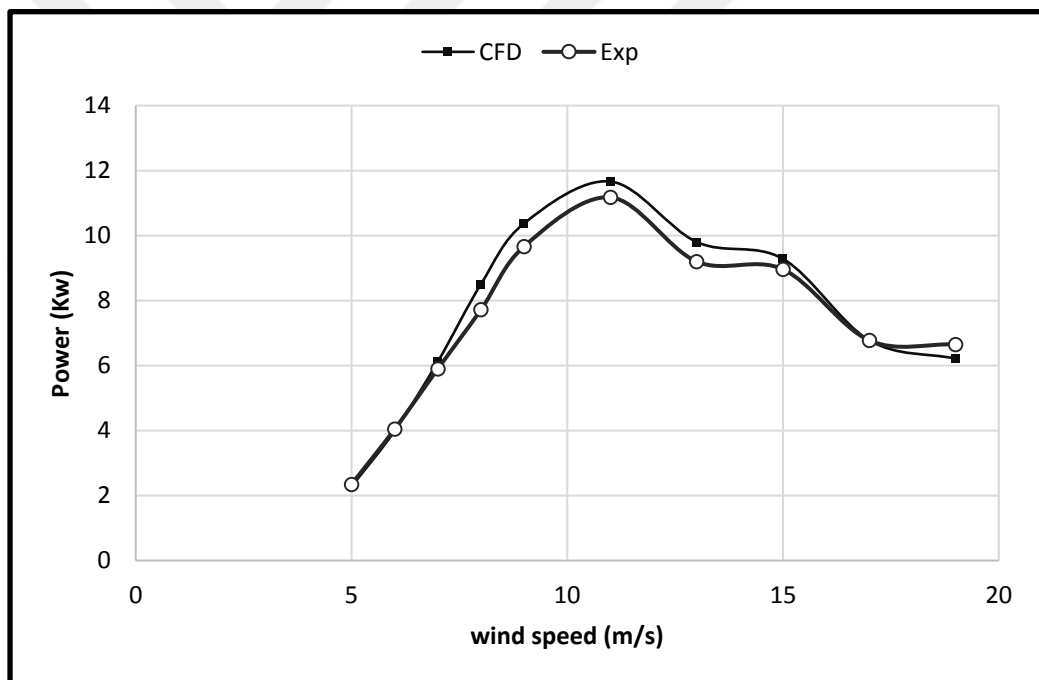


Figure 4.11: Power Generation Comparison: Experimental vs. Computed Power Generation using *NREL-VI*.

The results of power prediction have been listed in Table 4.4:

Table 4.4: Different Turbulence Models and their Power Generation (*NREL-VI*)

Speed (m/s)	Exp.data. Power (Kw)	SA power (Kw)	SSTpower (Kw)
5.08	2.34	2.39	2.34
6.05	4.03	4.02	4.10
7.05	5.89	6.38	6.31
8.03	7.71	8.84	8.72
9.06	9.66	10.45	10.1

The mentioned results show that the SST turbulence model provides the results, which are closest to the existing measurements. SST can accurately predict the correct power generation values at low, stalled or high wind speeds; therefore, we will use this model for the later calculations of our thesis.

The experiment shows installation of 22 pressure taps installed in 5 span-wise sections: 30%, 46.6%, 63.3%, 80% and 95%. The pairs having taps at 4% and 36% chord were installed. Their installation was accomplished at intermediate span locations. The installation of 5-hole probes was accomplished at 34%, 51%, 67%, 84% and 95% spans for measuring the dynamic pressure as well as the local effective attack angle.

The 3D gauge pressure contours, which were installed both on the pressure and suction sides, have been shown in Figures 4.12. In this case, the SST turbulence model was applied at 5, 10 and 15m/s wind speeds.

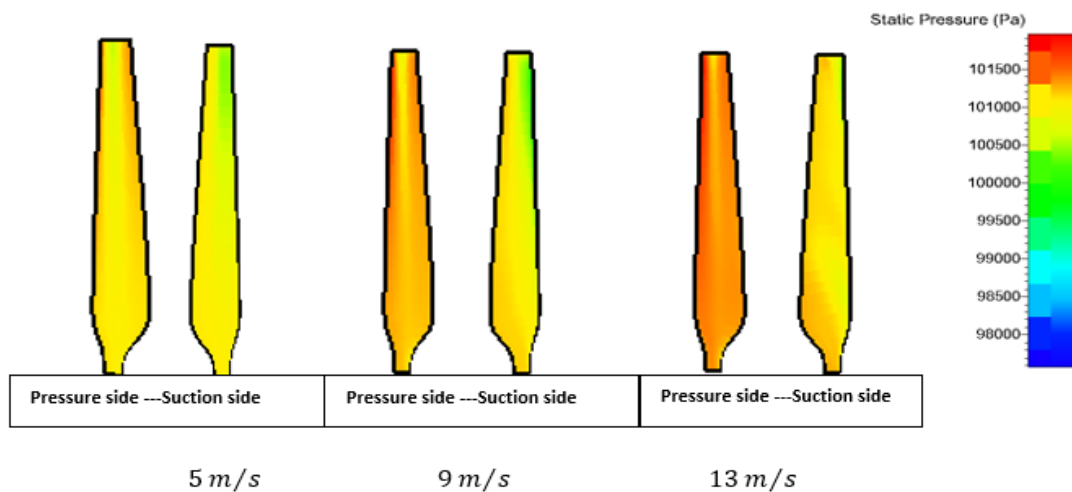


Figure 4.12: Pressure Contours

In case, there is some wind speed in (m/s), r represents section radius in m , represents rotational speed Ω (rad/s) and ρ represents free stream density (wind speed) in [kg/m^3]. They will help finding the pressure coefficient:

$$C_p = \frac{p - p_\infty}{\frac{1}{2}\rho_\infty(U_\infty^2 + (\Omega r)^2)} \quad (4.1)$$

Where,

ρ_∞ : density of the free stream [kg/m^3]

U_∞ : The wind speed [m/s]

Ω : The rotational speed [rad/s]

r : The radial distance from the center to the blade section [m]

The figures placed below show how the pressure coefficients are calculated through CFD using the SST turbulence model. The obtained values were compared with the experimental data considering three wind speeds: 5, 10, and 13 m/s for 5 distinct 3D blade sections: 30%, 47%, 63%, 80%, and 95%. The source of experimental results is given in the references [81]

The pressure contours, turbulent intensity and the pressure coefficient on pressure and suction sides of a wind turbine have been shown in the figures given below. As some studies have pointed out, the wind speed of just 5m/s results in laminar flow and the wind attaches to the blade span but not with the cylinder section, which is located at the base of the blade at the point that connects the blade to the hub. At 5m/s, no obvious transition took place; however, when the wind speed increased, transition took place in the outboard from the root section in the direction of the tip. The stagnation points of the dynamic pressure can be used to render the coefficient of pressure.

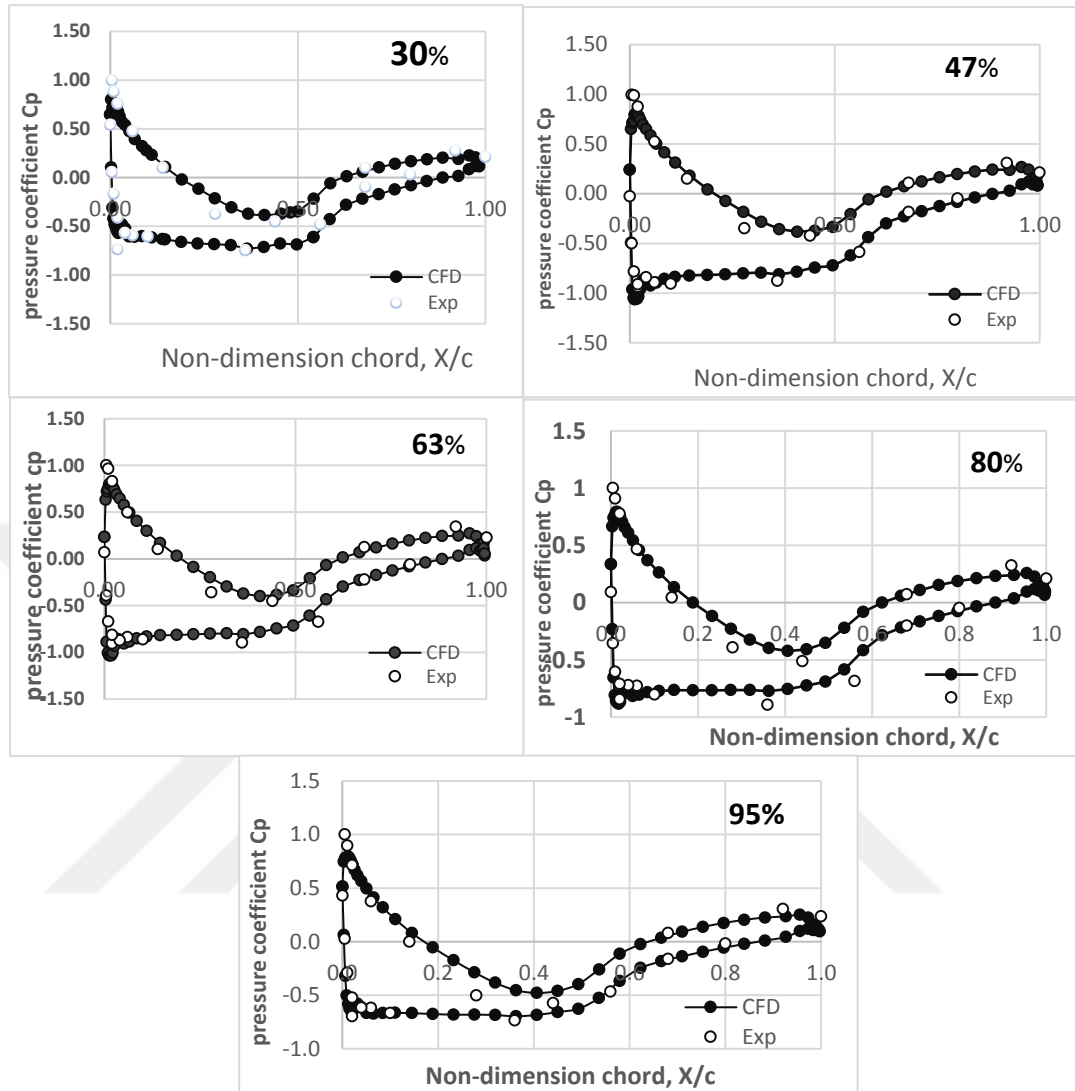


Figure 4.13: Experimental vs. Calculated Pressure Coefficients Span-Wise Sections (of *NREL-VI* at 5m/s)

The pressure coefficient for dimensionless x/c shows flow characteristics in a region. The plots shown above depict that at 5m/s, the pressure gradient displays the attached flow characteristics. The plots show large pressure differences along the primary section of the blade, which creates most of the lifting force to generate power. The comparisons with the literature and benchmark validation show that the mentioned plots show good agreement with the literature. And from plots, the velocity streamline at 5m/s shows completely attached lines having flow separation in the direction of the hub at the spot, at which, the cylinder extrusion, which connects the hub and the blade, is visible.

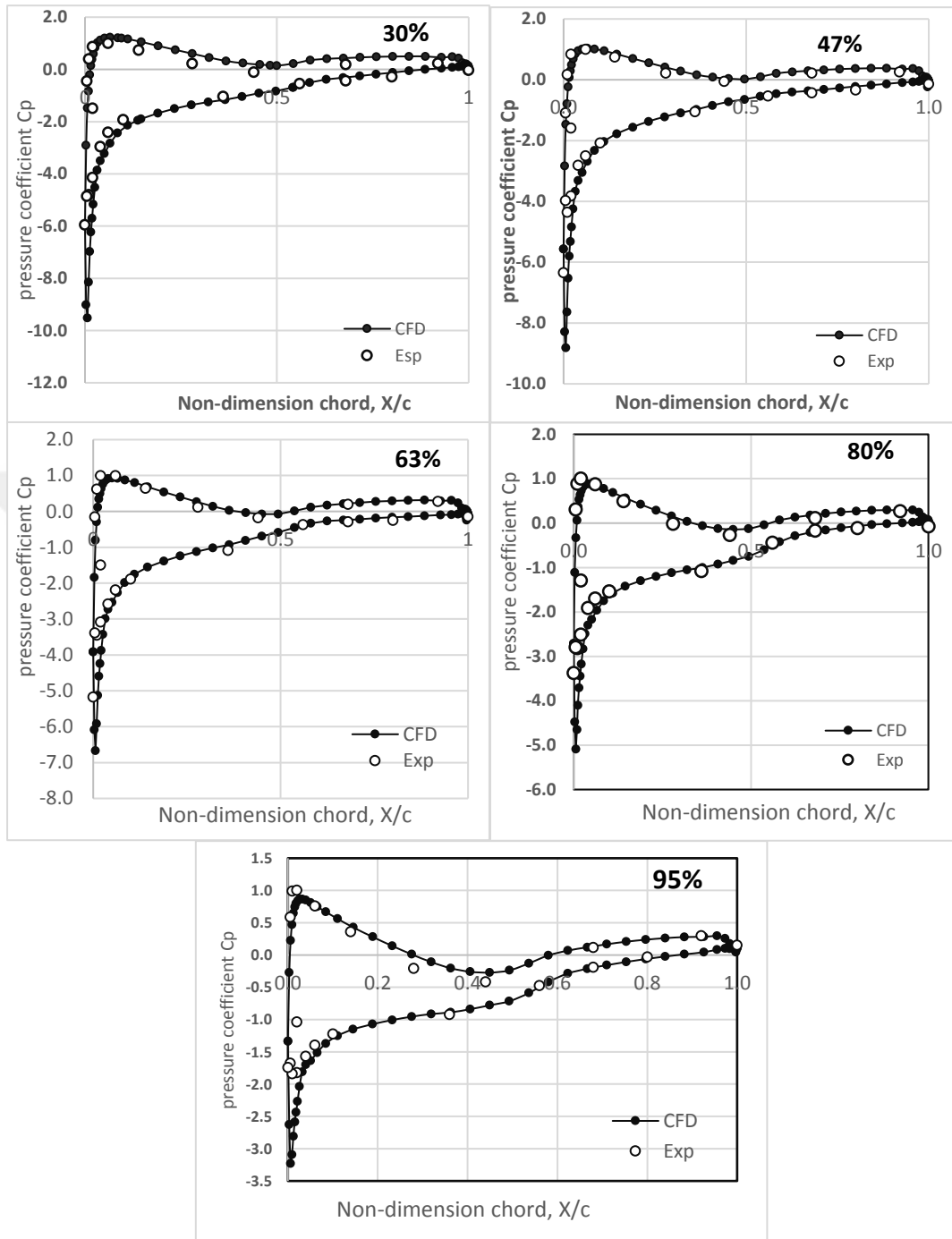


Figure 4.14: Experimental vs. Calculated Pressure Coefficients Span-Wise Sections of (NREL-VI at 10m/s)

Contrary to the low-speed and less windy situations, the speed of 10m/s marks the stall onset. A pressure coefficient distribution highlights the maximum adverse pressure gradients existing on the leading edge specifically towards its suction side. It was found that the flow separation can be observed very well at 30% span moving outboard towards 63% span-location. The turbulent separation progressively moves towards the trailing edge leaving from the direction of the leading edge when the transition moves outboard with the blade span. At almost 75%, the transition shifts towards the trailing edge. At 85%, the upward flow is attached over again. Between 30% and 63%, the second half of the blade suction side shows a constant pressure gradient that marks the stall onset within the local vicinity and in the area of separated flows. A little and decreasing pressure gradient is observable on the suction side immediately after the separation. It happens because of the rotational cross flows of wind. The suction-side streamlines, which indicates that the oblique vortex flows on the surface of the blade originating from the flow separation and the cross flows emerging from the rotation, which begin at the root of the blade, and later, it progressively moves outboard in the direction of the trailing edge, which was shown by the pressure coefficient plots.

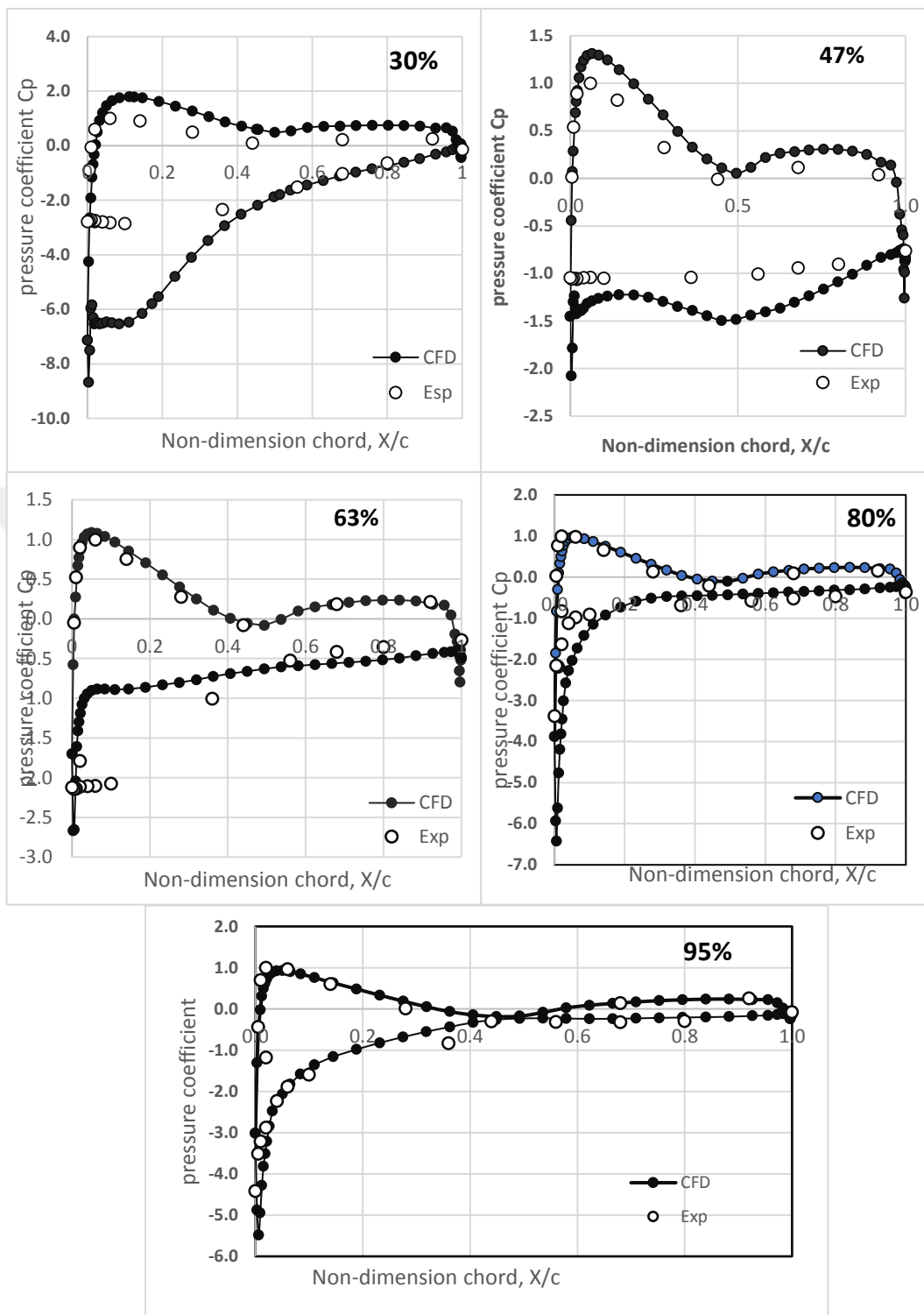


Figure 4.15: Experimental vs. Calculated Pressure Coefficients Span-Wise Sections of (NREL-VI at (13m/s)

At wind speed 13.1m/s, the turbulent flow can be seen from the plots at 80% span. The flow separation moves upwards from the suction side in the direction of the leading edge.

At radial spans 47% and 63%, positive pressure gradient moves in the direction of the trailing edge. The turbulent flows, which are highly separated, generate adverse pressure gradient that results in inappropriate approximation of the aerodynamic forces. At 95%, the pressure coefficient plot exhibits the properties of the attached flow.



Chapter 5

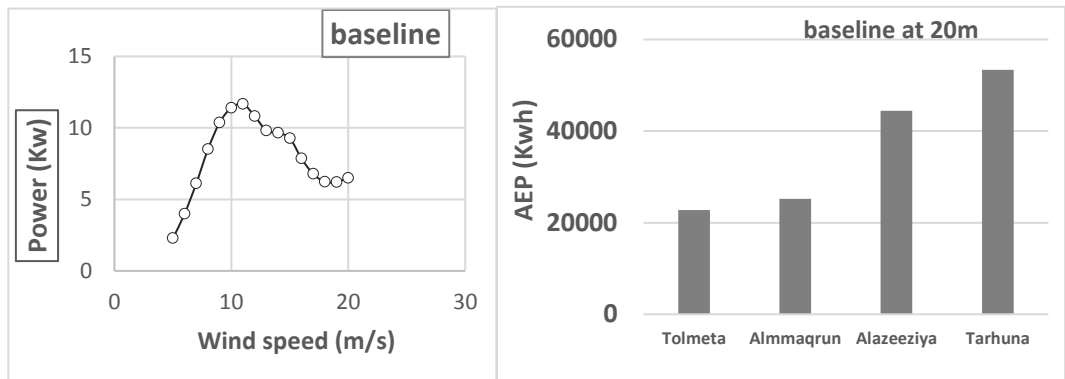
Results and Discussion

This chapter discusses the obtained results pertaining to the present value of costs (*PVC*) of the annual power generation in the sites, which use the same parameters (*K*, *C*). These parameters were used for analyzing the data that has already been filed in Chapter 2, in which, the case of a real turbine was discussed. After the selection of a turbine for experimental purpose (*NREL-VI*), *CFD* method was used to investigate and then analyze the experimental data obtained using the wind turbine (*3D* Reynolds-averaged Navier-Stokes). The results have been presented in Chapter 4. Efforts were made to obtain the best results with the most appropriate combination of the total annual energy production, power generation cost, wind turbine size, the control mechanism, optimized aerodynamic design of the wind turbine blade, and the blade tip pitch angle in order to get the maximum power output. The results are as follows:

5.1. Annual Energy and Power Curve of the Baseline turbine

The power curve for a baseline turbine was estimated using *CFD* and the annual energy production (*AEP*). The production calculations are very important for evaluating the wind energy projects. The long-term wind speed distribution is combined with the power curve of a specific wind turbine, which gives the information about the power generation at different wind speeds. Hence, it results in obtaining information about the total power generation in the whole year; so, *AEP* has been estimated at appropriate height (**20m**), which was estimated with the help of Equation 2.14 and there are many different ways to estimate the Weibull parameters (*k*, *C*). In this study, the maximum likelihood method (*MLM*) is implemented (For more details, see chapter 2).

The results for power curve, *AEP* and *C_f* are shown in figure 5.1. and table 5.1.



(a)

(b)

Figure 5.1. Power Curve of Baseline Turbine and Annual Energy of Sites

Table.5.1. The Results for AEP and C_f (NREL VI)

Site	AEP (kWh)	C_f (%)
Tolmeta	22768.59	25.99155
Almqrun	25187.42	28.75276
Alazeeziya	44466.26	50.76057
Tarhuna	53352.18	60.90432

5.2. Optimum Blade Tip Pitch Angles.

The baseline wind turbine is stall regulated which means that the blade tip pitch angle is fixed and does not change according to the current wind speed. At high wind speeds, strong vortices form behind the blade causing it to stall. Consequently, the power output reduces at speeds higher than the rated speed as seen in Figure 5.1(a). In the current study, the optimum blade tip pitch angle that corresponds to the maximum power output at each speed is chosen provided that the power output does not increase above the rated power of the wind turbine. If the maximum power output is above the rated power then the blade tip pitch angle that corresponds to the rated power, is selected as the optimum blade tip pitch angle. In this way, the stall regulated turbine becomes a pitch regulated one.

While the optimum pitch angle for the speeds below the rated speed is obtained to maximize the power at those speeds.

To find the optimum blade tip pitch angle, *CFD* analysis is performed for each speed at various blade tip pitch angle. The results of blade tip pitch angles for selected wind speeds are plotted in Figures (5.2,5.3, and 5.4)

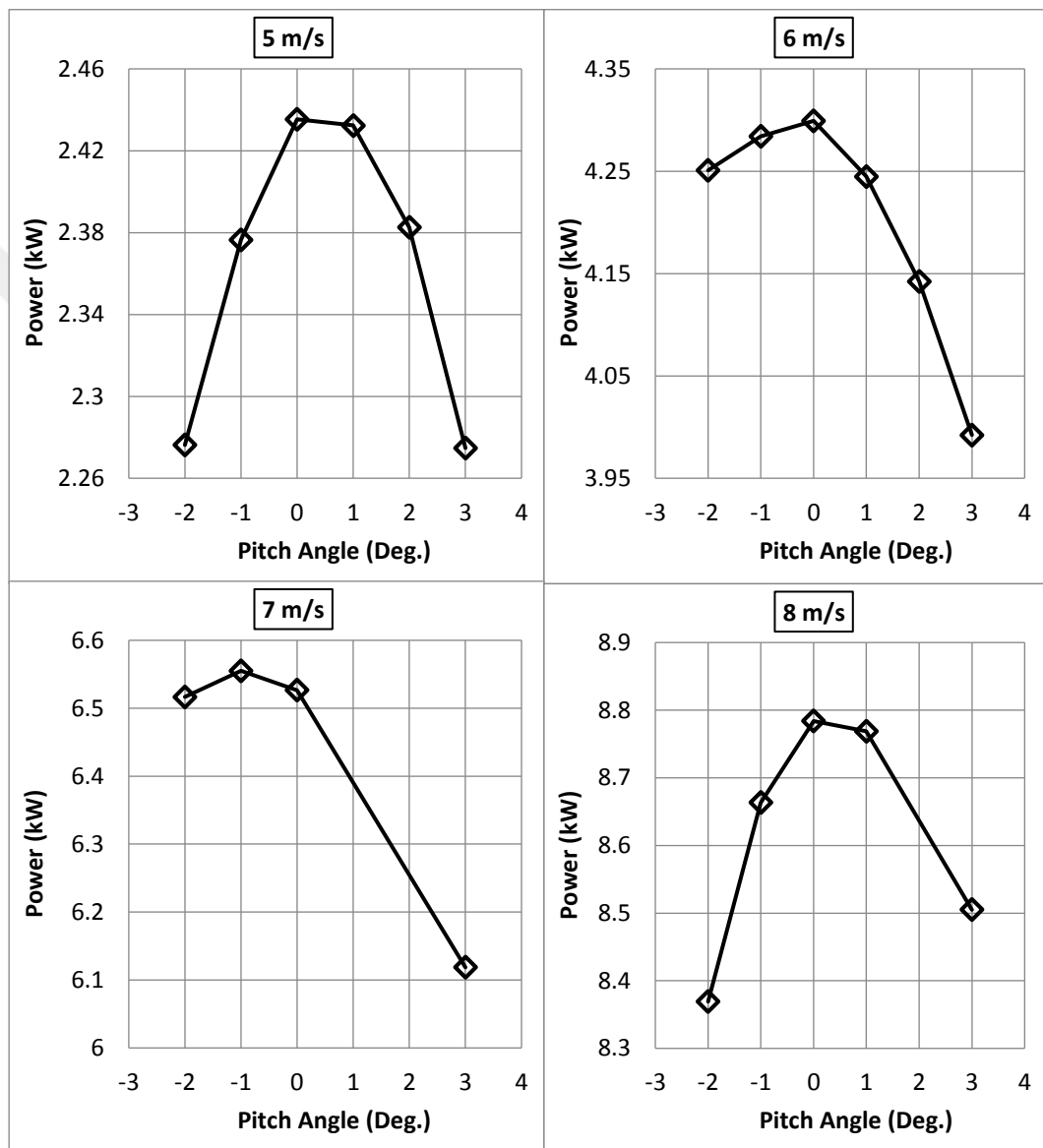


Figure 5.2. Optimum Blade Tip Pitch Angle at Different Wind Speeds.

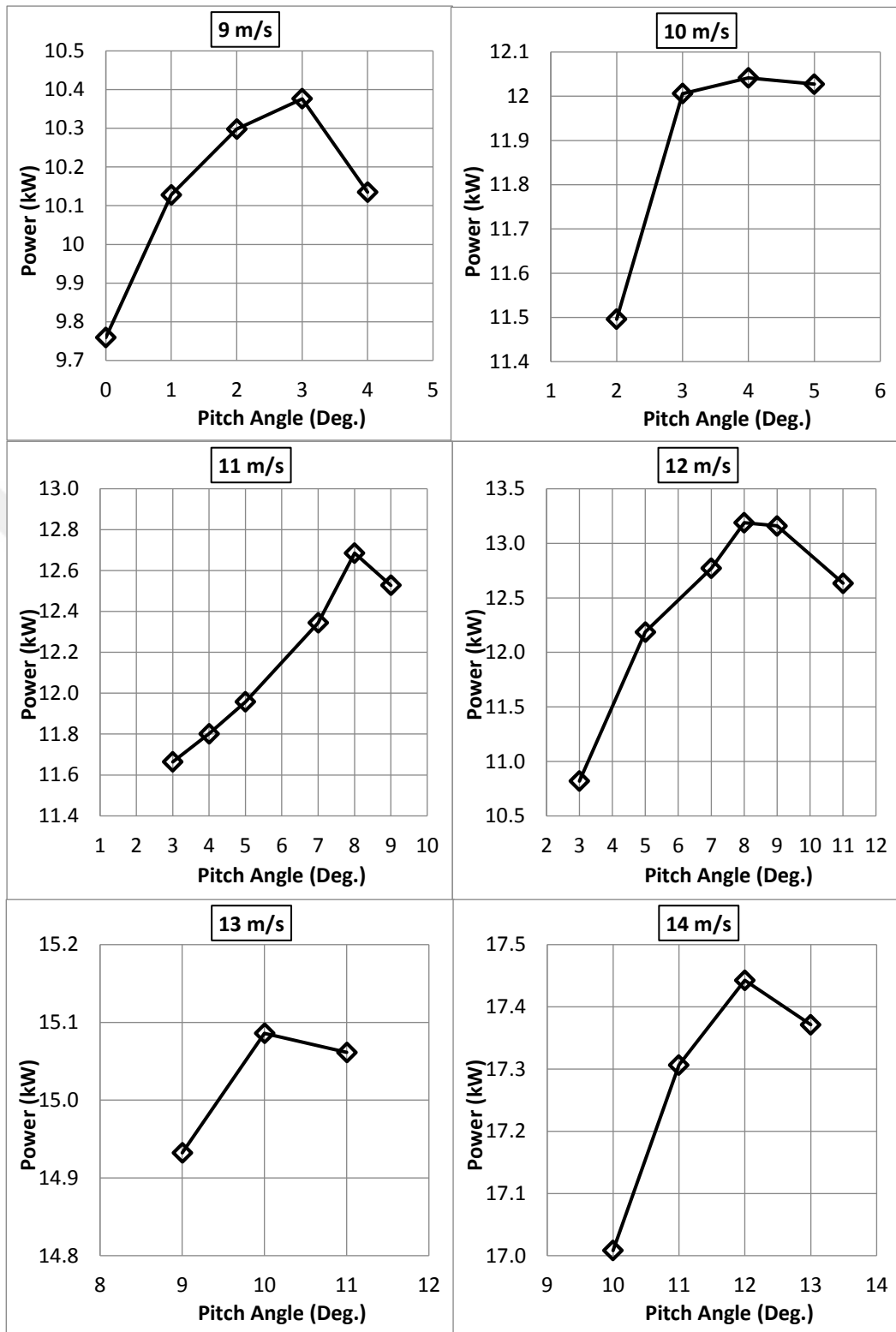


Figure 5.3 Optimum Blade Tip Pitch Angle at Different Wind Speeds.

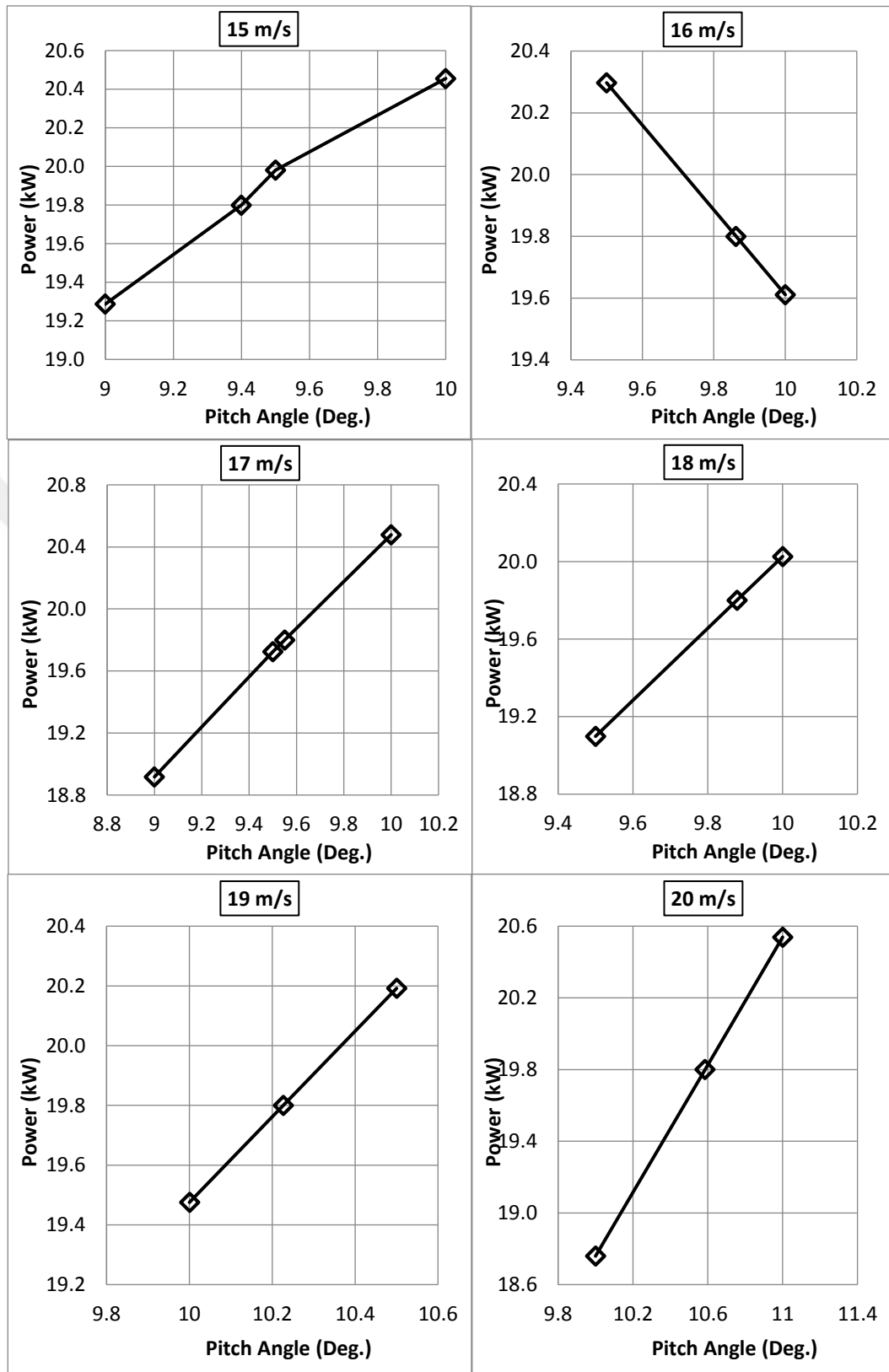


Figure 5.4. Optimum Blade Tip Pitch Angle at Different Wind Speeds.

It is notice from Figures (5.2-5.4) that at each speed up to 14m/s, the power output increases to a certain peak value as the blade tip pitch angle increases and then the power decreases again. The angle which corresponds to the peak power value is selected as the optimum blade tip pitch angle at that speed. At the speed 15 m/s, the power reaches the rated value of 19.8 kW at a pitch angle of 9.4°. This means that 15m/s is the rated speed and 9.4° is the optimum blade tip pitch angle at that rated speed. The results of the optimum blade tip pitch angles and the corresponding percentage of increase in power output at different wind speeds are summarized in Tables 5.2 and 5.3. At 9m/s, the optimum pitch is the same as the baseline blade tip pitch angle. A comparison between the optimum power output with the baseline turbine power is shown in Figure 5.5. The average increase of the power over the whole wind speed range is around 80%.

Table 5.2. Baseline Power Optimum Power at Different Wind Speeds.

Speed(m/s)	Baseline Power (Kw)	Opt.Power(Kw)
5	2.28	2.44
6	3.99	4.30
7	6.12	6.56
8	8.50	8.78
9	10.38	10.38
10	11.40	12.04
11	11.66	12.69
12	10.82	13.19
13	9.80	15.09
14	9.65	17.44
15	9.28	19.81
16	7.86	19.83
17	6.78	19.81
18	6.23	19.82
19	6.21	19.86
20	6.50	19.87

Table 5.3. Optimum Blade Tip Pitch Angles at Different Wind Speeds.

Wind Speed (m/s)	Optimum Pitch Angle (deg.)	Percentage of Increase in Power Output (%)
5.0	0.0	6.89
6.0	0.0	7.69
7.0	0.0	7.13
8.0	0.0	3.28
9.0	3.0	0.00
10.0	4.0	5.59
11.0	8.0	10.00
12.0	8.0	21.90
13.0	10.0	53.91
14.0	12.0	80.78
15.0	9.4	113.33
16.0	9.9	152.02
17.0	9.6	192.21
18.0	9.9	217.81
19.0	10.2	218.70
20.0	10.6	204.65

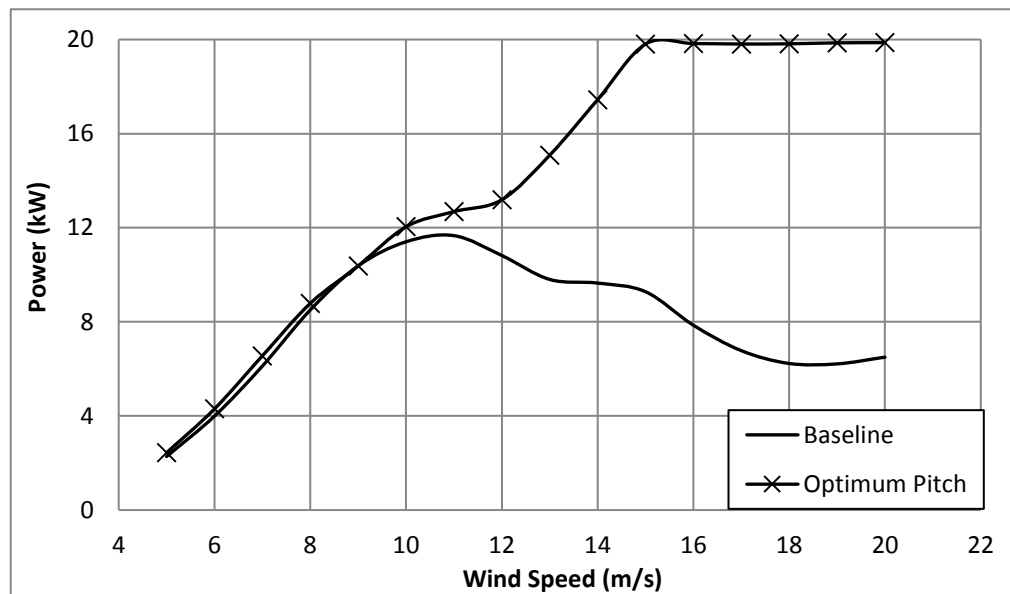


Figure 5.5. Comparison between the Optimum Power and the Baseline power.

5.3. Wind Turbine Blade Sizing

Some of the wind farms have relatively lower average wind speeds compared to others. For those farms, wind turbines of larger blades should be installed to capture more wind energy and produce more electricity. One aim of this study is to see the effects of wind turbine blade sizing on the energy output and to try to find a relation between the size and generated power. Three different blades with different sizes are analyzed. Those blades are obtained by increasing the size of the baseline blade by scale factors of 5%, 10% and 15%. Comparison between the scaled blades and the baseline blade is shown in Figure 5.6.

Two constraints are implemented for the scaling analysis. The first constraint is that the blade tip speed shall be the same as the baseline blade tip speed. This is achieved by decreasing the RPM such that the blade tip speed does not change. The *RPM* versus the scale factor is shown in Table 5.4. The second constraint is that the rated power of the scaled blade does not increase above the rated power of the baseline blade. This is accomplished by changing the blade tip pitch angle at speeds higher than the rated speed such that the rated power is not exceeded and kept fixed.

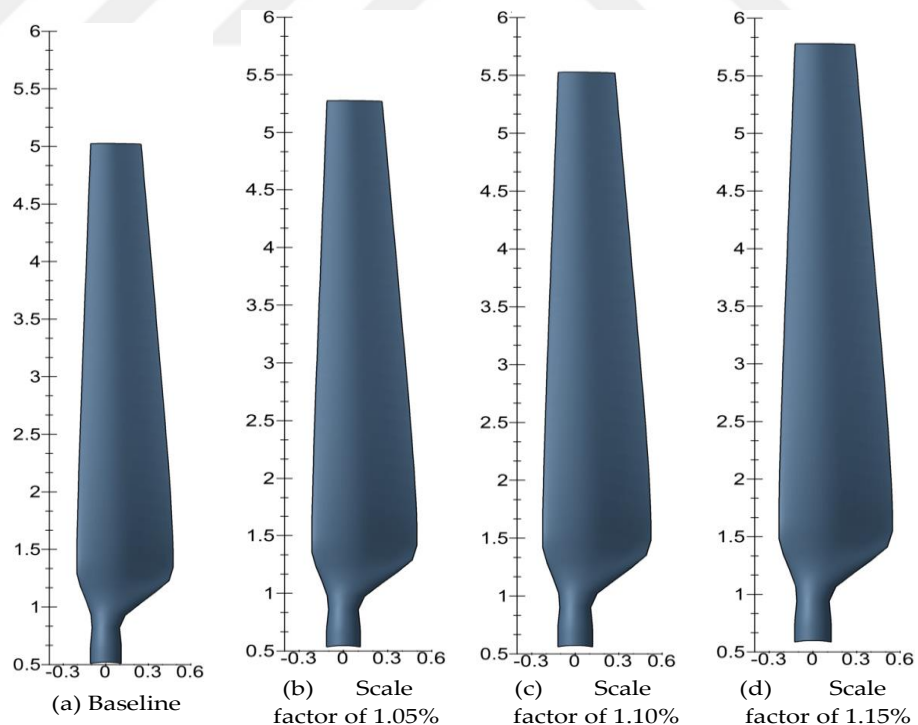


Figure 5.6. Blade Geometries with Different Scale Factors

Table 5.4. *RPM* Versus Scale Factor

Scale Factor	RPM
Baseline	72
5 %	68.58
10 %	65.46
15 %	62.61

The results of the computed power curves for different scales are compared to the baseline blade and the blade with blade tip pitch angle in Figure 5.7. All the results are calculated using the same *CFD* approach explained before. Notice that, results for the scaled blades at speeds lower than the rated speed are obtained at the optimum blade tip pitch angles stated in the preceding section. The rated power value of 19.8 kw is used at speeds equal to and higher than the rated speed. In the figure, we notice that the rated wind speed for the blade with 1.05 scale factor is 15m/s which is the same as the rated speed of the baseline blade but at different blade tip pitch angle. The rated power was reached at a rated speed of 14 m/s for the scale factor 1.1 and at 13m/s for the scale factor 1.15.

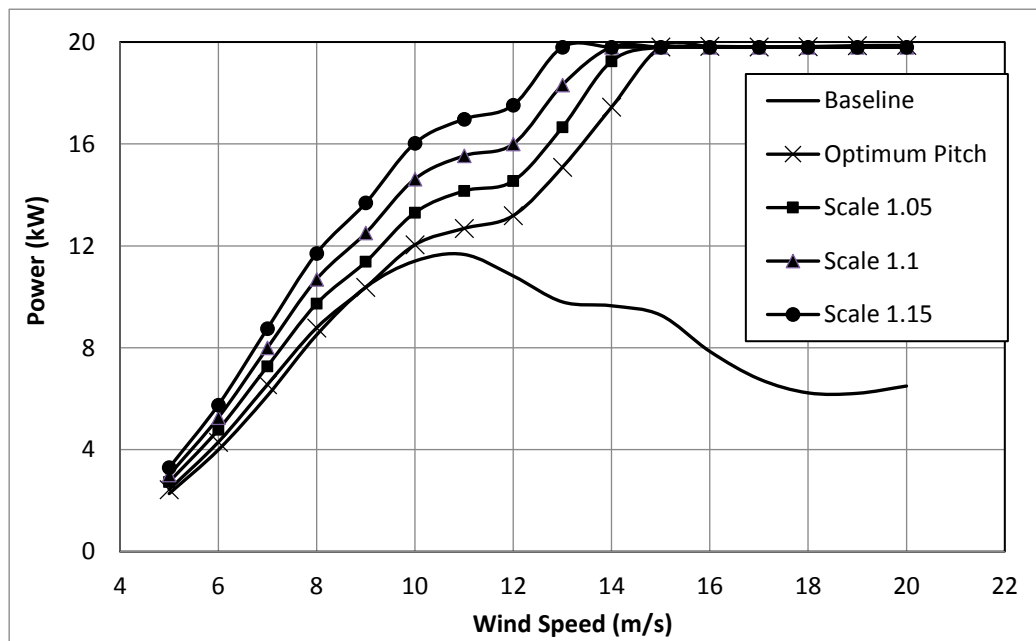


Figure 5.7. Comparison of Power Curves for Different Scales

Table 5.5. Comparison of Power Output Percentage increase for the Different Scales

Wind Speed (m/s)	Percentage of Increase in Power Output (%)		
	Optimum Pitch with 1.05 scale	Optimum Pitch with 1.1 scale	Optimum Pitch with 1.15 scale
5.0	12.55	23.69	35.51
6.0	11.35	22.30	33.88
7.0	10.98	22.04	33.63
8.0	10.78	21.74	33.31
9.0	9.63	20.54	31.92
10.0	10.50	21.47	33.12
11.0	10.33	21.10	32.30
12.0	10.29	21.32	32.88
13.0	10.42	21.43	-
14.0	10.37	-	-

The percentage of increase in power output is compared for the different scales in Table 5.5 at speeds lower than the rated speed. From the table, it is noticed that, increasing the blade size by a scale factor of 1.05 results in increasing the power output by an average value of 10.7%.

Similarly, increasing the size by factors of 1.1 and 1.15 result in increasing the power output by an average value of 21.7% and 33.1% respectively. It seems that the relation between the blade size and generated power output is such that each 5% increase in blade size leads to an increase of around 11% in the generated power.

However, to prove such a relation more excessive work should be conducted to study different wind turbines and different scales.

High increase in power output was attained by optimizing the blade tip pitch angle and increasing the blade size. The main objective of this study is to see the effects of optimizing the blade tip pitch angle and sizing the blade on the electricity cost. The electricity cost is estimated using both of the power curves of the wind turbine, wind data of the site and the cost of the wind turbine. To do so, wind assessment based on wind real data is carried out as shown in the coming section.

5.4. Electricity and Present Value Cost, PVC

In this section, the *AEP* is estimated, and the cost analysis is carried out for the analyzed sites using both of the baseline wind turbine, wind turbine with optimum pitch and wind turbine with different scales.

Table 5.6 shows the monthly and annual averages of the measured wind speeds in each site. It is clear from that Tarhuna has a high mean wind speeds along the year while the average wind speed in Tolmeita is relatively low.

Table 5.6: Mean Wind Speeds at 20 m Height

Site	Monthly Average Wind Speeds (m/s)												Annual Averages (m/s)
	Jan.	Feb.	Mar.	Apr.	May	Jun.	Jul.	Aug.	Sep.	Oct.	Nov.	Dec.	
Tolmeta	5.94	4.89	5.13	5.30	3.70	3.32	3.02	2.87	4.42	4.09	5.10	6.17	4.50
Almqrun	4.47	4.59	5.29	5.47	5.28	5.08	5.22	4.70	4.62	3.76	4.09	5.06	4.80
Alazeeziya	5.50	6.72	6.58	7.57	5.78	6.18	4.67	5.47	5.01	6.11	5.90	6.12	5.97
Tarhuna	5.63	7.26	6.80	9.66	6.88	7.37	5.95	6.38	6.41	7.02	6.15	5.60	6.76

Using the *CFD* results of the power curves for all the analyzed blades (Figure 5.8) together with the sites wind data including the Weibull parameters, the *AEP* is tabulated in Table 5.7 which also shows the percentage of increase in *AEP* with respect to the baseline blade.

Table 5.7. Comparison of the Annual Energy Production

Site	Baseline	Optimum Pitch		1.05 Scale Factor		1.10 Scale Factor		1.15 Scale Factor	
	AEP (MWh)	AEP (MWh)	Increase (%)	AEP (MWh)	Increase (%)	AEP (MWh)	Increase (%)	AEP (MWh)	Increase (%)
Tolmeita	22.76	24.44	7.33	27.05	18.80	29.69	30.39	32.45	42.52
Almqrun	25.18	27.04	7.37	29.92	18.82	32.84	30.41	35.90	42.54
Alazeeziya	44.47	50.25	13.01	55.30	24.37	60.40	35.82	65.64	47.61
Tarhuna	53.35	60.67	13.70	66.75	25.12	72.86	36.57	79.14	48.34

The results in Table 5.7 show that Tarhuna site yields more energy than Tolmeita, Almqrn and Alazeeziya due to its higher average wind speed (Table 5.6). Another important notice is that, with the optimum pitch, the increase in AEP is more for Tarhuna (13.7%) than for Tolmeita (7.33%), Almqrn (7.37%) and Alazeeziya (13%). The reason is explained as follow: the optimum pitch gives higher power difference from the baseline blade towards the high-speed region. Figure 5.6 shows that the difference in power generation with optimum pitch becomes very pronounced at speeds higher than 11m/s. The wind data of the sites tells us that only 3.8% of the recorded wind speeds are above 11 m/s in Almqrn site, 5.17% in Tolmeita, 11% in Alazeeziya and around 16% of the wind speeds are recorded above 11m/s in Tarhuna site. So, the optimum pitch is more effective for the case of Tarhuna site due to its more frequent high speeds.

To calculate the present value cost, *PVC*, the values of the different terms in equation (2.20) should be determined. In this study, the values of those terms have been calculated based on some assumptions which have been used as standard in many articles [55,82, 83]. The calculated and assumed terms and the computed *PVC* are listed in Table 7. The cost of the turbine is estimated from Adaramola et al. [84] as 1775\$ per each kW for commercial wind turbines of around 20kW rated power. Notice that, 3% of the turbine cost was added to the cost of the baseline turbine as the cost of the pitch mechanism. Also, it is assumed that increasing the size by a certain scale factor would increase the turbine price by the same factor.

Table 5.8. The Values of the Terms in the *PVC* Equation and the Calculated *PVC*.

Term	Assumed/Calculated Value				
	Baseline	Optimum Pitch	1.05 Scale	1.10 Scale	1.15 Scale
Turbine cost	35,145 USD	36,200 USD	38,000 USD	39,820 USD	41,630 USD
Investment, <i>I</i>	42,174 USD	43,440 USD	45,610 USD	47,780 USD	49,950 USD
OMR cost, <i>C_{omr}</i>	440 USD	453 USD	475 USD	498 USD	520 USD
Inflation Rate, <i>i</i>	0.12	0.12	0.12	0.12	0.12
Interest Rate, <i>r</i>	0.15	0.15	0.15	0.15	0.15
Scrap Value, <i>S</i>	4,220 USD	4,345 USD	4,560 USD	4,780 USD	5,000 USD
PVC	46,420 USD	47,820 USD	50,200 USD	52,600 USD	55,000 USD

The cost of each *kWh* produced by the turbine in, *USD* cent/kWh, is calculated from equations (2.21,2.23) for a turbine life time of 20 years. The results of the electricity price are shown in Table 5.9, 5.10 and the percentage of the electricity cost reduction with respect to the cost of the baseline blade is shown in Table 5.11.

Table 5.9. Electricity cost of each kWh for each site at Different blade Configurations.

Site	Electricity cost (USD cent/kWh)				
	Baseline	Optimum Pitch	1.05 Scale	1.10 Scale	1.15 Scale
Tolmeta	10.19	9.78	9.28	8.85	8.47
Almqrun	9.21	8.84	8.38	8.00	7.65
Alazeeziya	5.22	4.76	4.54	4.35	4.19
Tarhuna	4.35	3.94	3.76	3.61	3.47

Table 5.10. Electricity Cost of each kWh for each site at Different blade Configurations with Reduction.

Site	Electricity cost (USD cent/kWh)			
	Optimum Pitch	1.05 Scale	1.10 Scale	1.15 Scale
Tolmeta	9.38	8.45	7.69	7.04
Almqrun	8.48	7.62	6.95	6.36
Alazeeziya	4.34	3.94	3.63	3.36
Tarhuna	3.56	3.24	2.99	2.77

Table 5.11. Percentage of Reduction in Electricity Cost.

Site	Electricity cost reduction (%)			
	Optimum Pitch	1.05 Scale	1.10 Scale	1.15 Scale
Tolmeta	4.04	8.86	13.10	16.89
Almqrun	4.07	8.98	13.13	16.90
Alazeeziya	8.85	13.04	16.58	19.75
Tarhuna	9.54	13.64	17.11	20.20

Those calculated electricity costs correspond to the minimum price at which the electricity produced by the wind turbine should be sold such that the turbine will be able to payback itself within the specified turbine life. According to statistical web

sites, the average price of electricity in the world is around 8 - 15 cent/kWh. This means that Tarhuna site is feasible for wind energy projects even with the baseline wind turbine where the electricity cost is 4.35 *USD* cent/kWh. However, to make Tolmeita site feasible (reduce the electricity cost below the minimum average price in the world), optimum pitch with a scale factor of 1.15 for the blades should be used.



Chapter 6

Conclusion and Recommendations

6.1 Conclusion Remarks

In this study, wind energy assessment of four different sites close to the Libyan coast was conducted using available measured wind data. The assessment includes technical evaluation of the annual energy production and capacity factor and financial assessment to calculate the electricity cost per kWh. Greenhouse Gas emission effects on the cost analysis was also stated. The annual energy production was calculated using the Weibull distribution function. Three different methods were implemented to calculate the Weibull parameters (shape and scale factors); graphical method, empirical method and maximum likelihood method to see the effects of implementing different methods on the results. The annual energy production analysis showed that Tarhuna and Alazeeziya sites have the highest wind energy potential compared to the other sites. The cost analysis was done by means of present value of cost formula which is used in the calculation of the minimum cost of each kWh electrical energy produced by the wind turbines so that the wind energy project becomes feasible within the turbine lifetime. The results showed that Tarhuna site yields the lowest value of the kWh cost followed by Alazeeziya, then Almqrn and Tolmeita. Applying different Weibull methods results in different estimations for AEP, C_f , electricity cost and annual GHG reduction values. The GM method gives lower values for AEP, C_f and annual GHG reduction and higher values for the electricity cost. Where the MLM method gives higher values for AEP, C_f and annual GHG reduction and consequently lower values for electricity cost. The kWh cost in Tolmeita was calculated with the GM method as 6.13 USD cent/kWh and the average price for kWh sold in the world is about 8 USD cent/kWh. This means that even Tolmeita (with the lowest potential among the other cities in this study) would be feasible for wind projects and will be able to return the cost of the project in a period less than the wind turbine lifetime. Adding the contribution of GHG reduction caused by using the wind turbine in electricity generation reduces the kWh cost of the generated electricity by an average of around 18% for the selected sites. Such reduction in the electricity price makes the wind energy project in any of the selected sites more feasible for investment.

In the present study also, incorporation between CFD analysis and wind assessment was conducted. The CFD analyses were performed to find the optimum blade tip pitch angle at different wind speeds for the stall regulated NREL VI wind turbine and to convert this turbine into pitch regulated one. The new pitch regulated turbine was resized by three different scales. The effects of the pitch and scales on the AEP and generated electricity cost were compared and discussed.

The results show that, changing the turbine into pitch regulated one with the optimum blade tip pitch angle at speeds lower than the rated speed enhances the wind turbine performance. The implementation of the optimum pitch increases the power output by an average of 7.81 % for speeds up to 12 m/s and by an average of 154.18 % for speeds above 12 m/s compared to the baseline blade.

Adding the effects of scaling factor to the optimum blade tip pitch angle, the results show that the power output increases by averages of 10.7 %, 21.7 % and 33.1 % for the scale factors of 1.05, 1.10 and 1.15 respectively compared to the blade with optimum blade tip pitch angle without scaling. This indicates that, each 5% increase in blade size results in approximately 11% increase in power output. However, to validate this relation between the size and power output, more work on different wind turbines and using more various scales should be performed.

Computed power output data for all the analyzed cases were used together with the read wind data of four sites, Tolmeita ,Almqrun,Alazeeziye and Tarhuna, to estimate AEP and electricity cost. The results have demonstrated, AEP significantly increases for both of the sites. Also, there is an important reduction in the electricity cost for each site.

6.2. Future Work

In order to support and further validate the relationship between size and power output, more researches should be conducted on different wind turbines using diverse scales.

This is recommended for the expansion of the studies in terms of analysis and design in the field of wind energy, which is a futuristic option to meet the energy needs in Libya and several other countries.

References

- [1] Ashby, G. 2008. How Much Power Does a Wind Mill Generate? Read 20.04.2012 <http://ezinearticles.com/?How-Much-Power-Does-a-Wind-Mill--Generate?&id=1808270>
- [2] J F Manwell (and others) published the chapter: Wind Energy Explained: Theory, Design and Application, Second Edition in a book. Dec 22, 2017 - On Mar 1, 2006,
- [3] Rohatgi, J. S., Nelson, V. (1994) Wind Characteristics: An Analysis for the Generation of Wind Power. Alternative Energy Institute, Canyon, TX.
- [4] Golding, E.W.: The Generation of Electricity by Wind Power. E. & F.N. Spon Ltd. New York (1977)
- [5] Stein, D.: Windkraftanlagen in Dänemark, RAW-Denkschrift 4, Berlin (1942)
- [6] Westh, C.: Experiences with the F.L. Smidth Aeromotors. In: 6th IEA Expert Meeting LS-WECS, Aalborg (1981) Leipzig (1933)
- [7] Betz, A.: Das Maximum der theoretisch möglichen Ausnutzung des Windes durch Windmotoren, Zeitschrift für das gesamte Turbinenwesen (September 20, 1920)
- [8] Kleinhenz, F.: Das Großwindkraftwerk MAN-Kleinhenz. RAW Denkschrift (1941).
- [9] Putnam, P.C.: Power from the Wind. Van Nostrand Reinold Company, New York (1947)
- [10] <https://www.turbinesinfo.com/horizontal-axis-wind-turbines-hawt/>.
- [11] W. Tong, Wind Power Generation and Wind Turbine Design, Southampon: WIT Press, 2010.
- [12] <http://www.green-mechanic.com/2013/03/vertical-axis-wind-turbine-parts.html>
- [13] Wilson, R. E. & Lissome, P. B. S. (1974), Applied Aerodynamics of Wind Power Machines, Oregon State University, Corvallis, Oregon.
- [14] Manwell, J., McGowan, J., and Rogers, A. (2002). Wind Energy Explained. Theory, Design and Application. John Wiley and Sons, Ltd. Walker, J. and Jenkins, N. (1997). Wind Energy Technology. John Wiley and Sons, Ltd. 21
- [15] Actuator disk model of a wind turbine, adapted from (Jonkman 2003, Manwell et al. 2002).

- [16] Erich Hau, “Wind Turbines”, 2nd Edition, Springer, 2006.
- [17] Pedersen, M.B. and Nielsen, P. “Description of the two Danish 630 kW Wind Turbines Nibe A and Nibe B. Kopenhagen”, 3. BHRA International Symposium on Wind Energy Systems 26–29 Aug., 1980
- [18] Hansen M.O.L. Sorensen J.N. Voutsinas S. Sorensen N. and Madsen H.Aa. State of the art in wind turbine aerodynamics and aeroelasticity. Progress in Aerospace Sciences, 42:285–330, 2006.
- [19] Sorensen J.N. and Shen W.Z. Numerical modeling of wind turbine wakes. Journal of Fluid Engineering, 124:393–9, 2002.
- [20] Earl P. N. Duque, C. P. van Dam, and Shannon C. Hughes, “Navier-Stokes Simulations of The NREL Combined Experiment Phase II Rotor”, AIAA paper 99-0037, January 1999.
- [21] Sorensen, N. N., and Michelsen, J. A., “Aerodynamic predictions for the Unsteady Aerodynamics Experiment Phase II rotor at the National Renewable Energy Laboratory”, AIAA paper 2000-0037, 2000
- [22] Gupta, A., “Prediction of aerodynamic forces on wind turbine blades using computational fluid dynamics”, Master Thesis, Applied Science in Industrial Systems Engineering, University of Regina, 2007.
- [23] Nilay Sezer-Uzol, “Unsteady Flow Simulations Around Complex Geometries Using Stationery or Rotating Unstructured Grids”, PhD Thesis, The Pennsylvania State University, 2006.
- [24] Guanpeng Xu, “Computational Studies of Horizontal Axis Wind Turbines”, PhD thesis, Georgia Institute of Technology, May 2001.
- [25] Sarun Benjanirat, “Computational studies of horizontal axis wind turbines in high wind speed condition using advanced turbulence models”, PhD thesis, Georgia Institute of Technology, December 2007.
- [26] <http://www.gecol.ly/asp/Statistics.aspx>
- [27] Mohamed, A., A. Al-Habaibeh, and H. Abdo, An investigation into the current utilisation and prospective of renewable energy resources and technologies in Libya. Renewable Energy, 2013. 50: p. 732-740.
- [28] REAOL, “Renewable Energy Authority of Libya” Director of Projects Department, Tripoli, 2012-2013

- [29] Ahmed M. A. Mohamed, Amin Al-Habaibeh, Hafez Abdo and Mohammad Juma R. Abdunnabi, "The significance of Utilizing Renewable Energy Options into the Libyan Energy Mix", *Energy Research Journal*, 4 (1), 15-23, 2013.
- [30] M. S. Elmnefi and A. M. Bofares, "An Analysis of Wind Speed Distribution at Benina, Benghazi, Libya", *Applied Mechanics and Materials*, Vol. 492, pp: 550-555, (2014) DOI: 10.4028/www.scientific.net/AMM.492.550
- [31] Ahmed M.A. Mohamed, Amin Al-Habaibeh, Hafez Abdo, "An investigation into the current utilisation and prospective of renewable energy resources and technologies in Libya", *Renewable Energy* Vol. 50, pp: 732-740, (2013). doi: <http://doi.org/10.1016/j.renene.2012.07.038>
- [32] Satya P. Bindra, Farag Soul, S.D. Jabu, A. Allawafi, A.M. Belashher, H. Reani, S. Abulifa, and Khalifa Hammuda, "Potentials and Prospects of Renewables in Libya", *Progress in Clean Energy*, V. II: Novel Systems and Applications, Ch. 55, pp: 851-861, (2015).
- [33] W. El-Osta, M. Belhag, M. Klat, I. Fallah and Y. Kalifa, "Wind Farm Pilot Project in Libya", *Renewable Energy*, Vol.6, No. 5-6, pp: 639-642, (1995). DOI: [https://doi.org/10.1016/0960-1481\(95\)00061-N](https://doi.org/10.1016/0960-1481(95)00061-N)
- [34] W. El-Osta, Y. Kalifa, "Prospects of wind power plants in Libya: a case study", *Renewable Energy* V. 28, pp: 363–371, (2003). DOI: [http://doi.org/10.1016/S0960-1481\(02\)00051-4](http://doi.org/10.1016/S0960-1481(02)00051-4)
- [35] Wedad B. El-Osta, Mohamed Ali Ekhlal, Amal S. Yagoub, Yousef Khalifa and E. Borass "Estimation of capacity credit for wind power in Libya", *Int. J. Energy Technology and Policy*, Vol.3, No.4, pp: 363-377, (2005). DOI: <http://dx.doi.org/10.1504/IJETP.2005.008401>
- [36] Dimitrios Mentis, Sebastian Hermann, Mark Howells, Manuel Welsch and Shahid Hussain Siyal, "Assessing the technical wind energy potential in Africa a GIS-based Approach", *Renewable Energy*, vol. 83, pp: 110-125, (2015). DOI: <http://doi.org/10.1016/j.renene.2015.03.072>
- [37] Y. Song* and J. B. Perot CFD Simulation of the NREL Phase VI Rotor.
- [38] N.N. S0rensen, J.A. Michelsen (c) 2002 American Institute of Aeronautics & Astronautics or Published with Permission of Author(s) and/or Author(s)' Sponsoring Organization.

- [39] J .F. Manwell, J.G. McGowan, and A.L. Rogers, *Wind Energy Explained: Theory, Design and Application*, John Wiley & Sons Ltd.: West Sussex, England, pp. 38- 57, 2002. (Book)
- [40] R. D. Christofferson, and D. A. Gillette, “A simple estimator of the shape factor of the two- parameter Weibull distribution”, *Journal of J. Clim. Appl. Meteorol.*, Vol. 26, pp. 323–325, 1987. (Article)
- [41] C. R. Ranganathan, M. Ramanathan, and K. R. Swaminthan, Estimation of wind power availability inTamil Nadu”, *Renew. Energy*, DOI: 429–434, 10.1016/0960-1481(91)90053-R, Vol. 1, pp. 429-434,1991. (Article)
- [42] Isaac Lun Y. F. and Joseph Lam C., “A study ofWeibull parameters using long-term wind observations”, *Renew. Energy*, DOI: 10.1016/S0960-1481(99)00103-22000, Vol. 20, pp. 145–153, 2000. (Article).
- [43] Jaramillo O. A., Salana R., and Miranda U., “Wind power potential of Baja California Sur, Mexico”,*Renew. Energy*, DOI: 10.1016/j.renene.2004.03.004, Vol. 29, pp. 2087–2100, 2004. (Article)
- [44] A. Balouktsis, D. Chassapis, and T. D. Karapantsios,“A nomogram method for estimating the energy produced by wind turbine generators”, *Sol. Energy*,DOI: 10.1016/S0038-092X(01)00099-8, Vol. 72, pp. 251-259, 2002. (Article)
- [45] Tatiane C. Carneiro, Sofia P. Melo, Paulo C.M. Carvalho, and Arthur Plínio de S. Braga., “Particle swarm optimization method for estimation of Weibull parameters: a case study for the Brazilian northeast region” *Renew. Energy*, DOI: 10.1016/j.renene.2015.08.060, Vol. 86, pp. 751-759,2016. (Article)
- [46] F. Fazelpour, E. Markarian, and N. Soltani, “Windenergy potential and economic assessment of four locations in Sistan and Balouchestan province in Iran”*Renew. Energy*, DOI: 10.1016/j.renene.2017.03.072, Vol. 109, pp. 646-667, 2017. (Article)
- [47] Costa Rocha P.A., de Sousa R.C., de Andrade C.F., and da Silva M.E.V., “Comparison of seven numericalmethods for determining Weibull parameters for wind energy generation in the northeast region of Brazil”*Appl. Energy*, DOI: 10.1016/j.apenergy.2011.08.003,Vol. 89, pp. 395–400, 2012. (Article).
- [48] De Miguel A., and Bilbao J., “Test reference yeargeneration from meteorological and simulated solar radiation data”, *Sol. Energy*, DOI: 10.1016/j.solener.2004.09.015, Vol. 78, pp. 695- 703, 2005. (Article)
- [49] M. Baseer, J. Meyer, S. Rehman, and M.M. Alam, “Wind power characteristics of seven data collection sites in Jubail, Saudi Arabia using Weibull parameters”,*Renew. Energy*, DOI: 10.1016/j.renene.2016.10.040, Vol. 102, pp. 35-49, 2017. (Article)

- [50] J. Bilbao, A. De Miguel, A. Ayuso, and J. Franco, “Isoradiation maps for tilted surfaces in the Castile and Leon region, Spain”, *Energy Convers. Manag.*, DOI:10.1016/S0196-8904(02)00161-9, Vol. 44, pp. 1575-1588, 2003. (Article)
- [51] Martin O. L. Hansen, *Aerodynamics of Wind Turbines*, 2nd ed., Earthscan: London, UK, pp. 55-57, 2008. (Book)
- [52] ENERCON GmbH. ENERCON Wind energy converters: product overview. Online Source, July, 2010.
- [53] Lysen E. H., *Introduction to wind energy*, 2nd ed., CWD 82-1 Consultancy Services: Amersfoort, The Netherlands, 1983, pp. 261-279. (Book)
- [54] S. Rehman, T.O. Halawani, M. Mohandes, “Wind power cost assessment at twenty locations in the kingdom of Saudi Arabia” *Renew. Energy*, DOI:10.1016/S0960-1481(02)00063-0, Vol. 28, pp. 573-583, 2003. (Article)
- [55] F. Ahwide, A. Spena, and A. El-Kafrawy, Estimation of Electricity Generation in Libya Using Processing Technology of Wind Available Data: The Case study in Derna”, *APCBEE Procedia*, DOI: 10.1016/j.apcbee.2013.05.078, Vol. 5, pp. 451-567, 2013. (Article)
- [56] Satyanarayana G. and Shiva P. K. K., “Wind energy potential and cost estimation of wind energy conversion systems (WECSs) for electricity generation in the eight selected locations of Tigray region (Ethiopia)”, *Renewables: wind, water and solar*, DOI:10.1186/s40807-016-0030-8, Vol. 3 No.10, 2016.
- [57] International Energy Agency. CO2 Emissions from fuel combustion. Highlights, IEA 2010.
- [58] RETScreen International. Clean energy project analysis: RETScreen engineering and cases textbook. 3rd ed.; Minister of Natural Resources: Canada, 2005.
- [59] P. Luckow, E. A. Stanton, S. Fields, W. Ong, B. Biewald, S. Jackson, and J. Fisher, Spring 2016 National Carbon Dioxide Price Forecast. Synapse Energy Economics Inc: Cambridge, MA, USA, March 2016.
- [60] Anderson, John D., Jr., *Fundamentals of Aerodynamics*, 2nd Edition McGraw-Hill, New York, 1991.
- [61] Liepmann, H.W. and Roshko, A., *Elements of Gasdynamics*, Wiley, New York, 1957.
- [62] Anderson, J.D., Jr., *Modern Compressible Flow: With Historical Perspective*, 2nd Edition McGraw-Hill, New York, 1990.

- [63] Kutler, P., 'Computation of Three-Dimensional, Inviscid Supersonic Flows,' in H.J. Wirz (ed.), *Progress in Numerical Fluid Dynamics*, Springer-Verlag, Berlin, 1975, pp. 293–374.
- [64] ANSYS. Inc. Is certified to ISO 9001:2008.
- [65] David C. Wilcox, "*Turbulence Modeling for CFD*", DCW Industries, Inc., 1993.
- [66] C. J. Chen, S. Y. Jaw, "*Fundamentals of Turbulence Modeling*", Taylor and Francis, 1998.
- [67] Spalart P.R., Allmaras S.R., "*A One-Equation Turbulence Model for Aerodynamic Flows*", AIAA 92-0439, AIAA 30th Aerospace Sciences Meeting and Exhibit, Reno, NV, Jan 6-9, 1992.
- [68] Klaus A. Hoffmann, Steve T. Chiang, "*Computational Fluid Dynamics*", Volume III, Engineering Education System, Wichita, Kansas, 4th Edition, 2000.
- [69] Menter, F.R., "*Two-Equation Eddy-Viscosity Turbulence Models for Engineering Applications*", AIAA Journal, Vol. 32, No. 8, pp. 269-289, 1994.
- [70] Wilcox D., "*Reassessment of the scale-determining equation for advanced turbulence models*", AIAA Journal, vol.26, pp.1299-1310, 1988.
- [71] Wilcox D., "*Turbulence model for CFD*", tech. rep., DCW Industries, Inc., 5354 Palm Drive, La Canada, Calif, 1993
- [72] Hakimi N., "*Preconditioning methods for time dependent Navier-Stokes equations*", PhD Thesis, Dept of Fluid Mechanics, Vrije Universiteit Brussel, 1997.
- [73] Numeca CFD Fine/Turbo Theory Manual, April 2010.
- [74] E. F. Toro, "*Riemann Solvers ad Numerical Methods for Fluid Dynamics*", Springer, 2nd Edition, 1999.
- [75] <http://www.cfd-online.com/Wiki>
- [76] Aly S., Marconi F., Ogot M., Pelz R., Siclari M., "*Stochastic Optimization Applied to CFD Shape Design*", AIAA-95-1647-CP, pp. 11-20, 1995.
- [77] Thomas Hansen, "Wind Turbine Simulations Using Navier-Stokes CFD," Royal Institute Technology, Stockholm, Master Thesis 2010.
- [78] Numeca CFD AutoBlade user manual, October 2007.
- [79] Anderson, J.D. *Computational Fluid Dynamics: The Basics with Applications*. McGraw-Hill, New York, NY, USA, 1995.

- [80] ANSYS. Gambit - Computational Fluid Dynamics Preprocessor from Fluent. <http://www.fluent.com/software/gambit/>, 2008.
- [81] M. M. Yelmule and E. A. Vsj, "CFD predictions of NREL Phase VI rotor experiments in NASA/AMES wind tunnel," *International Journal of Renewable Energy Research*, vol. 3, no. 2, pp. 261-269, 2013.
- [82] A.S. Ahmed Shata; R. Hanitsch. The potential of electricity generation on the east coast of Red Sea in Egypt. *Renew. Energy* **2006**, 3, 1597-1615, DOI: 10.1016/j.renene.2005.09.026.
- [83] A.S. Ahmed Shata; R. Hanitsch. Electricity generation and wind potential assessment at Hurghada, Egypt. *Renew. Energy* **2008**, 33, 141-148, DOI: 10.1016/j.renene.2007.06.001.
- [84] M.S. Adaramola; S.S. Paul; S.O. Oyedepo. Assessment of electricity generation and energy cost of wind energy conversion systems in north-central Nigeria: *Energy Convers. Manga* 2011,52,3363DOI: 10.1016/j.enconman.2011.07.007.

CURRICULUM VITAE

PERSONAL INFORMATION

1. Surname, Name: Silini, Salem Ramadan
 2. Nationality: Libyan
 - Date and Place of Birth: 1 January 1966, Tarhana – Libya
 3. Marital Status: Married with 4 children
 4. Phone: +2185218683
- email: salemsilini@ymail.com



5. EDUCATION

6. MS Kazan University Mechanical Engineering, 2002
 7. BS Tripoli University Engineering, 1990
- High School Ibn Khaldun for boys

WORK EXPERIENCE

- | | |
|--------------|------------------------------------------------------|
| 2018 Present | University Teacher |
| 2009 – 2010 | Head of Technical Affairs Department of Examinations |
| 2012 -1013 | Head of the Evaluation and Measurement Office |
| 1991 – 2004 | Engineer at the Technical Research Center |

LANGUAGES

Arabic (Native), English (Good), Russian (Little)

PUBLICATIONS

- 1 - Technical and Economical Evaluation and GHG Analysis of Wind Power Generation in Four Sites Using Different Weibull Parameters: (INTERNATIONAL JOURNAL of RENEWABLE ENERGY RESEARCH. M. A. Elfarra and S. Silini, Vol.8, No.3, September 2018).
- 2 - Submitted under tittle (Prediction of optimum blade tip pitch angle and proper blade sizing of a wind turbine to minimize the generated electricity cost: A study based on CFD and real wind data) to JESTCH JOURNAL 2018.
- 3- Many researches on the manufacture and testing of heat exchangers during the work of the research center.

HOBBIES

football, Tourism and exploration, Computers, reading.